UNIVERSITÀ DEGLI STUDI DI TRIESTE

XXX CICLO DEL DOTTORATO DI RICERCA IN

Scienze della Terra e Meccanica dei Fluidi

Surface Circulation Structures in the Malta Sicily Channel derived from HF radar and altimetry: Estimation, validation and analysis.

Settore scentifico-disiplinare: **GEO/12**

OCEANOGRAFIA E FISICA DELL'ATMOSFERA

DOTTORANDO / A

NYDIA CATALINA REYES SUAREZ

COORDINATORE

PROF. PIERPAOLO OMARI

SUPERVISORE DI TESI

PROF. MIROSLAV GACIC

ANNO ACCADEMICO 2016/2017

Surface Circulation Structures in the Malta Sicily Channel derived from HF radar and altimetry: Estimation, validation and analysis.

Nydia Catalina Reyes Suárez

Universitá degli Studi di Trieste

A thesis submitted for the degree of

Doctor of Philosophy

March 2018

This thesis is dedicated to
Abuelito
for teaching me that the best heritage is KNOWLEDGE.

Acknowledgements

You can start over again! Dont even think about quitting now! It is easy to replay in your mind how things did not work, how much you lost, what you are going through, how angry you are. There is no amount of conversation or magic that is going to wipe the slate clean. You are wasting valuable time and energy that could be used to regain a new normal and start another version of your life. Even though you are hurt and you may be feeling down stop kicking yourself! Face what has happened. Make the decision to start over again. Les Brown

First of all I would like to thank to my supervisor Miroslav Gacic for his constant support and help through all this years. To professor Jeff Paduan and Mike Cook, which without their help and experience I would not have been able to finish this project. To all my friends and colleagues which dedicate time, gelati, aperitifs, serate, cenette, movie nights, dancing nights, arrampicate and gite insieme. To the ones who have had the guts and patience of dealing with me. And of course to my family which even if far far away from me, they have been and I am pretty sure will be there for me always. And last but not least, to Max, which has filled my days with Joey!

Abstract

The Malta Sicily Channel makes part of the Sicily channel system, where water exchanges and thermohaline properties between the Eastern and Western Mediterranean basins take place; at the same time this exchange influences the biological processes and it is relevant from the productive and environmental point of view. A geostrophic current field in the Sicily channel was computed out from AVISO Absolute dynamic topography product, in order to get a broader picture and the main structures influencing the Malta Sicily Channel in a bigger spacial scale. Those data sets include MADT starting from January 1993 to December 2015. On the other hand, scatterometer wind fields spanning from January 1988 to December 2011 from the CCMP (Cross-Calibrated Multi-Platform wind vector analysis) were obtained for the Sicily channel as well, to see the influence of the wind in this area. Validation and then analysis of the surface circulation was made using estimates of the velocity field from High frequency radar data spanning from August 2012 to January 2015 (a three array of CODAR HF-radars between Malta and Sicily, under the CALYPSO project), satellite chlorophyll, sea surface temperature, and numerical and real drifters. CCMP v2 scatterometer datasets spanning from August 2012 to January 2015, alongside with the HFR datasets, were used in order to study high frequency motions as well as mesoscale structures that were not identified previously for this area, by means of different methods such as *Kundu*, 1976 [53] and *Sanderson et al.*, 1995 [99]]. These datasets helped us to identify the main surface circulation structures which are fundamental in order to understand the Malta Sicily Channel circulation dynamics.

Contents

1 Introduction **1**

2 Methods and Datasets **12**

2.1 Theory and concepts: motion and circulation in the ocean 12

2.1.1 Equations of Motion. 14

2.1.2 Wind forcing 20

2.1.2.1 Inertial currents 20

2.1.2.2 Ekman Layers 21

2.1.3 Geostrophic Currents 24

2.1.4 Surface Geostrophic Currents from Altimetry 27

2.2 Datasets and methods 27

2.2.1 High Frequency Radar 27

2.2.2 Mediterranean Sea (M)ADT - Absolute Dynamic Topography 31

2.2.2.1 Empirical Orthogonal Functions - EOFs 34

2.2.3 Cross-Calibrated Multi-Platform wind vector analysis 37

2.2.4 Drifters 37

2.2.5 Chlorophyll 38

2.2.6 Sea Surface Temperature. 39

2.2.7 Complex Correlation and veering estimation. 40

2.2.8 Kinematic properties of an eddy. 41

3 Results and Discussion **45**

3.1 The Sicily channel 45

3.1.1 Mean surface circulation 45

3.1.2 Eddy Kinetic Energy (EKE). 55

3.1.3 Empirical Orthogonal Functions (EOF) 56

3.1.4 Wind Fields 63

3.2 The Malta Sicily channel 66

3.2.1 Correlation coefficients 72

3.2.2 Comparison among available spatial data 74

3.3 Short time scales in the Malta-Sicily channel 78

3.3.1 Complex correlation. 81

3.3.2 The Malta Sicily gyre 82

3.4 Ekman pumping in the Malta Sicily channel 86
3.4.1 Ekman Layer 87

4 Conclusions **92**

Bibliography **96**

List of Figures

1.1 Mediterranean basin geometry and nomenclature for major sub-basins and straits. Shaded areas indicate depths less than 200 m. Boxes (14) are locations of different water mass formations [*Pinardi et al.*, 2015 [87]] 2

1.2 Schematic of the scales of circulation variabilities and interactions in (A) western Mediterranean, (B) eastern Mediterranean [*Robinson et al.*, 2001 [93]]. 3

1.3 Bathymetric map of the Sicilian Channel and surrounding areas. 4

1.4 Thermal infrared images of the Strait of Sicily and adjacent areas. The image was derived from NOAA 9 AVHRR data. Daytime passage at 1340 UT, January 3, 1986. A growing eddy-like disturbance is indicated by an arrow (Manzella et al., 1988 [62]). 5

1.5 Infrared satellite image of the Strait of Sicily on January 27, 1996. Land is white and bordered by a black line; clouds are extra-labeled. The geographical grid is $1° \times 1°$. The white box frames a 50km baroclinic wave (Onken et al., 1998 [78]) . 6

1.6 Scheme of the Atlantic Water circulation in the Sicily Channel (SC) area mainly summarized by Sorgente et al., 2011 [105], with permanent patterns in black lines, summer patterns in red lines, and winter patterns in blue lines. Note that the Maltese Channel Crest (MCC) is drawn as an anti-cyclone (as in Beranger et al., 2004 [7] and Lermusiaux and Robinson 2001 [58]). The bathymetry is drawn using a grey scale to highlight the shallow continental shelves in the Central Mediterranean (m). L is Lampedusa Island (Jouini et al., 2016 [52]) 7

1.7 3-Dimensional model bathymetry of the Malta channel (from Drago et al., 2003. [28] 9

1.8 3-Dimensional image of the Malta escarpment taken from the CUMECS-2 blog. CUMECS-2 was a research expedition that surveyed the Malta-Sicily Escarpment from 31st August to 7th September 2014 [75] 10

2.1 Time and space typical scales of physical oceanographic phenomena from turbulence to changes in ocean circulation associated with Earths orbit variations (*Huang*, 2010 [45]). 13

2.2 Forces and accelerations in a fluid: (a) acceleration, (b) advection, (c) pressure gradient force, (d) gravity, and (e) acceleration associated with viscosity ν (*Talley*, 2011 [107]). 16

2.3 Ekman layer velocities (Northern Hemisphere). Water velocity as a function of depth (upper projection) and Ekman spiral (lower projection). The large open arrow shows the direction of the total Ekman transport, which is perpendicular to the wind (*Talley et. al*, 2011 [107]). 22
2.4 Ekman transport divergence near the equator driven by easterly Trade Winds. (b) The effect of equatorial Ekman transport divergence on the surface height, thermocline, and surface temperature. (c) Coastal upwelling system due to an alongshore wind with offshore Ekman transport (Northern Hemisphere) *Talley et. al*, 2011 [107]. 23
2.5 Geostrophic balance: horizontal forces and velocity. (a) Horizontal forces and velocity in geostrophic balance. PGF=pressure gradient force. CF=Coriolis force. (b) Side view showing elevated pressure (sea surface) in center, low pressure on sides, balance of PGF and CF, and direction of velocity v (into and out of page) *Talley et. al*, 2011 [107]. 24
2.6 Representative HF radar Doppler spectrum *Harlan et al.*, 2010 [42]). 28
2.7 Schematic for determining the resulting vector current from velocity components of two intersecting radials (*Graber et al.*, 1997.[38]). 29
2.8 High frequency radar stations of three CODAR SeaSondes at Ta'Sopu (Malta), Ta'Barkat (Malta) and Pozzallo Harbor (Sicily, Italy) from [16] (*Cosoli et al.*, 2015 [23]). 31
2.9 Different notions of sea surface height used in altimetry (Copernicus CMEMS-SL-QUID-008-032-051 catalog [22]). 33
2.10 System Argos uses radio signals transmitted from surface buoys to determine the position of the buoy. A satellite receives the signal from the buoy B. The time rate of change of the signal, the Doppler shift F, is a function of buoy position and distance from the satellite's track. Note that a buoy at BB would produce the same Doppler shift as the buoy at B. The recorded Doppler signal is transmitted to ground stations E, which relays the information to processing centers A via control stations K. From *Stewart*, 2008 [106]. 38

3.1 Filtered absolute dynamic topography (MADT) time series spatially averaged over the Sicilian channel (10-16 °E and 33-38 °N). The blue line represents the 4th polynomial fit which shows the pseudo-oscillatory behavior of the time series. The latest being associated with the BiOS mechanism. 46
3.2 Schematic representation of the AdriaticIonian bimodal oscillating system: (a) anticyclonic mode and (b) cyclonic mode [taken from *Gacic et al.*, 2010 [33]]. . . . 47
3.3 Interannual map of Mediterranean absolute dynamic topography and mean geostrophic circulation in the Sicilian channel. Permanent structures in black, summer in red, winter in blue and semipermanent structures in dashed lines. The most predominant gyres are highlighted in green. 49

3.4 Interannual Winter map of Mediterranean absolute dynamic topography and mean geostrophic circulation in the Sicilian channel. 50
3.5 Interannual Spring map of Mediterranean absolute dynamic topography and mean geostrophic circulation in the Sicilian channel. 51
3.6 Interannual Summer map of Mediterranean absolute dynamic topography and mean geostrophic circulation in the Sicilian channel. 53
3.7 Interannual Autumn map of Mediterranean absolute dynamic topography and mean geostrophic circulation in the Sicilian channel. 54
3.8 Sicily channel mean geostrophic eddy kinetic energy (EKE) derived from MADT Aviso datasets over the time span 1993-2015. Colorbar represents eddy kinetic energy in cm^2/s^2 56
3.9 First EOF/PC mode of SSH in the Sicilian channel, dataset spanning from January 1993 to December 2015. 57
3.10 Sea surface heights from 2010 to 2013. 59
3.11 Geostrophic Currents from 2010 to 2013. 60
3.12 Second EOF/PC mode of SSH in the Sicilian channel, dataset spanning from January 1993 to December 2015. 62
3.13 Wind stress fields averaged seasonally for the whole CMPP time series available (1988-2011). 64
3.14 Wind stress curls fields averaged seasonally for the whole CMPP time series available (1988-2011). Orange (positive wind stress curl) represents upwelling or Ekman pumping events. Violet (negative wind stress curl) show places of Ekman suction or downwelling. Green arrows represent wind stress as in Fig. 3.13 65
3.15 Power spectra of HF-radar components showing diurnal K1, O1, P1 (1 cpd, yellow shaded area) and semi-diurnal M2, S2, N2 (2 cpd, purple shaded area) tidal components in the Malta Sicily Channel. 67
3.16 1 month recording trajectories from Drifters deployed on July 2013 by the National Institute of Oceanography and Experimental Geophysics OGS (image has been provided by Dr. Simone Cosoli by official mail). 69
3.17 Interpolated best grid coverage from HFR datasets. Here each grid point satisfies a minimum data return of 95%. 69
3.18 Show numerical (black) and real (red) drifters. The numbers represent the OGS identification number and the letter in front of them represent the month in which the drifter was deployed. Green dots represents the places in which the numerical drifters were deployed. 71
3.19 Separation distance between the numerical drifters computed from HFR and the real ones deployed by OGS in October and September 2013 and March 2014. Colorbar represents the number of numerical drifters with a separation distance $x(t)$ at certain time t over the grid in Figure. 3.17. 72
3.20 U Spatial correlation between a central point of the grid with the ones surrounding. 73

3.21 V Spatial correlation between a central point of the grid with the ones surrounding. 74
3.22 U-V Spatial correlation between a central point of the grid with the ones surrounding. 74
3.23 Geostrophic currents calculated form altimetry datasets, showing the mesoscale anticyclonic gyre identified on February 2014 (down) and the pathway of Atlantic Ionian Stream on September 2012 (down). Black lines represent the current field form HF radar data. Color arrows represent the geostrophic current field and colorbar gives the magnitude of each velocity vector. 76
3.24 Sea surface temperature from Aqua/MODIS satellite mission showing the mesoscale anticyclonic gyre on January 2013 (upper left) and the Atlantic Ionian Stream pathway on May, August and October 2013. Black lines represent current field form HF radar data and the Temperature in °C. 77
3.25 Chlorophyll concentration from NOAA N' satellite mission showing the influence of the mesoscale anticyclonic gyre and the Atlantic Ionian Stream on the Malta-Sicily channel on August 2012, January, March and October 2013. Black lines represent current field form HF radar data, magenta lines the geostrophic velocity field, red ones the wind velocity field and the colorbar represents chlorophyll concentration in mg $pigment/\mathrm{m}^3$. 78
3.26 Interpolated grid for each of the datasets. Violet arrows represent wind vectors, red arrows represent geostrophic currents derived from MADT data and yellow arrows are the velocity vectors from HFR on 01 August 2012. 79
3.28 V component time series of Wind, geostrophic and HFR velocities. Upper panel compares the residual latitudinal (North-South) v velocity ($V_{residual} = V_{radar} - V_{geostrophic}$) with the latitudinal v velocity wind component. Lower panel shows the time series of each dataset; wind (red), geostrophic (blue) and HF radar (green). 79
3.27 U component time series of Wind, geostrophic and HFR velocities. Upper panel compares the residual meridional (East-West) u velocity ($U_{residual} = U_{radar} - U_{geostrophic}$) with the meridional u velocity wind component. Lower panel shows the time series of each dataset; wind (red), geostrophic (blue) and HF radar (green). 80
3.29 grid cells where complex correlation is computed. Number are used to reference each parameter to the grid point which they belong to. So, p_1, θ_1 are the parameters corresponding to box 1. 81
3.30 subgrid of the HFR original grid to calculate vorticity with *Sanderson*, 1995 [99] method. Red dots denote grid points where data was available for most of the time period studies. Blue, green and black dots represent grid points where velocity will be compared with vorticity. 83

3.31 Upper panel represents the meridional velocity time series on Figure. 3.30. Blue time series corresponds to the blue dot in Figure. 3.30, as well as the green dot corresponds to the green time series. Intermediate black dots time series in Figure. 3.30 are represented in gray in the current figure. Lower panel depicts the East - West difference (left hand side) time series calculated from the difference between blue and green velocity time series from the HFR radar dataset and vorticity (right hand side) calculated using *Sanderson*, 1995[99] method through the lstranslate routine developed by the HFR radar group at the Naval Postgraduate School. . . 84
3.32 Upper panel represents the latitudinal velocity time series on Figure. 3.30. Blue time series corresponds to the blue dot in Figure. 3.30, as well as the green dot corresponds to the green time series. Intermediate black dots time series in Figure. 3.30 are represented in gray in the current figure. Lower panel depicts the South-North difference (left hand side) time series calculated from the difference between blue and green velocity time series from the HFR radar dataset and vorticity (right hand side) calculated using *Sanderson*, 1995[99] method through the lstranslate routine developed by the HFR radar group at the Naval Postgraduate School. . . 85
3.33 Anticyclonic gyres in agreement with vorticity calculated from Sanderson's method. 86
3.34 The surface Ekman layer generated by a wind stress on the ocean. 88
3.35 Theoretical Ekman layer compared with ADCP data at different stations in the Malta-Sicily channel. 90
3.36 Surface velocity fields obtained from HFR (High frequency Radar) measurements on The 2nd and the 3rd October 2013. The black boxes show the average position of the stations. 91

1 Introduction

The ocean is in constant motion. This turbulent fluid evolves in time and space over a large variety of scales (from global such as the thermohaline circulation to small scales like molecular mixing or capillary waves), where complex oceanic structures like gyres, eddies, jets, filaments, and the like, originate from the interaction of all these scales of motion. Mesoscale to sub-mesoscale oceanic structures (tens of kilometers to hundred of meters) contribute to the vertical and horizontal transport of passive substances such as nutrients and sediments, likewise influences ocean stratification; but it is at the surface where most of human activity in the ocean takes place. For example, ocean currents affect fishing, where seasonal and interannual variability of currents have a significant impact on fish larval dispersion [*Qian et al.*, 2015 [91]]. On the other hand, boating, navigation and so commercial shipping impart a significant contribution on fuel consumption and transport [*Bialystocki and Konovessis*, 2016 [13]; *Dohan*, 2017 [25]]; where knowledge of surface currents and so tracking methods and instruments (such as High Frequency Radars), can be of help in cases like oil-spills, search and rescue support [*Paduan and Rosenfeld*, 1996 [81]; *Paduan and Washburn*, 2013 [82]], tracking marine debris, mapping or backtrack the spread of pollutants to the original source (e.g. the pieces of the Malasyan Airlaines flight 370 airplane [*Trinanes et al.*, 2016 [110]]). In this thesis we apply various techniques in order to identify the main surface circulation structures along with the dynamics and the main forcing function in the Malta-Sicily Channel area, a region of primary importance and a natural laboratory in the Mediterranean sea.

The Mediterranean sea (Figure. 1.1) is a mid-latitude anti-estuarine semi-enclosed sea, subdivided into two sub-basins; the eastern (EMED) and the western (WMED) Mediterranean basins. This almost isolated system exchanges water, salt, heat and other properties with the North Atlantic Ocean (NAO) via the narrow Gibraltar strait ($\sim$60 km long, $\sim$12 km wide at its narrowest section at Pt. Cires and $\sim$300 m deep at the main sill between Pt. Paloma, Spain and Pt. Altares, Morocco [*Candela*, 1991 [17]]) on its westernmost side which plays an important role in the global thermohaline circulation [*Robinson et al.*, 2001 [93]; *Pinardi et al.*, 2015 [87]]. Due to the limited exchange with open Ocean, the Mediterranean Sea can bee seen as thermodynamic system where evaporation exceed precipitation and the negative and the fresh water

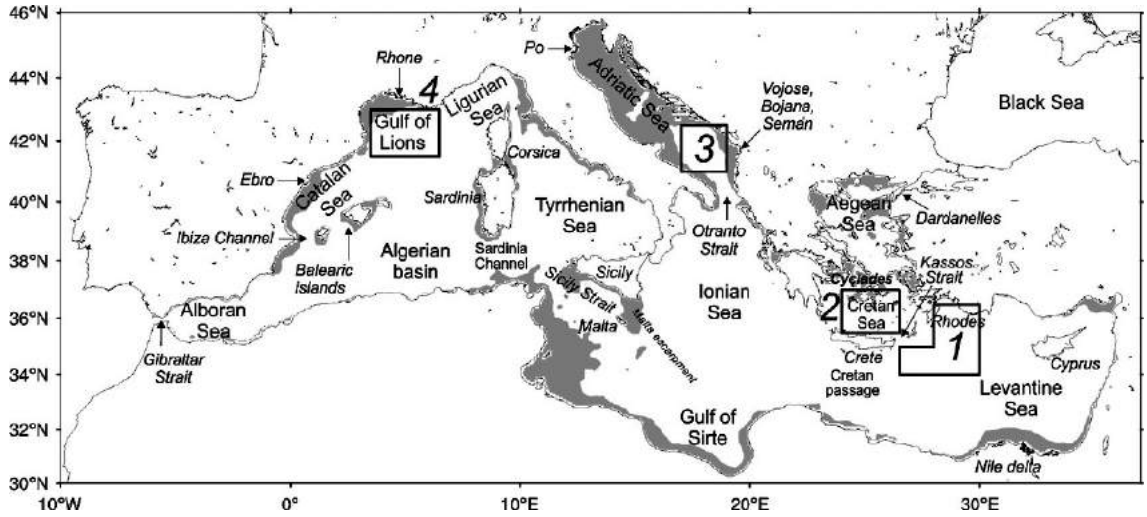

Figure 1.1: Mediterranean basin geometry and nomenclature for major sub-basins and straits. Shaded areas indicate depths less than 200 m. Boxes (14) are locations of different water mass formations [*Pinardi et al.*, 2015 [87]]

budgets are balanced by the input of heat and water from the Gibraltar strait [*Pinardi et al.*, 2015 [87]] subsequently changing the properties of the water masses [*Bethoux and Gentili*, 1999 [10]; *Millot and Taupier-Letage*, 2005 [64]]. The system behave as a double layer system in which the inflow of colder and fresher water from the Atlantic Ocean at the surface (Atlantic water, AW) transforms progressively into warmer and more saline thus denser water in the bottom layer as water exchange over straits flows throughout the Western and Eastern Mediterranean basins. Part of this flow then recirculates and outflows (Levantine intermediate water, LIW) into the Atlantic Ocean as an intermediate water at the bottom and intermediate layers [*Sorgente et al.*, 2011 [105]; *Jouini et al.*, 2016 [52]]. The surface temperature for instance, generally increases from the Gibraltar strait to the inner parts of the Mediterranean basin; on the opposite during winter, lowest surface temperatures are found in the extreme northern parts and in the inner parts of the Adriatic and Aegean seas which are sites of dense water formation [*Reddy*, 2001 [92]]. On the other hand, the Mediterranean circulation also takes place at different temporal and spatial scales at the same time, namely basin scale (the slow thermohaline cell), sub-basin (gyres and jets) scale and mesoscale (internal eddies and swirl flows) as shown in Figure. 1.2, where it is also subjected to the combined effects of wind stress and buoyancy fluxes at the surface due to fresh water input, heat exchanges and internal dynamical processes.

In the Sicilian channel, complexities are introduced by topography and by the shape of the coastline [*The POEM group*, 1992 [41]; *Robinson et al.*, 2001 [93]; *Pinardi et al.*, 2015 [87]]. This topographically complex passage connects two sub-basins in the Mediterranean, the EMED and the WMED. At the northern-most part of the channel, between Cape Bon-Tunisia and Mazzara del Vallo-Italy, the Sicily strait

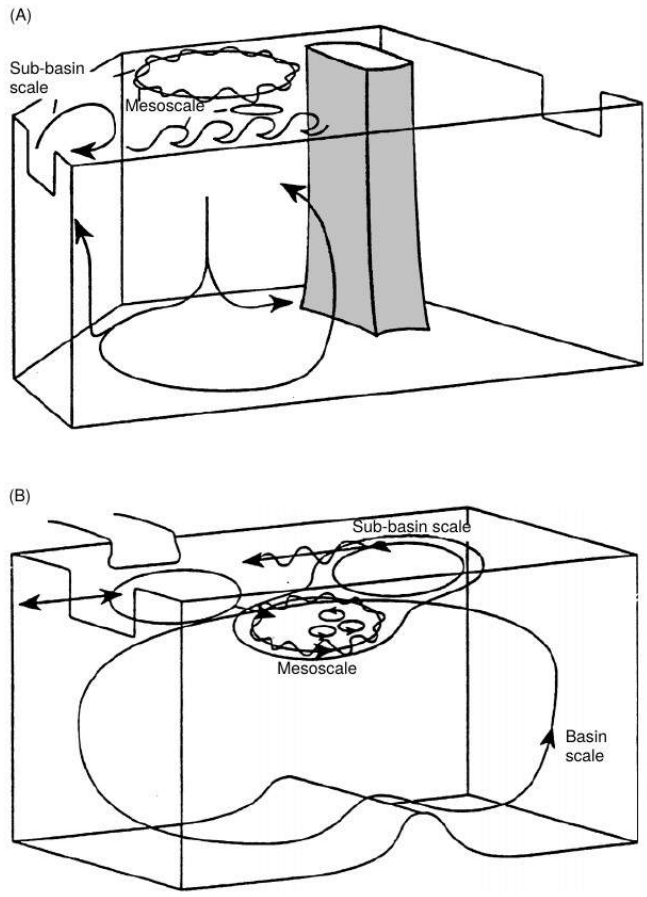

Figure 1.2: Schematic of the scales of circulation variabilities and interactions in (A) western Mediterranean, (B) eastern Mediterranean [*Robinson et al.*, 2001 [93]].

(140 km; *Ismail et al.*, 2014 [47]) divides the channel in a two-sill, two-layer system. As at Gibraltar, it is maintained by the excess of evaporation in the EMED (Figure. 1.3) [*Astraldi et al.*, 1999 [2]; *Pinardi et al.*, 2015 [87]]. A ridge divides the strait longitudinally into two channels, each with different cross sectional areas. The channel on the Italian side is very narrow and has a maximum depth of 430 m whereas the one the Tunisian side is wider, shallower and with a sill depth of about 360 m [*Astraldi et al.*, 1999 [2]]. Additionally, the canyons in the Sicily Channel are very shallow and exert a strong constraint on the deep water exchange with the EMED, where trenches can be deeper than 1700 m [*Astraldi et al.*, 2002 [3]].

Due to strained diplomatic relations between Italy and Tunisia, researchers have to face difficulties to study the whole channel, constraining Italian and Tunisian scientist to study only the part of the channel that belongs to their respective countries [*Schroeder et al.*, 2008 [100]; *Ismail et al.*, 2012, 2014 [46] [47]].To clarify, in this thesis, the Sicily channel comprises the area between $\sim$ 32°N to $\sim$ 37°N and $\sim$ 10°E to

$\sim$ 16°E. Whereas the Sicilian strait refers to the northern-most part of the channel, between Cape Bon-Tunisia and Mazzara del Vallo-Italy (as in Figure. 1.3).

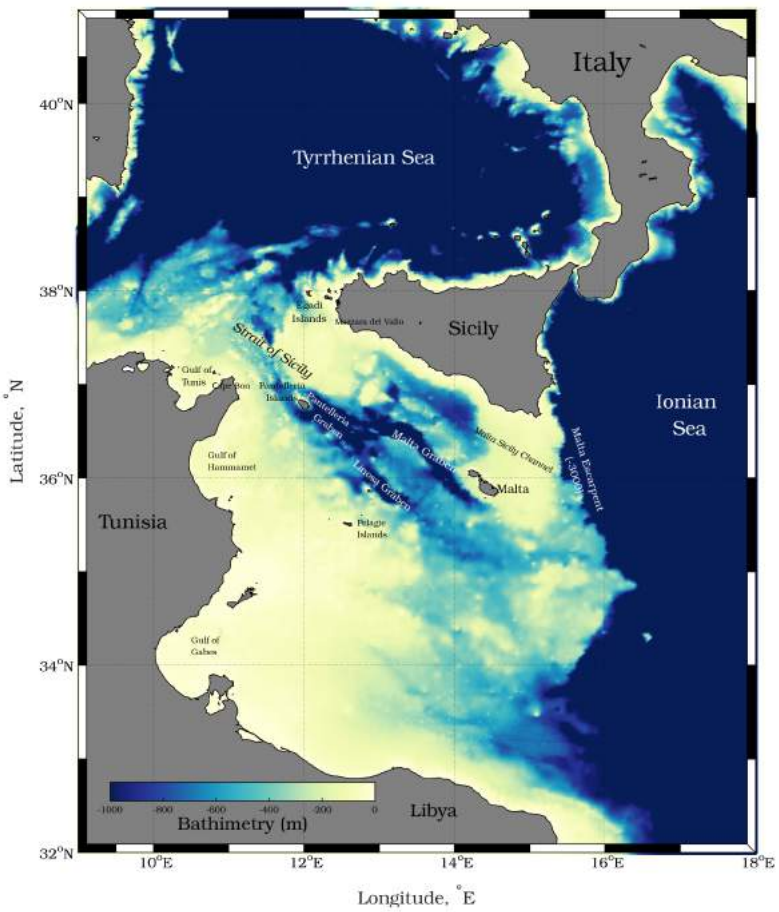

Figure 1.3: Bathymetric map of the Sicilian Channel and surrounding areas.

The surface circulation in the Sicily Channel has been synthesized from different datasets, oceanographic campaigns as well as by different modeling studies. Starting back in the 60s with the work of *Frasseto*, 1965 [31], succeeded later by other projects e.g. *Fieux*, 1971 [30]; *Grancini et al.*, 1972 [39]; *Ozturgut*, 1975 [79]; *Morelli et al.*, 1975 [65]; *Garzoli and Maillard*, 1976 [36]; *Johannessen et al.*, 1977 [51]; *Hopkins*, 1978 [97]; *Bethoux*, 1979 [9]; *Philippe and Harang*, 1982 [83]; *Gelsi and Mossetti*, 1984 [37]; *Lacombe et al.*, 1985 [54]; *Hopkins*, 1985 [44]; *Grancini and Michelato*, 1987 [40]; *Manzella et al.*, 1988 [63]; *Piccioni et al.*, 1988 [84]. Then with the incorporation of computational models, in the early 90s works like *Manzella et al.*, 1990 [62]; *Moretti et al.*, 1993 [66]; *Robinson et al.*, 1992 [94]; *Astraldi et al.*, 1996 [4]; *Onken and*

Sellschopp, 1998 [78]; Herbaut et al., 1998 [43]; *Bethoux and Gentili*, 1999 [10], and the important collaboration works of Lermusiaux and Robinson at the beginning of the 00s *Lermusiaux and Robinson*, 1999 [57]; *Lermusiaux and Robinson*, 1999 [57]; *Lermusiaux and Robinson*, 2001 [58], among others gave a broader picture of the zone and where the physical conditions of the channel were investigated *Béranger et al.*, 2005 [6].

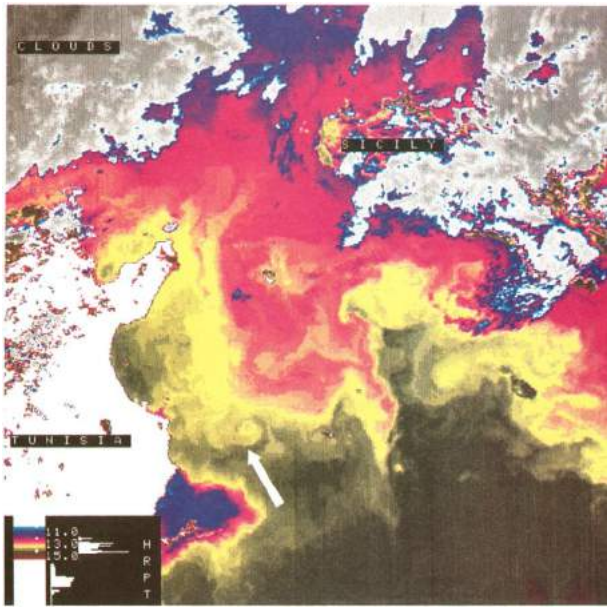

Figure 1.4: Thermal infrared images of the Strait of Sicily and adjacent areas. The image was derived from NOAA 9 AVHRR data. Daytime passage at 1340 UT, January 3, 1986. A growing eddy-like disturbance is indicated by an arrow (Manzella et al., 1988 [62]).

One of the first observations obtained from satellite, which stimulated scientist to study the Sicily channel, is shown in Figure. 1.4. This thermal infrared image of the strait of Sicily was studied by *Manzella et al.*, 1988 [63]. They found that during winter, part of the Atlantic water that enters into the Tunisian side of the strait meanders around the African coast constrained by a thermal front. This in turn weakens as the surface temperatures become isothermal. Meanders, rings and a large tongue of warm water penetrating the central area was also observed by *Grancini and Michelato*, 1987 [40] from satellite and hydrological data. On the other hand, *Onken and Sellschopp*, 1998 [78] described the evolution of baroclinic waves in the strait (Figure. 1.5). In the numerical model the flow was found to be baroclinically unstable, where in winter time the instabilities are driven by a seasonal internal potential vorticity whereas for the summer period it depends on the bottom slope. In their model they also found that for the winter period, the range of unstable waves is larger and that the potential energy release is stronger making the horizontal mixing

more efficient, as well as higher values of kinetic and eddy kinetic energies than in summer as previous works suggested.

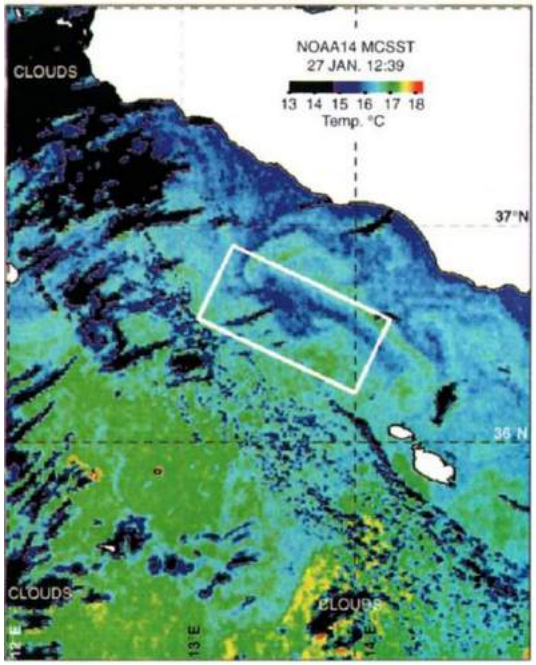

Figure 1.5: Infrared satellite image of the Strait of Sicily on January 27, 1996. Land is white and bordered by a black line; clouds are extra-labeled. The geographical grid is $1° \times 1°$. The white box frames a 50km baroclinic wave (Onken et al., 1998 [78])

The circulation of this area has been synthesized by *Jouini et al.*, 2016 [52] as follows (Figure. 1.6). The Algerian Current (AC) advects the AW eastward along the Algerian slope and splits into two branches at the entrance to the SC, owing to a topographic effect caused by the Sicily sill [Herbaut et al., 1998 [43]]. A first branch of the AW stream penetrates into the Tyrrhenian Sea forming the Bifurcation Tyrrhenian Current (BTC, as denoted by Sorgente et al., 2011 [105]), which flows along the northern coast of Sicily, while the second branch crosses the Sicily Channel and then enters the Eastern Mediterranean flowing along the coast of Tunisia [*Manzella et al.*, 1990 [62]] enhancing the Atlantic Tunisian Current (ATC, *Beranger et al.*, 2004 [7]). In several high-resolution models, the BTC generally flows eastward along the northern coast of Sicily [*Onken et al.*, 2003 [77]; *Pierini and Rubino*, 2001 [86]; *Napolitano et al.*, 2003 [67]; *Beranger et al.*, 2004 [7]], while in some others [*Pierini and Rubino*, 2001 [86]; *Sorgente et al.*, 2003 [104]; *Beranger et al.*, 2004 [7]], the BTC presents a secondary bifurcation near 11°E flowing north-westward, which forms a cyclonic circulation denoted as the South Eastern Sardinian Gyre (SESG) by *Sorgente et al.*, 2011 [105]. An additional AW stream is also observed, entering the Eastern Mediterranean and flowing along the southern coast of Sicily forming the so called Atlantic Ionian Stream (AIS, as denoted by *Robinson et al.* 1999 [95]).

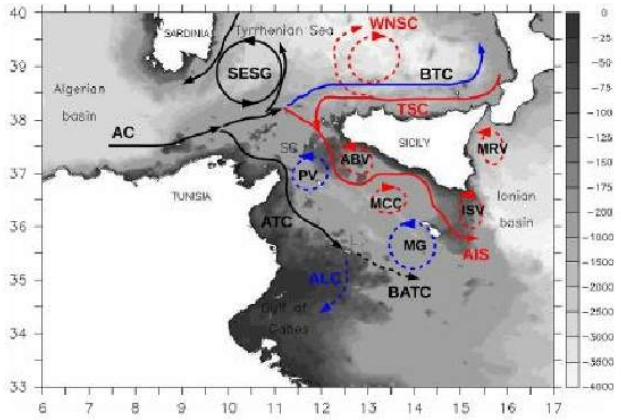

Acronym	Name	Notes
ABV	Adventure Bank Vortex	Cyclonic
AC	Algerian Current	
AIS	Atlantic Ionian Stream	
ALC	Atlantic Libyan Current	
ATC	Atlantic Tunisian Current	
AW	Atlantic Water	
BATC	Bifurcation Atlantic Tunisian Current	
BTC	Bifurcation Tyrrhenian Current	
ISV	Ionian Shelf break Vortex	Cyclonic
LIW	Levantine Intermediate Water	
MCC	Maltese Channel Crest	Anti-cylonic
MG	Medina Gyre	Cyclonic
MRV	Messina Rise Vortex	Cyclonic
SESG	South Eastern Sardinia Gyre	Cyclonic
TSC	Tyrrhenian Sicilian Current	
WNSC	Westward Northern Sicilian Current	
PV	Pantelleria Vortex	Cyclonic

Figure 1.6: Scheme of the Atlantic Water circulation in the Sicily Channel (SC) area mainly summarized by Sorgente et al., 2011 [105], with permanent patterns in black lines, summer patterns in red lines, and winter patterns in blue lines. Note that the Maltese Channel Crest (MCC) is drawn as an anti-cyclone (as in Beranger et al., 2004 [7] and Lermusiaux and Robinson 2001 [58]). The bathymetry is drawn using a grey scale to highlight the shallow continental shelves in the Central Mediterranean (m). L is Lampedusa Island (Jouini et al., 2016 [52])

During summer, the AIS is strong and constrained towards Sicily, mainly due to westerly winds, which maintain an upwelling front south of Sicily [*Robinson et al.* 1999 [95]; *Lermusiaux and Robinson*, 2001 [58]; *Beranger et al.*, 2004 [7]]. In the Strait, the stream flows North of Pantelleria and bears north-westward around the Adventure Bank Vortex (ABV). It then turns southeastward in the Maltese Channel Crest (MCC), goes around the Ionian Shelf-break Vortex (ISV) and finally flows off the shelf and bifurcates into the upper western Ionian Sea (Fig. 1.6). The presence of important mesoscale structures like eddies, gyres or plumes [*Sammari et al.*, 1999 [98]; *Lermusiaux*, 1999 [57]; *Ciappa*, 2009 [20]] structures appear, e.g. the cyclonic ABV, ISV and MRV, and anticyclonic MCC, where they most likely agree with the stretching and squeezing of the AIS while is passing through the Sicilian channel as the conservation of potential vorticity over topography suggests [*Lermusiaux and Robinson*, 2001 [58], *Drago et al.*, 2003 [28]]. This definition is rather simple, and we believe that a new definition should be taken into consideration since it has been observed that the AIS circulation is more complex in our studies.

As mentioned before, since the Strait of Sicily is the gateway for the exchange of water between the eastern and the western Mediterranean seas, it is forced by the negative water budget in the eastern Mediterranean, where the loss of water owing to evaporation exceeds the gain due to rainfall and river runoff (E-P, positive) [*Lacombe et al.*, 1985 [54]; *Bethoux and Tailliez*, 1994 [12]]. In winter the decrease of buoyancy is further enhanced by strong surface cooling leading to deep convection and the export of high-salinity Levantine Intermediate Water (LIW) into the Western Mediterranean (WMED) through the Strait in deeper layers [*Bethoux and Gentili*, 1999 [10], [11]; *Millot and Taupier-Letage*, 2005 [64]]. This net loss in the eastern Mediterranean

then is compensated by the inflow of fresher Atlantic Water (AW) in the near-surface layers [*Onken et al.*, 1998 [78]; *Pinardi et al.*, 2015 [87]].

The main objective of this research is to describe the Malta-Sicily channel surface circulation due to its importance for the Mediterranean sea. With the development of ports and free-ports in Malta, around 20% of all oil transported by sea passes by this area, this heavy marine traffic accounts for an annual flux of 350 million tons of crude oil and refined products, which makes the Malta-Sicily channel a highly risky zone in terms of marine pollution from oil among other hazardous substances [*Drago et al.*, 2003 [28]]. On the other hand, from the fisheries point of view, the limited extend of this area makes the ecosystem vulnerable due to bad fishing practices and unsustainable fishing efforts [*Drago et al.*, 2003 [26]]. For this reason, an appropriate knowledge of the physical and biological oceanography (such as the patterns and dynamical process driving the circulation in the area and the biological transport like fish larval dispersion) for the area is necessary in terms of risk prevention and prediction. This area has been relatively studied, with about 104 CTD stations, 1014 XBT and 1407 MBT within the MEDATLAS-I (1997) where sea current measurements are commonly lacking. Satellite Imagery (thermal infrared images *Philippe and Harange.*, 1982 [83]; *Le Vourch et al.*, 1992 [56]) has helped in the identification of synoptic variability and mesoscale phenomena, in particular the upwelling system along the southern coast of Sicily [*Manzella et al.*, 1988 [63]; *Le Vourch et al.*, 1992 [56]].

Lately, with the efforts of A. Drago from the university of Malta and the Calypso project [16], an array of high frequency radars (13.MHz) direction-finding system (CODAR Ocean Sensor) was installed at Ta'Sopo (Gozo), Ta'Barkat (Malta) and Pozzallo Harbor (Sicily) as part of the efforts to better understand the surface circulation in the area. High frequency (HF) radars constitute a well established technique capable of resolving accurately oceanic structures in space and time [*Paduan and Graber*, 1997 [80]]. This is specially true, in combination with Lagrangian drifters, floats, Eulerian current measurements, temperature-salinity profiles, satellite imagery and the appropriate analysis tools. Furthermore, a new product has been released [74] by professor's Drago group in late 2016, the smart-phone app KAPTAN uses data mainly derived from the Calypso HF radar observing system, satellite observations, marine numerical models and weather forecast reports in order to provide hourly suitable local reporting of different parameters such as 2D maps of sea surface currents, air temperatures, precipitation, atmospheric pressure, winds, sea surface temperature, current drift and waves.

The Malta Sicily-channel, is a passage in the mid Mediterranean that separates the Malta island from the southern tip of Sicily. Topographically, this shelf is characterized by a plateau in the middle part with an average depth of 150 m (Figure. 1.3). The

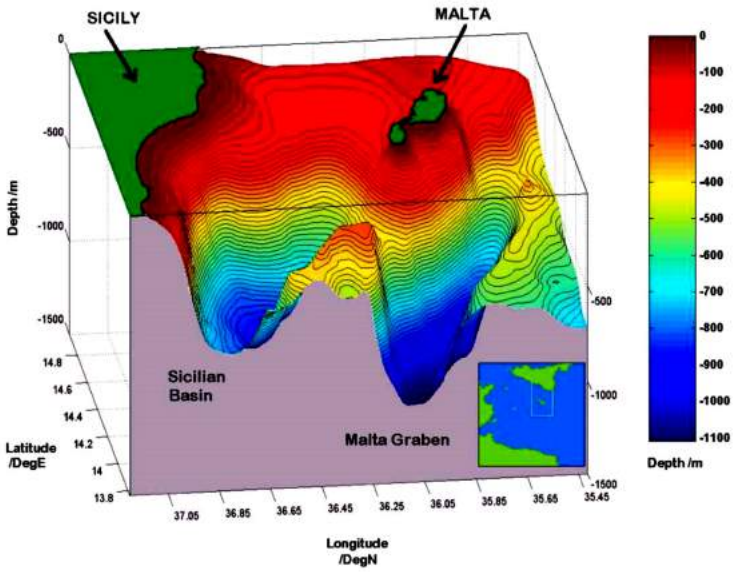

Figure 1.7: 3-Dimensional model bathymetry of the Malta channel (from Drago et al., 2003. [28]

shelf is limited by a submarine ridge where the Maltese islands represent the emerged part [*Lodolo and Ben-Avraham.*, 2015 [59]]. Figure. 1.7 shows a 3-dimensional view of the bathymetry in the channel [*Drago et al.*, 2003 [28]]. The shelf is interrupted from its extension towards the west by the Sicilian basin, which separates it from the Adventure Bank. On its eastern side, it deepens abruptly into the Ionian sea due to the presence of the sharp and deep Malta Escarpment ($\sim$ 2500 m 1.8) one of the largest and least-explored underwater cliffs in the Mediterranean Sea [75]. On the other hand, the Malta graben in Figure. 1.7 makes part of the several bottom depressions reaching depths of $\sim$1700 m in the Sicilian channel (see also Figure. 1.3). We recall that the general circulation in the Sicily channel is mainly driven by the slow Mediterranean thermohaline circulation, together with their mesoscale and seasonal variability, which gives rise to typical structures such the ones presented in Figure. 1.6. Circulation at large time scales (low frequency) in the Malta-Sicily channel is mainly driven by the variability of the AIS; while local winds, tides, Coriolis effect, introduce shorter time scales (higher frequency motions).

The AIS path starts as a meander to the south of the Adventure bank, extending south eastwards and looping back to the north around Malta (MCC in Figure. 1.6). It presents a seasonal pattern in which, during summer and autumn, the flow takes the consistency of a jet stream, gaining positive vorticity as it reaches the shelf break at the east of Malta [*Drago et al.*, 2010 [27]]. This jet stream tends to deflect northward towards the Ionian as a looping meander forming the Ionian shelf break vortex (ISBV in Figure. 1.6). The circulation at intermediate layers consists mainly of Levantine intermediate water (LIW), which resides at a depth of about 200 to 300 m. This

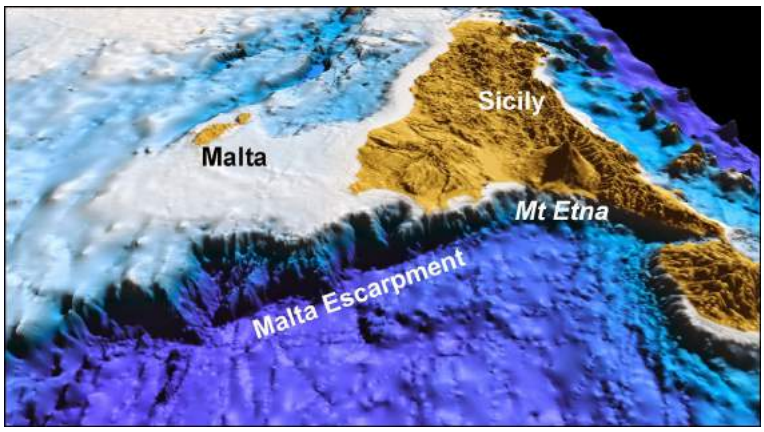

Figure 1.8: 3-Dimensional image of the Malta escarpment taken from the CUMECS-2 blog. CUMECS-2 was a research expedition that surveyed the Malta-Sicily Escarpment from 31st August to 7th September 2014 [75]

water mass enters the MSC via the Medina sill where the sea bottom rises from a depth of $\sim$ 2500 m to a mean around 400 m and flows westward deepening after passing the Sicily strait [*Drago et al.*, 2010 [27]]. The LIW is formed in the Levantine basin during winter as a result of cooling and evaporation processes and is strongly controlled by the complex topography of the MSC [*Pinardi et al.*, 2015 [87]].

In this thesis our main focus is on determining and describing the patterns and dynamical processes driving the surface circulation of the Malta-Sicily Channel. We apply various techniques and data products, such as daily AVISO Salto/Duacs multimission altimeter maps of absolute dynamical topography (MADT), Cross calibrated multi-platform wind vectors (CCMP), high frequency radar (HFR) datasets from the CALYPSO project, satellite Sea Surface Temperature (SST) and Sea Surface Chlorophyll (CHL) as well as Drifter and ADCP data. *Chapter 1* is the introduction, where we give the state of the art of the knowledge of the area under discussion, the motivation and the objectives of this thesis. *Chapter 2*, gives a general overview of the theory necessary to understand the processes influencing the ocean circulation, as well as some basic aspects of the oceanic systems, followed by the description of the datasets previously mentioned and the methodology used. The methods of analysis include: the study of spatial and temporal structures with Empirical Orthogonal Functions (EOF) applied to sea surface heights over geoid data (MADT), geostrophic transport calculations over key transects in the SC region and wind field analysis involving the wind stress and wind stress curl at annual, seasonal and monthly time scales to evidence the wind influence on the current patterns in the SC and MSC surface circulation. In *Chapter 3*, we show the results obtained during the development of this thesis with the methodology aforementioned. Here we analyze surface geostrophic current and Sea Surface Height fields, High Frequency Radar and wind fields in both the Sicily Channel and the Malta-Sicily Channel at annually, seasonally

and monthly times scales in order to extract the main circulation patterns and forcing functions for both areas focusing especially in the MSC. Then, satellite Sea Surface Temperature and Chlorophyll (SST and CHL respectively) observations alongside with drifter trajectories are used to show how these surface circulation patterns can influence particular properties, as well as a way of validation of the high frequency radar estimates. Subsequently, ADCP data in the MSC are be used with the aim of getting insight into the vertical current structure in this area. *Chapter 4* is dedicated to the conclusions and some future work to be done.

2 Methods and Datasets

In this chapter we describe the datasets and methods used to develop this thesis. *First section* describes the theory necessary to understand the processes undergoing ocean circulation. We define our governing equations and some approximations such as Inertial currents, Ekman theory and geostrophic approximation are introduced. In *section 2*, the datasets and methods applied on this thesis are introduced. High Frequency Radar, Maps of Absolute Dynamic Topography, wind vectors from cross-calibrated multi-platform wind vector analysis and drifters, as well as sea surface temperature and chlorophyll are described. Complex correlation, Empirical Orthogonal Functions and Sanderson's method to determine the kinematic properties of an eddy are also depicted.

2.1 Theory and concepts: motion and circulation in the ocean

The ocean is a fluid in constant motion with a very wide range of spatial and temporal scales. Its complexity varies from small motions such as turbulences to ocean currents, waves or the global thermohaline circulation. Figure. 2.1. for instance, shows the space and time scales of some of the most important physical processes in the ocean.

At the smallest scale is molecular mixing. At macroscopic scales of centimeters, vertical layering or microstructure and capillary waves occur. At the scale of meters surface waves are found, which have rapid timescales and fine structure. At scales of tens of meters, internal waves with timescales of about a day can be found. Tides have the same timescales as internal waves, but larger spatial scales that cover hundreds to thousands of kilometers. Mesoscale eddies and strong ocean currents are found at spatial scales of tens of kilometers to several hundred kilometers with timescales of weeks to years. The large-scale ocean circulation has a spatial scale the size of ocean basins up to the global ocean and a timescale ranging from seasonal to permanent. The timescales for wind-driven and thermohaline circulation in Figure. 2.1 can occur around ten years for a gyre to hundred of years through the entire ocean. It can be seen from Figure. 2.1, that short spatial scales in general have short timescales, while the long spatial scales have long timescales. Some exceptions can be found in

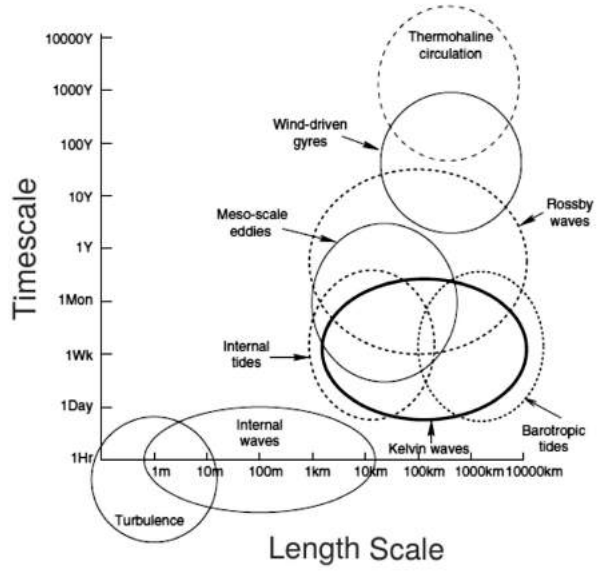

Figure 2.1: Time and space typical scales of physical oceanographic phenomena from turbulence to changes in ocean circulation associated with Earths orbit variations (*Huang*, 2010 [45]).

tides and tsunamis, as well as in some fine-structure phenomena which have longer timescales than might be expected from their short spatial scales (*Talley*, 2011 [107]).

Whether the timescale of an ocean phenomena is greater than or less than about a day, which is the timescale for the Earths rotation, is of special importance since the earth has an important effect on how the water in the ocean moves in response to an applied force. If the force and motion are sustained for days or longer, then the motion is strongly influenced by the rotation. For this, the Rossby number is the parameter telling us the ratio between the time scale of earth's rotation and the time scale of motion. If this ratio is large, then rotation can be neglected. This happens in very small scale and fast motions like turbulence in Figure. 2.1. For the slow, large-scale motions the Rossby number is small and then Earth's rotation is important. On the other hand, dissipation is very weak in the sense that the timescale for dissipation to act is long compared with both the timescale of Earths rotation and the timescale for the circulation to move water from one place to another.

Additionally, the shape, depth, and geographic location of a water parcel affects the general characteristics of its circulation. Smaller scale features, such as locations of deep sills and fracture zones, sea-mounts, and bottom roughness, as well as sub-sea features, strongly influences the ocean circulation. Ridges separate deep waters of the ocean into distinct basins. Water deeper than the sill between two basins cannot move from one to the other. Tens of thousands of sea-mounts are scattered throughout the ocean basins. They interrupt ocean currents, and produce turbulence leading

to vertical mixing in the ocean (*Stewart*, 2008 [106]). Marginal seas on the other hand, are large basins of salty water that are connected to the open ocean by one or more fairly narrow channels. The Mediterranean sea provides an example of a negative water balance in a sea with less inflow (river runoff and precipitation)than evaporation. At shallower depths sills (shallowest part of a channel) defining a marginal sea strongly influences both the mid-level currents and the distribution of water masses associated with the sea. Coastal upwelling is a direct consequence of the shape of the coast and its related bottom topography. Alongshore currents are often determined by the coastal bottom topography and the instabilities in the system can depend on the horizontal scales of the bottom topography. Near the shore bottom topography regulates the breaking of surface gravity waves and also directly influences local tides (*Talley*, 2011 [107]).

2.1.1 Equations of Motion.

In the ocean, the downward force of gravity is mostly balanced by an upward pressure gradient force; that is, the water is not accelerating downward. Instead, it is kept from collapsing by the upward pressure gradient force. Therefore pressure increases with increasing depth. This balance of downward gravity force and upward pressure gradient force, with no motion, is called *hydrostatic balance*. In a non-rotating fluid, a pressure difference between two points in the fluid drives the fluid toward the low pressure. In a fluid dominated by rotation, the flow can be geostrophic (see section. 2.1.3), perpendicular to the pressure gradient force, circling around centers of high or low pressure due to the Coriolis effect. So then, horizontal pressure gradients drive the horizontal flows in the ocean. This pressure gradient is much smaller than the vertical one, but the latter is balanced by the downward force of gravity and does not drive a flow (*Talley*, 2011 [107]).

Circulation in the ocean is often divided into two parts, the wind-driven and the thermohaline components. Wind blowing on the ocean initially causes small capillary waves and then a spectrum of waves and swell in the ocean. Impulsive changes in wind lead to short timescale inertial currents. Steady or much more slowly changing wind creates the oceans near-surface frictional Ekman layer(see section. 2.1.2.2), which involves the Coriolis effect. As the wind momentum transfer persists, the geostrophic, wind-driven circulation results.

The thermohaline circulation is associated with heating and cooling (thermo), and evaporation, precipitation, runoff, and sea ice formation which results in salinity changes (haline). Thermohaline-dominated circulation is weaker and slower compared with wind-driven circulation. Its forcing ranges from very local to very broad scale. The energy source for thermohaline circulation importantly includes the wind and

tides that produce the turbulence essential for the diffusive upwelling across isopycnals that closes the thermohaline overturning. Both the wind-driven and thermohaline circulations are almost completely in geostrophic balance, with the forcing that drives them occurring at higher order (*Talley*, 2011 [107]).

Fluid flow in three dimensions is governed by three equations expressing how velocity (or momentum) changes, one for each of the three physical dimensions. Each of the three momentum equations includes an acceleration term, an advection term and forcing terms. Since a fluid is continuous, the mass of a single object is replaced by the mass per unit volume (density); forces are also expressed per unit volume.

$$\text{Density} \times (\text{Acceleration} + \text{Advection}) = \text{Forces per unit volume} \tag{2.1}$$

$$\text{Forces per unit volume} = \text{Pressure gradient force} + \text{Gravity} - \text{Friction} \tag{2.2}$$

Expressions 2.1 and 2.2 are each three equations, one for each of the three dimensions. The terms in Eqs. 2.1 and 2.2 in Cartesian coordinates x, y, z (x and y are west-east and south-north, and z is upward), are illustrated in Figure 2.2.

The inclusion of advection means that Eq. 2.1 is the expression of momentum change in a Eulerian framework, where the observer sits at a fixed location relative to Earth. Equation 2.1 can be written without the advection term, in a Lagrangian framework, where the observer drifts along with the fluid flow.

For a rotating geophysical flow, the acceleration term on the left-hand side of Eq. 2.1 is rewritten to separate local acceleration due to an actual local force from the effects of rotation. The effects that are separated out are the centrifugal and Coriolis accelerations. The frictional force in Eq. 2.1 leads to dissipation of energy due to the fluid's viscosity.

The vector velocity is expressed in Cartesian coordinates as $\mathbf{u}= (u, v, w)$ where the bold u indicates a vector quantity, and u, v, and w are the positive eastward (x-direction), northward (y-direction) and positive upward (z-direction) velocities, then

$$\frac{\partial \mathbf{u}}{\partial t} = \frac{\partial u}{\partial t} + \frac{\partial v}{\partial t} + \frac{\partial w}{\partial t} \tag{2.3}$$

Advection is how the flow moves properties (including scalars such as temperature or salinity) and vectors (such as the velocity). It can change the flow properties if there is a gradient in the property through which the fluid moves. In the x-momentum equation, the advection term is,

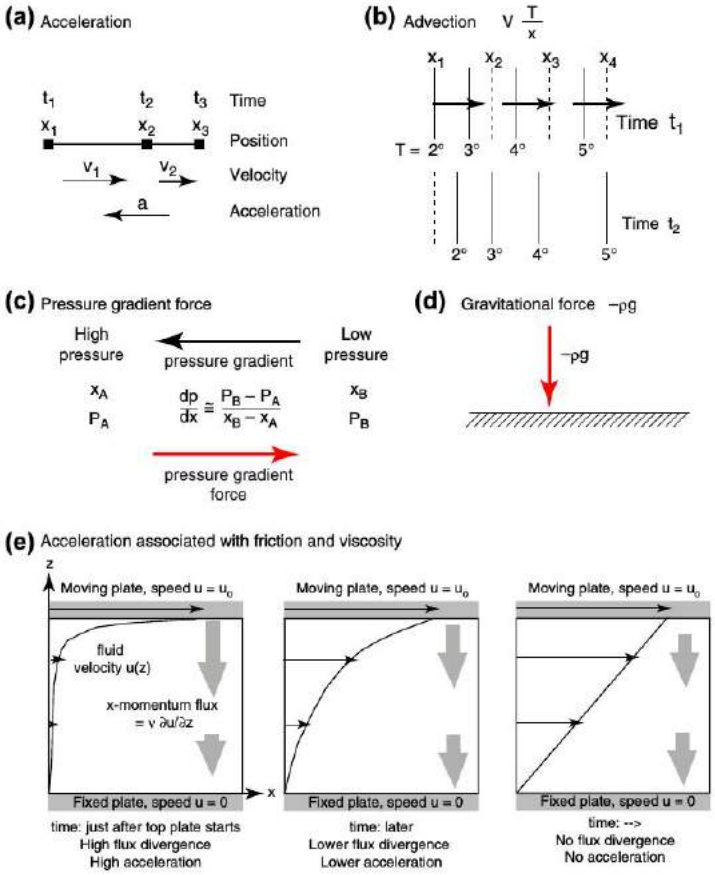

Figure 2.2: Forces and accelerations in a fluid: (a) acceleration, (b) advection, (c) pressure gradient force, (d) gravity, and (e) acceleration associated with viscosity ν (*Talley*, 2011 [107]).

$$x - \text{direction advection} = u\frac{\partial u}{\partial x} + v\frac{\partial u}{\partial y} + w\frac{\partial u}{\partial z} \tag{2.4}$$

The *substantial derivative* or *material derivative* is the sum of the acceleration and advection terms,

$$\frac{\mathrm{D}u}{\mathrm{D}t} = \frac{\partial u}{\partial t} + u\frac{\partial u}{\partial x} + v\frac{\partial u}{\partial y} + w\frac{\partial u}{\partial z} \tag{2.5}$$

In mathematical form, the pressure gradient force is,

$$x - \text{direction pressure gradient force} = \frac{-\partial \mathrm{p}}{\partial x} \tag{2.6}$$

Since the gravitational force between Earth and the object or fluid parcel is directed toward the center of mass of Earth. Gravitational force is mass of the object $\times$ gravitational acceleration g, equal to 9.780318 m^2/sec (at the equator). The gravitational force per unit volume is then,

$$z - \text{direction gravitational force per unit volume} = -\rho g \tag{2.7}$$

Centrifugal force is the apparent outward force on a mass when it is rotated. Since Earth rotates around a fixed axis, the direction of centrifugal force is always outward away from the axis, opposite to the direction of gravity at the equator; at Earths poles it is zero. The mathematical expression for centrifugal acceleration (force divided by density) is

$$\text{centrifugal acceleration} = \Omega^2 r \tag{2.8}$$

where U is the rotation rate of Earth, equal to 2π/T where T is the length of day, and r is the Earths radius. Because the centrifugal acceleration is nearly constant in time and points outward, away from Earths axis of rotation, we usually combine it formally with the gravitational force, which points toward Earths center. We replace g in Eq.2.7 with an effective gravity g, which has a weak dependence on latitude.

The second term in a rotating frame of reference included in the acceleration equation 2.1 is the Coriolis force. When a water parcel moves, Earth spins out from under it. Due to the Coriolis force the parcel of water moves to the right of its direction of motion in the Northern Hemisphere and to the left in the Southern Hemisphere. The Coriolis force is non-zero only if the body is in motion, and is important only if the body travels for a significant period of time. Mathematically, the Coriolis force is represented in the following equations,

$$x - \text{momentum equation: } -2\Omega \sin\varphi v \equiv -fv \tag{2.9a}$$

$$y - \text{momentum equation: } 2\Omega \sin\varphi u \equiv fv \tag{2.9b}$$

$$\text{Coriolis parameter: } f \equiv 2\Omega \sin\varphi \tag{2.9c}$$

where "$\equiv$" denotes a definition, Ω is the rotation rate, φ is latitude, u is velocity in the x-direction, v is velocity in the y-direction. The Coriolis parameter, f, is a function of latitude and changes sign at the equator, it has units of $\sec^{-1}$.

For a Newtonian fluid, and if viscosity has no spatial dependence, viscous stress enters the momentum equations as

$$x - \text{momentum dissipation} = \upsilon \left(\frac{\partial^2 u}{\partial x^2} + \frac{\partial^2 u}{\partial y^2} + \frac{\partial^2 u}{\partial z^2} \right) \tag{2.10}$$

where υ is the molecular (kinematic) viscosity. *Eddy viscosity* is introduced to account for a more efficient mixing. Eddy viscosity should be proportional to the product of turbulent speed and path length. Therefore, horizontal eddy viscosity is generally much larger than vertical eddy viscosity.

Mathematically, the viscous terms in Eqs. 2.1 and 2.10 are replaced by the eddy viscosity terms:

$$x - \text{momentum dissipation} = \mathrm{A}_H \left(\frac{\partial^2 u}{\partial x^2} + \frac{\partial^2 u}{\partial y^2} \right) + \mathrm{A}_V \left(\frac{\partial^2 u}{\partial z^2} \right) \tag{2.11}$$

where A_H is the horizontal eddy viscosity and A_V is the vertical eddy viscosity. A_H and A_v have units of kinematic viscosity, $\mathrm{m}^2/\mathrm{sec}$.

Temperature is changed by heating, cooling, and diffusion. Salinity is changed by addition or removal of freshwater, which alters the dilution of the salts. Density is then computed from temperature and salinity using the equation of state of seawater.

$$\rho(\mathrm{S}, \mathrm{T}, \mathrm{p}) = \frac{\rho(\mathrm{S}, \mathrm{T}, 0)}{\left[1 - \frac{\mathrm{p}}{K(\mathrm{S},\mathrm{T},\mathrm{p})} \right]} \tag{2.12}$$

The complete set of equations for temperature, salinity, and density forcing, plus the full momentum balance with spatially varying eddy viscosity and rotation are:

$$\frac{\mathrm{D}u}{\mathrm{D}t} - fv = \frac{\partial u}{\partial t} + u\frac{\partial u}{\partial x} + v\frac{\partial u}{\partial y} + w\frac{\partial u}{\partial z} - fv$$
$$= -\frac{1}{\rho}\frac{\partial \mathrm{p}}{\partial x} + \frac{\partial}{\partial x}\left(\mathrm{A}_H\frac{\partial u}{\partial x}\right) + \frac{\partial}{\partial y}\left(\mathrm{A}_H\frac{\partial u}{\partial y}\right) + \frac{\partial}{\partial z}\left(\mathrm{A}_V\frac{\partial u}{\partial z}\right) \quad (2.13a)$$

$$\frac{\mathrm{D}v}{\mathrm{D}t} + fv = \frac{\partial v}{\partial t} + u\frac{\partial v}{\partial x} + v\frac{\partial v}{\partial y} + w\frac{\partial v}{\partial z} + fv$$
$$= -\frac{1}{\rho}\frac{\partial \mathrm{p}}{\partial y} + \frac{\partial}{\partial x}\left(\mathrm{A}_H\frac{\partial v}{\partial x}\right) + \frac{\partial}{\partial y}\left(\mathrm{A}_H\frac{\partial v}{\partial y}\right) + \frac{\partial}{\partial z}\left(\mathrm{A}_V\frac{\partial v}{\partial z}\right) \quad (2.13b)$$

$$\frac{\mathrm{D}w}{\mathrm{D}t} = \frac{\partial w}{\partial t} + u\frac{\partial w}{\partial x} + v\frac{\partial w}{\partial y} + w\frac{\partial w}{\partial z}$$
$$= -\frac{1}{\rho}\frac{\partial \mathrm{p}}{\partial z} - g + \frac{\partial}{\partial x}\left(\mathrm{A}_H\frac{\partial w}{\partial x}\right) + \frac{\partial}{\partial y}\left(\mathrm{A}_H\frac{\partial w}{\partial y}\right) + \frac{\partial}{\partial z}\left(\mathrm{A}_V\frac{\partial w}{\partial z}\right) \quad (2.13c)$$

$$\frac{\mathrm{DT}}{\mathrm{D}t} = \frac{\partial \mathrm{T}}{\partial t} + u\frac{\partial \mathrm{T}}{\partial x} + v\frac{\partial \mathrm{T}}{\partial y} + w\frac{\partial \mathrm{T}}{\partial z}$$
$$= \frac{\mathrm{Q}_H}{\rho C_p} + \frac{\partial}{\partial x}\left(\kappa_H\frac{\partial \mathrm{T}}{\partial x}\right) + \frac{\partial}{\partial y}\left(\kappa_H\frac{\partial \mathrm{T}}{\partial y}\right) + \frac{\partial}{\partial z}\left(\kappa_V\frac{\partial \mathrm{T}}{\partial z}\right) \quad (2.13d)$$

$$\frac{\mathrm{DS}}{\mathrm{D}t} = \frac{\partial \mathrm{S}}{\partial t} + u\frac{\partial \mathrm{S}}{\partial x} + v\frac{\partial \mathrm{S}}{\partial y} + w\frac{\partial \mathrm{S}}{\partial z}$$
$$= \mathrm{Q}_S + \frac{\partial}{\partial x}\left(\kappa_H\frac{\partial \mathrm{S}}{\partial x}\right) + \frac{\partial}{\partial y}\left(\kappa_H\frac{\partial \mathrm{S}}{\partial y}\right) + \frac{\partial}{\partial z}\left(\kappa_V\frac{\partial \mathrm{S}}{\partial z}\right) \quad (2.13e)$$

$$\rho = \rho(\mathrm{S},\mathrm{T},\mathrm{P}) \quad (2.13f)$$

$$\frac{\mathrm{D}\rho}{\mathrm{D}t} = \frac{\partial \rho}{\partial t} + u\frac{\partial \rho}{\partial x} + v\frac{\partial \rho}{\partial y} + w\frac{\partial \rho}{\partial z}$$
$$= \left(\frac{\partial \rho}{\partial \mathrm{S}}\right)\frac{\mathrm{S}}{\mathrm{t}} + \left(\frac{\partial \rho}{\partial \mathrm{T}}\right)\frac{\mathrm{T}}{\mathrm{t}} + \left(\frac{\partial \rho}{\partial \mathrm{P}}\right)\frac{\mathrm{P}}{\mathrm{t}} \quad (2.13g)$$

$$\frac{\mathrm{D}\rho}{\partial t} + \rho\left(\frac{\partial u}{\partial x} + \frac{\partial v}{\partial y} + \frac{\partial w}{\partial z}\right) = 0 \qquad \text{if density changes are small then,} \quad (2.13h)$$

$$\frac{\partial u}{\partial x} + \frac{\partial v}{\partial y} + \frac{\partial w}{\partial z} = 0 \qquad \text{(continuity equation)} \quad (2.13i)$$

In which, Equation. 2.13d represents the temperature change + the temperature advection/convection = heating cooling term Q_H (heat source, positive for heating negative for cooling) + the diffusive term. C_p, represent the specific heat of sea water. Equation. 2.13e represents the salinity change + salinity advection/convection = evaporation/precipitation/runoff + diffusion, Q_S is the salinity source (positive for evaporation, negative for precipitation and runoff). κ_H and κ_V are the horizontal and vertical eddy diffusivity, analogous to the horizontal and vertical eddy viscosities in the momentum equations (2.13 abc). The full equation of state appears in Eq. (2.13f), from which the evolution of density in terms of temperature and salinity change can be computed (Eq. 2.13g). The coefficients for the three terms in Eq.

2.13g are the haline contraction coefficient, the thermal expansion coefficient, and the adiabatic compressibility (*Talley*, 2011 [107]).

For the full set of equations describing the physical state of the ocean, it should be included the continuity (or mass conservation) equation (2.13h). If density changes are small, Eq. 2.13h is approximated as Eq. 2.13i, which is known as the continuity equation.

2.1.2 Wind forcing

Wind blowing over the ocean exerts stresses that set the water in motion. The net effect of atmospheric momentum exchanges with the ocean surface input stress in the ocean (wind stress), where for time scales of about 1 day or longer, Coriolis effect plays an important role.

2.1.2.1 Inertial currents

At time scales about a day, the ocean responds to the action of wind stress with short term motions known as "Inertial currents". These structures are the result of a balance between the Coriolis force and the time derivatives of the initial horizontal velocities produced by the wind stress.

Eq. 2.13 for a parcel of water moving in the ocean without friction is represented mathematically by,

$$\frac{du}{dt} = -\frac{1}{\rho}\frac{\partial \mathrm{P}}{\partial x} + 2\Omega v \sin\varphi \tag{2.14a}$$

$$\frac{dv}{dt} = -\frac{1}{\rho}\frac{\partial \mathrm{P}}{\partial y} - 2\Omega u \sin\varphi \tag{2.14b}$$

$$\frac{dw}{dt} = -\frac{1}{\rho}\frac{\partial \mathrm{P}}{\partial z} + 2\Omega u \cos\varphi - g \tag{2.14c}$$

If the only force acting over the fluid is the Coriolis force, then no horizontal pressure gradient in present so,

$$\frac{\partial \mathrm{P}}{\partial x} = \frac{\partial \mathrm{P}}{\partial y} = 0 \tag{2.15}$$

we can assume that the flow is horizontal and Eq. 2.14 becomes,

$$\frac{du}{dt} = 2\Omega \sin\varphi = fv \tag{2.16a}$$

$$\frac{dv}{dt} = -2\Omega \sin\varphi = -fu \tag{2.16b}$$

where, $f = 2\Omega \sin \varphi$ is the Coriolis parameter (as mentioned in section. 2.1.1). Eq. 2.16 are two coupled first order, linear, differential equations. If we solve for u and insert in Eq. 2.16a, we obtain:

$$\frac{du}{dt} = \frac{1}{f}\frac{d^2v}{dt^2} = fv \tag{2.17}$$

rearranging the equation we can recognize the equation of and harmonic oscillator as follows,

$$\frac{d^2v}{dt^2} + f^2v = 0 \tag{2.18}$$

with solutions,

$$u = \mathrm{V} \sin ft \tag{2.19a}$$
$$v = \mathrm{V} \cos ft \tag{2.19b}$$
$$\mathrm{V} = u^2 + v^2 \tag{2.19c}$$

called inertial currents or inertial oscillation.

In the northern hemisphere, the water particles deflects in clockwise circles whereas in the southern hemisphere, inertial currents are counterclockwise.The current will oscillate after several days around and then settling frictionally to a steady flow (*Stewart*, 2008 [106]; *Talley et. al*, 2011 [107]).

2.1.2.2 Ekman Layers

Steady winds blowing over the sea surface produce a thin boundary layer. This wind-driven frictional layer is called the Ekman layer. The physical processes in this layer include only friction (eddy viscosity) and Coriolis acceleration. If the eddy viscosity is independent of depth, the angle between wind and surface currents is 45 degrees to the right of the wind in the northern hemisphere (to the left in the southern).

Due to frictional stress proportional to the eddy viscosity, A_v, each layer from the surface on down accelerates the next layer below to the right (Northern hemisphere) and has a weaker velocity that the layer above it. As a result, the complete structure is a decaying spiral (Figure. 2.3).

If we assume a steady, homogeneous, horizontal flow with friction on a rotating earth, then horizontal and temporal derivatives are zero,

$$\frac{\partial}{\partial t} = \frac{\partial}{\partial x} = \frac{\partial}{\partial y} = 0 \tag{2.20}$$

This leaves a balance between friction and the Coriolis force,

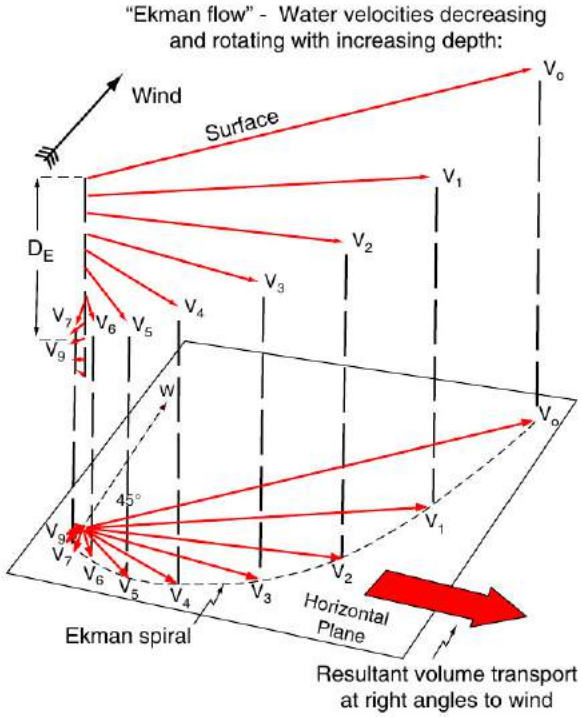

Figure 2.3: Ekman layer velocities (Northern Hemisphere). Water velocity as a function of depth (upper projection) and Ekman spiral (lower projection). The large open arrow shows the direction of the total Ekman transport, which is perpendicular to the wind (*Talley et. al*, 2011 [107]).

$$\tau_{xz} = \rho A_V \frac{\partial u}{\partial z}, \qquad \tau_{yz} = \rho A_V \frac{\partial v}{\partial z} \tag{2.21}$$

where τ_{xz} and τ_{yz} are the components of wind stress in the x and y directions. The x and y equations are,

$$fv + A_V \frac{\partial^2 u}{\partial z^2} = 0 - fu + A_V \frac{\partial^2 v}{\partial z^2} = 0 \tag{2.22a}$$

with solutions,

$$u = V_0 e^{az} \cos(\pi/4 + az) \tag{2.23a}$$
$$v = V_0 e^{az} \sin(\pi/4 + az) \tag{2.23b}$$

when the wind is blowing to the north ($\tau = \tau_{yz}$). The constants are:

$$V_0 = \frac{\tau}{\sqrt{(\rho^2 f A_V)}}, \qquad \text{and} \qquad a = \sqrt{\frac{f}{2A_z}} \tag{2.24}$$

Ekman proposed that the thickness of the layer is the depth D_E at which the current velocity is opposite to the velocity at the surface. This occurs at a depth $D_E = \pi/4$ so the Ekman layer depth is,

$$D_E = \sqrt{\frac{2\pi^2 A_V}{f}} \tag{2.25}$$

When wind stress varies with position and therefore, Ekman transport, there can be a convergence or divergence of water within the Ekman layer. Convergence results in *downwelling* of water out of the Ekman layer. Divergence results in *upwelling* into the Ekman layer. This is the mechanism that connects the frictional forcing by wind of the surface with the interior geostrophic ocean circulation (Fig. 2.4).

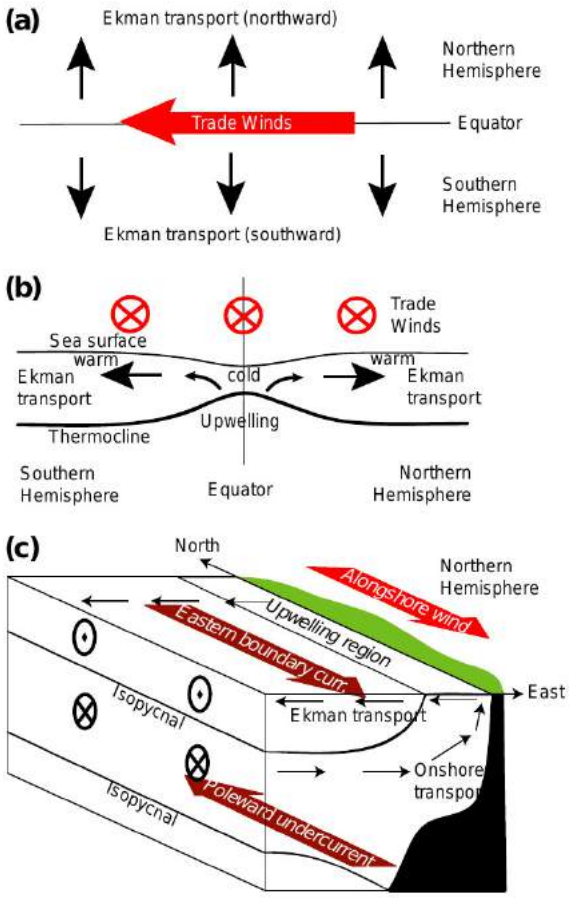

Figure 2.4: Ekman transport divergence near the equator driven by easterly Trade Winds. (b) The effect of equatorial Ekman transport divergence on the surface height, thermocline, and surface temperature. (c) Coastal upwelling system due to an alongshore wind with offshore Ekman transport (Northern Hemisphere) *Talley et. al*, 2011 [107].

In the northern hemisphere ($f > 0$) upwelling into the Ekman layer results from positive wind stress curl and downwelling from negative wind stress curl. Downwelling

is refereed as Ekman pumping and Upwelling is sometimes refereed as Ekman suction. On the other hand, in the coastline is also a place where Ekman transport can be developed but in this case (like in this thesis case) divergence/convergence is due to the boundary conditions at the coast as well. If the wind blows along the coast, the Ekman transport is perpendicular to the coast so there must be either downwelling or upwelling at the coast to feed the Ekman layer. This mechanism is called coastal upwelling (Fig. 2.4c) a more detailed description can be found in *Pickett and Paduan*, 2003 [85].

2.1.3 Geostrophic Currents

For the scales longer than several days and at spatial scales of several kilometers, the balance of the forces in the horizontal reduces to the balance between the horizontal pressure gradient and the Coriolis force. This is known as geostrophy or geostrophic balance and it is depicted in Fig. 2.5

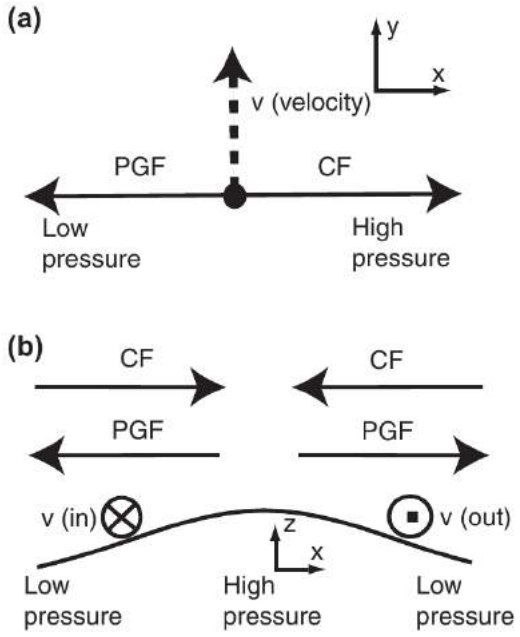

Figure 2.5: Geostrophic balance: horizontal forces and velocity. (a) Horizontal forces and velocity in geostrophic balance. PGF=pressure gradient force. CF=Coriolis force. (b) Side view showing elevated pressure (sea surface) in center, low pressure on sides, balance of PGF and CF, and direction of velocity v (into and out of page) *Talley et. al*, 2011 [107].

Here the pressure gradient force vector points from high to low pressure. Due to the presence of rotation, the Coriolis force exactly compensates the pressure gradient force so the net force is zero. Thus the water parcel does not accelerate (relative to earth). The parcel moves exactly perpendicular to both forces.

Assuming that the fluid is stationary and that there is no friction then,

$$u = v = w = 0, \qquad \text{then} \qquad \frac{du}{dt} = \frac{dv}{dt} = \frac{dw}{dt} = 0 \tag{2.26}$$

$$\mathrm{F}_x = \mathrm{F}_y = \mathrm{F}_z = 0 \qquad \text{(no friction)} \tag{2.27}$$

with these assumptions the momentum equations (Eq. 2.13) become,

$$\frac{1}{\rho}\frac{\partial \mathrm{P}}{\partial x} = 0, \tag{2.28a}$$

$$\frac{1}{\rho}\frac{\partial \mathrm{P}}{\partial y} = 0, \tag{2.28b}$$

$$\frac{1}{\rho}\frac{\partial \mathrm{P}}{\partial z} = -g(\varphi, z) \qquad \text{Hydrostatic balance.} \tag{2.28c}$$

$$\tag{2.28d}$$

where g is a function of the latitude φ and the height z. In this case the ocean is at rest, or the flow velocity at each point is constant over time and external forces such as gravity are balanced by a pressure gradient force.

The geostrophic balance requires that the Coriolis force balances the horizontal pressure gradient. Then the vertical pressure gradient force, which points upward from high to low pressure, is balanced by gravity, which points downward (hydrostatic balance). Assuming the flow has no acceleration i.e, $\frac{du}{dt} = \frac{dv}{dt} = \frac{dw}{dt} = 0$, then horizontal velocities are much longer than vertical: $w \ll u, v$. The only external force is gravity and that friction is small. Then Eq. 2.13a, b, c become,

$$\frac{\partial \mathrm{P}}{\partial x} = \rho f v \tag{2.29a}$$

$$\frac{\partial \mathrm{P}}{\partial y} = -\rho f u \tag{2.29b}$$

$$\frac{\partial \mathrm{P}}{\partial z} = -\rho g \tag{2.29c}$$

These equations represent the geostrophic balance. If the Coriolis parameter is approximately constant ($f = f_0$), the geostrophic velocities are approximately non-divergent:

$$\frac{\partial u}{\partial x} + \frac{\partial v}{\partial y} = 0 \tag{2.30}$$

such non-divergent velocity field can be written in terms of a stream function ψ,

$$u = -\frac{\partial \psi}{\partial y} \qquad \text{and} \qquad u = \frac{\partial \psi}{\partial x}. \tag{2.31}$$

From Eq. 2.29 a and b, the stream function for a geostrophic flow is $\psi = \frac{\mathrm{P}}{f_0 P_0}$. Therefore, maps of pressure distribution (or dynamic height) are maps of the geostrophic stream function, and the flow approximately follows the mapped contours. In those maps low pressure regions are called *cyclones* and if the flow flows around low pressure regimes is called the *cyclonic* (or counterclockwise in the northern hemisphere and clockwise in the southern hemisphere). Flow around high pressure regions is called *anticyclonic* (*Talley*, 2011 [107]).

Eq. 2.29 can be rewritten as,

$$u = -\frac{1}{f\rho}\frac{\partial \mathrm{P}}{\partial y}; \qquad v = \frac{1}{f\rho}\frac{\partial \mathrm{P}}{\partial x} \tag{2.32a}$$

$$\mathrm{P} = \mathrm{P}_0 + \int_{-h}^{\zeta} g(\varphi, z)\rho(z)dz \tag{2.32b}$$

where P_0 is the atmospheric pressure at $z = 0$ and ζ is the sea surface height. In this case, the sea surface is allowed to be above or below the surface $z = 0$ and the pressure gradient at the sea surface is balanced by a surface current u_s.

Substituting Eq. 2.32 b into 2.32 a, and using the Buosinesq approximation yields,

$$\begin{aligned} u &= -\frac{1}{f\rho}\frac{\partial}{\partial y}\int_{-h}^{0} g(\varphi, z)\rho(z)dz - \frac{g}{f}\frac{\partial \zeta}{\partial y} \\ &= -\frac{1}{f\rho}\frac{\partial}{\partial y}\int_{-h}^{0} g(\varphi, z)\rho(z)dz - u_s \end{aligned} \tag{2.33a}$$

$$\begin{aligned} v &= \frac{1}{f\rho}\frac{\partial}{\partial x}\int_{-h}^{0} g(\varphi, z)\rho(z)dz - \frac{g}{f}\frac{\partial \zeta}{\partial x} \\ &= \frac{1}{f\rho}\frac{\partial}{\partial x}\int_{-h}^{0} g(\varphi, z)\rho(z)dz - v_s \end{aligned} \tag{2.33b}$$

If the ocean is homogeneous, ρ and g are constants, then the first term on the right hand side of Eq. 2.33 is zero and the horizontal pressure gradients within the ocean are the same as the gradients at $z = 0$ and it is known as *Barothropic* flow. On the other hand if the Ocean is stratified, then the horizontal pressure gradient has two terms, one due to the slope at the sea surface and an additional term due to horizontal density differences; those equations represent the *Baroclinic* flow. The first term in Eq. 2.33 is due to variations in density distribution and requires the velocity (u_0, v_0) at the sea surface or at some depth (*Stewart*, 2008 [106]).

2.1.4 Surface Geostrophic Currents from Altimetry

Geostrophic velocities at the sea surface can be calculated from satellite altimetry by means of the sea surface height ζ as follows. The geostrophic approximation applied at $z = 0$ leads to the relation that surface geostrophic currents are proportional to the surface slope. The pressure on the level surface is:

$$\mathrm{P} = \rho g(\zeta + r) \tag{2.34}$$

assuming ρ and g constant in the upper few meters of the ocean. Then substituting Eq. 2.34 into Eq. 2.29 gives the two components of the surface geostrophic current.

$$u_g = -\frac{g}{f}\frac{\partial \zeta}{\partial y}, \qquad \text{and} \qquad v_g = \frac{g}{f}\frac{\partial \zeta}{\partial x} \tag{2.35}$$

where ζ is the sea surface height above a level surface. In this way we are able to calculate the geostrophic currents from satellite altimetry data, which is going to be discussed in the next chapter.

2.2 Datasets and methods

2.2.1 High Frequency Radar

High frequency radar is a short base remote sensing technique that permits continuous monitoring of sea surface currents at distance up to 100 Km from shore, with high resolution in time (10 min to 3 hours) and space (500 m to 6 km). The measuring technique thus provides useful information to study impacts on social relevant issues such as search and rescue operations, coastal pollution, transport of material, oil spills and its mitigation, beach erosion, and air-sea interaction studies.

As *Harlan et al.*, 2010 [42] described, HF belongs to the part of the electromagnetic spectrum having frequencies from 3 to 30 MHz, which is equivalent to radio wavelengths between 10 to 100 m. HF radar has been shown to be the optimal method for coastal sea surface mapping for certain number of reasons.

1. Targets required to produce coherent sea echo using HF are surface gravity waves, usually of several to few tens of meter wavelength. which are well understood and nearly always present in the open ocean.

2. Vertically polarized HF waves can propagate over conductive sea water via coupling to the mean spherical surface, producing measurement ranges beyond line-of-sight out to 200 Km or more offshore.

3. Doppler sea echo at HF under most wave conditions, has a well-defined signal from wave -wave processes. This allows for robust extraction of current velocities.

It is primarily these 3 factors, along with the spatial resolutions that are possible due to the frequency modulation that place the HF band in an unique status for coastal current monitoring (*Harlan et al.*, 2010 [42]).

The basic technique of HF radar systems consist on the analysis of a backscattered radio wave from ocean waves. A transmit antenna sends radio-wave signals to the ocean and then perform an analysis of the energy backscattered by resonant surface waves or "Bragg waves" of one-half the incident radar wavelength (Eq. 2.36) traveling on the sea surface,

$$\Lambda = \lambda/2 \sin\theta_i, \tag{2.36}$$

where Λ is the wavelength of the Bragg waves, λ is the radar wavelength and θ_i is the incidence angle. For shore-based HF radar system, $\theta_i = 90°$ so Λ in this case is equal to $\lambda/2$. This Bragg scattering effect results in two discrete and well-defined peaks in the Doppler spectrum (Figure. 2.6). In the absence of a surface current, the position of these peaks are symmetric with frequency (f_B) offset from the origin by an amount proportional to $2C_0\lambda^{-1}$, where $C_0 = \sqrt{g\Lambda/2\pi}$, represents the linear phase speed of the surface Bragg wave in deep water and g is the acceleration of gravity (*Graber et al.*, 1997.[38]).

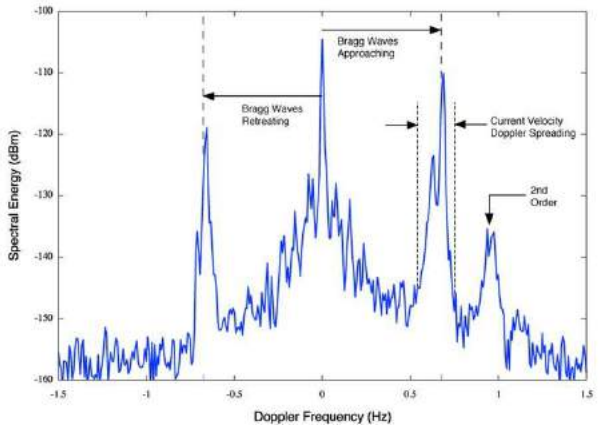

Figure 2.6: Representative HF radar Doppler spectrum *Harlan et al.*, 2010 [42]).

A current underlying the surface waves causes a translation of the entire coordinate frame with respect to a stationary observer or a radar station on shore. Thus the Bragg peaks in the Doppler spectra are displaced from the Bragg frequency f_B by an amount,

$$\Delta f = \frac{2V_r}{\lambda}, \tag{2.37}$$

where V_r is the radial component of the effective surface current along the look direction of the radar. Thus, to resolve the two-dimensional (2-D) current fields, two radar stations are required where their separation determines the domain of the mapped region.

While the accuracy of the measurement is a maximum for an angle of intersection of 90° between the two radar beams, the error in resolving the current vectors increases as the intersection angle departs from this optimal value. Figure. 2.7 shows how to compute the vector current at a given intersection point of two radar beams or radials. The velocity components parallel (V_p) and normal (V_n) to the two intersecting radials can be expressed in terms of the radial velocity components R_1 and R_1 originated from two stations observing the same area,

$$V_p = \frac{R_1 + R_2}{2\cos(\Delta/2)}, \tag{2.38}$$

$$V_n = \frac{R_1 - R_2}{2\sin(\Delta/2)}. \tag{2.39}$$

with,

$$\Delta = \theta_2 - \theta_1, \tag{2.40}$$

where θ_1 and θ_2 represent bearing angles of the radials (*Graber et al.*, 1997.[38])

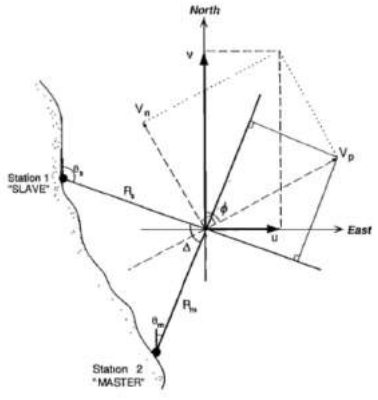

Figure 2.7: Schematic for determining the resulting vector current from velocity components of two intersecting radials (*Graber et al.*, 1997.[38]).

The horizontal components i.e, east and north components of the velocity vector $U(u, v)$ can then be expressed as:

$$u = V_p \sin\phi + V_n \cos\phi, \tag{2.41}$$

$$v = V_p \cos\phi + V_n \sin\phi, \tag{2.42}$$

where,

$$\phi = \frac{\theta_2 + \theta_1}{2}, \tag{2.43}$$

is the angle of the bisector of the radar beams measured clockwise from true north. Substitution of Eq. (2.38) and (2.39) into (2.41) and (2.42) yields,

$$u = \frac{R_1 \cos\theta_2 - R_2 \cos\theta_1}{\sin\Delta}, \tag{2.44}$$

$$v = \frac{R_2 \sin\theta_1 - R_1 \sin\theta_2}{\sin\Delta}. \tag{2.45}$$

For angles Δ less than 30°, generally, no vector currents are computed because errors are inversely proportional to the angle of intersection. However, under certain circumstances (e.g., the current is aligned along one of the radials) this value can be relaxed and reduced to 15°. This geometric criterion is used to eliminate very sharp and shallow angles between two radials.

On the other hand, The Coastal Ocean Dynamics Applications Radar, CODAR, is a portable HF radar system that allows to measure and map Near-Surface currents in coastal waters. CODAR utilizes a three-element crossed-loop/monopole antennae system and direction-finding techniques that are easily deployed in small, confined areas compared to the beach real estate required for the length of the phased array. The azimuthal resolution of the current field is based on a least-squares fit of the Fourier series to the data. Thus, the current resolution tends to be more sensitive to beam patterns in direction-finding algorithms (*Emery et al.*, 1997 [29]).

Hourly real-time high frequency radar data from three CODAR SeaSondes installed in Ta'Sopu (Malta), Ta'Barkat (Malta) and Pozzallo Harbor (Sicily, Italy) (Figure.2.8) provided surface current maps in the Malta-Sicily channel from the period August 2012 to January 2015. Those hourly data are organized in time series of hourly averaged velocity vectors with u (Meridional, East-West) and v (Latitudinal, North-South) components of the total velocity. The datasets were provided by Dr. Aldo Drago from the University of Malta and were collected as part of the partially sponsored European Unions Italia-Malta Calypso project (see [16] for more information). The project aims to routinely monitor sea surface currents in the region to optimize interventions in case of oil spill response and emergency situations, and to more generally monitor sea conditions in this area of the Mediterranean Sea (*Cosoli*

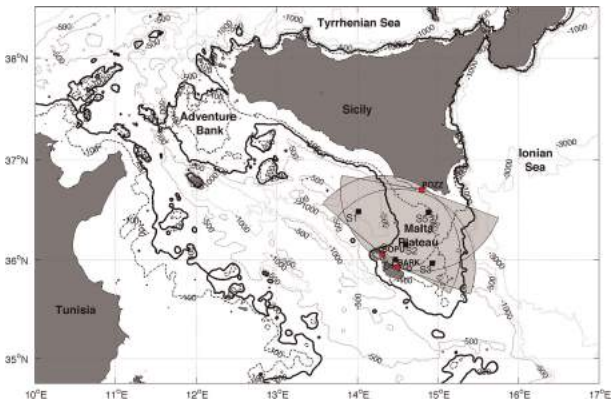

Figure 2.8: High frequency radar stations of three CODAR SeaSondes at Ta'Sopu (Malta), Ta'Barkat (Malta) and Pozzallo Harbor (Sicily, Italy) from [16] (*Cosoli et al.*, 2015 [23]).

et al., 2015 [23]) The CALYPSO system operating set-up and resolution (13.5 MHz frequency, angular resolution 5°, range resolution 1.6 Km), provides radar measurements that are representative of the first meter of the ocean surface, with grid sizes in the range of 0.3-8.3 Km^2. The radars share the same transmit frequency using a GPS-synchronization module, and operate with both the ideal and measured antenna beam patterns. Hourly sea surface current maps are derived on a Cartesian grid with 3x3 km^2 horizontal resolution by least-squares fitting of the radial components of the ocean currents from two or more radar stations in areas of common overlap (*Cosoli et al.*, 2015 [23]).

2.2.2 Mediterranean Sea (M)ADT - Absolute Dynamic Topography

MADT Ssalto/Duacs multi-mission L4 altimeter products available from January 1993 to December 2015 containing multi-mission surface heights above geoid, gridded ($1/8° \times 1/8°$ on a regular grid); were used to compute dynamic topography maps which is the sum of sea level anomaly (M)SLA and mean dynamic topography. For this dataset the Copernicus Marine and Environment Monitoring Service (CMEMS) has taken over the whole processing and distribution of those products (formerly distributed by Aviso+ with no change in the scientific content).

The geographic coverage includes Mediterranean Sea, in which for this thesis a subset of the original grid between 32-40°N and 9-18°E is taken for our studies. All the missions are homogenized with respect to a reference mission which is currently OSTM/Jason-2. The SLA is computed with an optimal and centered computation time window (6 weeks before and after the date). This product is processed by the SL-TAC multi-mission altimeter data processing system. It processes data from all altimeter missions: Jason-3, Sentinel-3A, HY-2A, Saral/AltiKa, Cryosat-2, Jason-2,

Jason-1, T/P, ENVISAT, GFO and ERS1/2. The system acquires and then synchronizes altimeter data and auxiliary data; where each mission is homogenized using the same models and corrections. The Input Data Quality Control checks that the system uses the best altimeter data. The multi-mission cross-calibration process removes any residual orbit error, or long wavelength error (LWE), as well as large scale biases and discrepancies between various data flows; all altimeter fields are interpolated at crossover locations and dates. After a repeat-track analysis, a mean profile, which is peculiar to each mission, or a Mean Sea Surface (MSS) (when the orbit is non repetitive) is subtracted to compute sea level anomaly. Data are then cross validated, filtered from residual noise and small scale signals, and finally subsampled. Finally an Optimal Interpolation is made merging all the flying satellites in order to compute gridded SLA. The ADT (Absolute Dynamic Topography) is then computed as follows: $adt = sla + MDT$ where MDT is the Mean Dynamic Topography distributed by Aviso+ (`http://www.aviso.altimetry.fr/en/data/products/auxiliary-products/mdt.html`). The errors have been estimated to be lower than 3 mm/yr at regional scale. Sea level errors for mesoscales vary between 1.4 cm^2 in low variability areas to more than 30 cm^2 in high variability areas [22].

The Altimetry gives access to the Sea Surface Height (SSH) above the reference ellipsoid (Figure 2.9),

$$\text{SSH} = \text{Orbit - Altimetric Range}$$

The Mean Sea Surface (MSS_N) is the temporal mean of the SSH over a period N. It is a mean surface above the ellipsoid of reference and it includes the Geoid.

$$\text{MSS}_\text{N} = <\text{SSH}>_\text{N}$$

The Sea Level Anomaly (SLA_N) is the anomaly of the signal around the mean component. It is deduced from the SSH and MSS_N:

$$\text{SLA}_\text{N} = \text{SSH} \quad \text{MSS}_\text{N}$$

The Mean Dynamic Topography (MDT_N) is the temporal mean of the SSH above the Geoid over a period N.

$$\text{MDT}_\text{N} = \text{MSS}_\text{N} \quad \text{Geoid}$$

The Absolute Dynamic Topography (ADT) is the instantaneous height above the Geoid. Then, when the ocean is also influenced by wind, differential heating and precipitation and other sources of energy, the ocean surface moves from the geoid. Thus, the departure from the geoid provides information on the ocean dynamics.

The ADT is the sum of the SLAN and MDT_N:

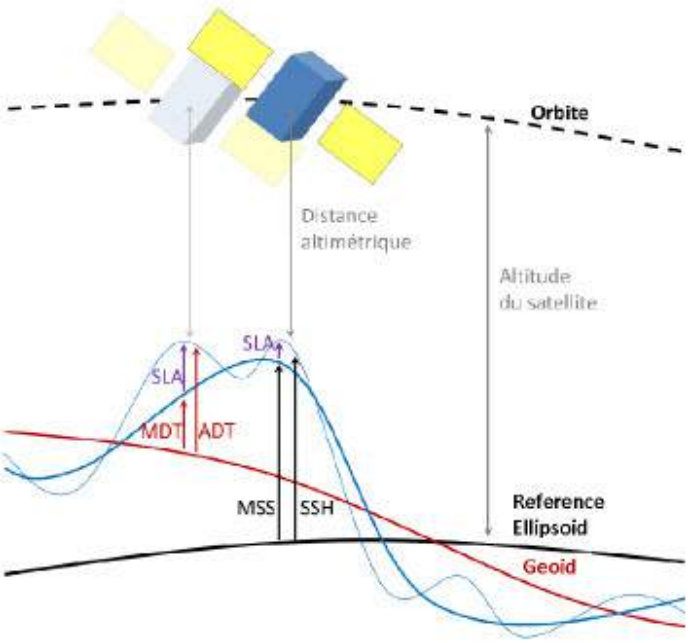

Figure 2.9: Different notions of sea surface height used in altimetry (Copernicus CMEMS-SL-QUID-008-032-051 catalog [22]).

$$\text{ADT} = \text{SLA}_\text{N} + \text{MDT}_\text{N} = \text{SSH} - \text{MSS}_\text{N} + \text{MDT}_\text{N}$$

The L4 product generation processing methodology consists in an optimal interpolation processing as fully synthesized in *Pujol et al.*, 2016 [89]. Here the main source of error comes from the sampling capability of the altimeter constellation. The more altimeters are available, the best is the mesoscale sampling. Another source of error for L4 products is directly linked to the methodologies and parameters applied for SLA interpolation on a regular grid (*Chelton et al.*, 2011 [18]).

Geostrophic currents were calculated form the MADT datasets (as in section. 2.1.3) over the period previously mentioned and will be analyzed in Chapter. **??**. Due to the small Rossby radius of deformation in the Mediterranean Sea (15-20 km according to Robinson et al, 2001 [93]), the typical mesoscale features are characterized by scales of the order of 10-100 km (*Malanotte and Robinson*, 2012 [61]). On the other hand, Eddy Kinetic Energy (EKE) was computed in order to measure the degree of the variability of the area under study. It is calculated as follows using the geostrophic approximation,

$$EKE = \frac{1}{2}\left[U_g'^2 + V_g'^2\right] \tag{2.46}$$

where,

$$U_g'^2 = -\frac{g}{f}\frac{\partial \zeta'}{\partial y} \tag{2.47a}$$

$$V_g'^2 = \frac{g}{f}\frac{\partial \zeta'}{\partial x} \tag{2.47b}$$

$$\tag{2.47c}$$

are the zonal and meridional geostrophic velocities and ζ' denotes the surface dynamic topography provided by the altimeter. Since the EKE is a measure of the degree of variability, this can help us to identify highly variable phenomena such as eddies or current meanders (*Borzelli et al.*, 2014[15]).

2.2.2.1 Empirical Orthogonal Functions - EOFs

EOF is an useful way of organizing information. Here we use EOF analysis on the MADT time series in order to characterize the Sicily channel and its variability. To do this, we represent the information of the time series in a different set of orthogonal functions to characterize the time series (instead of the sin and cos in the Fourier analysis). A set of functions with jumps in them could allow us to characterize the time series primarily with the lower-order functions. Here, the appropriate set of orthogonal functions are empirically determined from the time series itself.

Gridded climate data in general comes as an array containing for each vertical level a 3-dimensional in space and 1-dimensional in time, field F. The later is a function of time t, latitude θ, and longitude φ. We suppose that the horizontal coordinates are discretized to yield latitudes θ_j where $j = 1, ..., p_1$ and longitudes φ_k with $k = 1, ..., p_2$, similarly for time, i.e. t_i where $i = 1, ..., n$. This yields a total number of grid points $p = p_1 p_2$. The discretized field reads:

$$F_{i,j,k} = F(t_i, \theta_j, \varphi_k), \tag{2.48}$$

with $1 \leq i \leq n,\ 1 \leq j \leq p_1$, and $1 \leq k \leq p_2$. It is generally memory consuming to process three and higher dimensional arrays such as F. Therefore we transform F into a 2-dimensional array, the *data matrix* X where the two spatial dimensions are concatenated together.

Now we have the gridded data set which is composed by a space-time field $X(t, s)$ representing the value of the field X (like SSH), at time t and spatial position s. The value of the field at discrete time t_i and grid points s_j is noted x_{ij} for $i = 1, ..., n$ and $j = 1, ..., p = p_1 p_2$. The observed field is then represented by the data matrix:

$$X_{ij} = \begin{pmatrix} x_{11} & x_{12} & \dots & x_{1p} \\ x_{21} & x_{22} & \dots & x_{2p} \\ \vdots & \vdots & & \vdots \\ x_{n1} & x_{n2} & \dots & x_{np} \end{pmatrix} \tag{2.49}$$

If $\bar{x}_{.j}$ is the time average of the field[1] at the jth grid point, i.e.

$$\bar{x}_{.j} = \frac{1}{n} \sum_{k=1}^{n} x_{ij} \tag{2.50}$$

then the climatology of the field is defined by

$$\bar{\mathbf{x}} = (\bar{x}_{.1}, ..., \bar{x}_{.p}) \tag{2.51}$$

the anomaly field, or departure from the climatology is defined at (t, s) by:

$$x'_{ts} = x_{ts} - \bar{x}_{.s} \tag{2.52}$$

or in the matrix form:

$$X' = X - \mathbf{1}\bar{\mathbf{x}} = \left(I - \frac{1}{n} \mathbf{1}\mathbf{1}^T \right) X \tag{2.53}$$

where $\mathbf{1} = (1, ..., 1)^T$ is the (column) vector containing n ones, and I is the $n \times n$ identity matrix.

Empirical orthogonal functions technique aims to find a new set of variables that capture most of the observed variance from the data through a linear combination of the original variables. EOFs have been introduced in climatic sciences since the early 50's (*Obukhov*, 1947, 1960 [71] [72]; *Fukuoka*, 1951 [32]; *Lorenz*, 1956[60]; *Craddock*, 1973 [24]). Its terminology was first introduce by *Lorenz*, 1956 [60] who applied it in a forecasting project at the MIT.

- **Derivation of EOFs**

Once the anomaly data matrix Eq.2.53 is determined, we should define the covariance matrix,

$$\Sigma = \frac{1}{n-1} X'^T X', \tag{2.54}$$

which contains the covariance between any pair of grid points. The aim of EOF is to find the linear combination of all the variables, i.e. grid points, that explain

[1] Here the seasonal and other external cycles are supposed to have been removed from the data

maximum variance. That is to find a direction $\mathbf{a} = (a_1, ..., a_p)^T$ such that $X'\mathbf{a}$ has maximum variability. Now the variance of the (centered) time series $X'\mathbf{a}$ is

$$\text{var}(X'\mathbf{a}) = \frac{1}{n-1} \parallel X'\mathbf{a} \parallel^2 = \frac{1}{n-1}(X'\mathbf{a})^T(X'\mathbf{a}) = \mathbf{a}^T\Sigma\mathbf{a} \tag{2.55}$$

To make the problem bounded we require the vector $\mathbf{a}$ to be unitary. Hence the problem yields,

$$\max_{\mathbf{a}}(\mathbf{a}^T\Sigma\mathbf{a}), \quad s.t. \;\; \mathbf{a}^T\mathbf{a} = 1 \tag{2.56}$$

The solution to Eq. 2.56 is an eigenvalue problem (EVP),

$$\Sigma\mathbf{a} = \lambda\mathbf{a} \tag{2.57}$$

by definition the covariance matrix Σ is symmetrical and therefore diagonalizable. The k'th EOF is the k'th eigenvector $\mathbf{a}_k$ of Σ. The covariance matrix is also semidefinite, hence all the eigenvalues are positive. The eigenvalue λ_k corresponding to the k'th EOF gives a measure of the explained variance. It is usual to write the explaining variance as a percentage as,

$$\frac{100\lambda_k}{\Sigma_{k=1}^p \lambda_k}\% \tag{2.58}$$

The projection of the anomaly field X' onto the k'th EOF $\mathbf{a}_k$, i.e. $\mathbf{c} = X'\mathbf{a}_k$ is the k'th principal component (PC)

$$c_k(t) = \sum_{k=1}^{p} x'(t,s)a_k(s) \tag{2.59}$$

Because Σ is diagonalizable the set of its eigenvectors forms an orthogonal basis of the p-dimensional Euclidean space, defined with the natural scalar product. So by construction, the Empirical Orthogonal Functions are orthogonal and the PCs uncorrelated. The orthogonality property provides a complete basis where the time-varying field can be separated as:

$$X'(t,s) = \sum_{k=1}^{p} \tag{2.60}$$

This property constitutes, a strong constraint that puts limits to the physical interpretation of individual EOFs since in general physical patterns tend to be nonorthogonal (*North*, 1984 [70]). By construction EOFs constitute directions of variability with no particular amplitude. Therefore if $\mathbf{1}$ is an EOF, so is $\alpha\mathbf{1}$ for any nonzero α. for convenience they are chosen to be unitary. Also by construction EOFs are stationary structures, i.e. they do not evolve in time. The principal component attached to the corresponding EOF provides the sign and the overall amplitude of the EOFs

as a function of time. This provides a simplified representation of the state of the field.

2.2.3 Cross-Calibrated Multi-Platform wind vector analysis

6-hourly high-resolution (0.25 degree) gridded Cross-Calibrated, Multi-Platform (CCMP) wind vectors, were used in this thesis to obtain ocean surface wind velocity over the Sicily channel. A subgrid from 32-40°N to 9-18°E was taken initially with the L3 CCMP v1 version, available for the time span July 1987 to December 2011 (the only available until 2016). Another subgrid from 35.8-36.8°N to 13.8-15.4°E from the CCMP v2 was taken from the period between August 2013 to January 2015, in order to analyze wind patters in the Malta-Sicily channel.

The CCMP data set combines cross-calibrated satellite microwave winds and instrument observations using a Variational Analysis Method (VAM) to produce high-resolution (0.25 degree) gridded analyses. Satellite wind retrievals derived by Remote Sensing Systems (RSS) from a number of satellite-borne passive and active microwave instruments are used. RSS inter-calibrates radiometers at the brightness temperature level to within 0.2 degree Celsius, applying a refined sea-surface emissivity model and radiative transfer function to derive surface winds. The resulting wind retrievals are highly consistent between microwave radiometer instrument platforms, including SSM/I, SSMIS, AMSR, TMI, WindSat, and GMI. RSS has also developed a geophysical model function for deriving wind speeds and directions from microwave scatterometers, including QuikSCAT and ASCAT. Both radiometer and scatterometer data are validated against ocean moored buoys, which confirm the measurements are in agreement (to within 0.8 m/s) despite the difference in wind measurement and retrieval methodologies. All wind observations are referenced to a height of 10 meters (*Atlas et al.*, 2011 [5]). For a complete description of the dataset see: `http://www.remss.com/measurements/ccmp/` and *Atlas et al.*, 2011 [5].

2.2.4 Drifters

Surface drifters or satellite-tracked surface drifting buoys are Lagrangian devices (i.e, follow the water parcel), which consist of a drogue plus a float at given depth. Their speed is calculated along their track by computing the finite difference of their position over time. Drifter position are given by the Argos system or by GPS positioning system (*Stewart*, 2008 [106]).

Six surface drifters from Istituto Nazionale di Oceanografia e di Geofisica Sperimentale (OGS) in Italy with a drogue of 10m, where deployed in the Malta Sicily channel as part of MedArgo program within the Mediterranean Operational Network for the Global Ocean Observing System (MONGOOS) between 2013 and 2015.

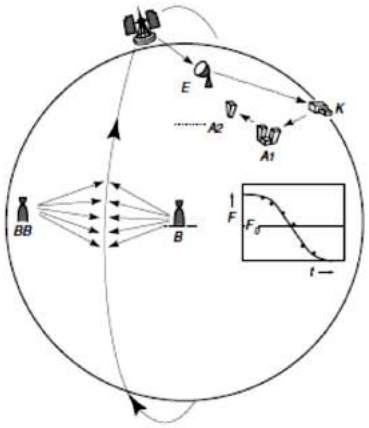

Figure 2.10: System Argos uses radio signals transmitted from surface buoys to determine the position of the buoy. A satellite receives the signal from the buoy B. The time rate of change of the signal, the Doppler shift F, is a function of buoy position and distance from the satellite's track. Note that a buoy at BB would produce the same Doppler shift as the buoy at B. The recorded Doppler signal is transmitted to ground stations E, which relays the information to processing centers A via control stations K. From *Stewart*, 2008 [106].

These instruments provide data to the Copernicus Marine Environment Monitoring Service (CMEMS), were partial support is provided by the Argo-Italy and European Commission projects. For our studies we followed the following drifters: 4877, 4878, 4880 and 4882 for September 2013; 4883 and 4885 for October 2013 and 4903, 4904a, 4905a, 4905b, 4906, 4908b for March 2014. Here the numbers represent the OGS identification number (IdOgs, visit `http://nettuno.ogs.trieste.it/sire/medsvp/drifter_gen.php`). These drifters will be used to validate the measurements made by the HF radars using HFR routines from the HFR group at the Naval Postgraduate School (NPS).

2.2.5 Chlorophyll

Sunlight in the ocean heats the sea water warming up the surface layers, providing the energy required by phytoplankton to grow. Chlorophyll pigments in phytoplankton absorb light and the plants themselves scatter light. This process changes the color of the ocean and then we can use the reflected surface light to map chlorophyll concentration (CHL) from space, which is of primary importance to estimate the ocean productivity. In this thesis, monthly data of chlorophyll concentration (in mg $pigment/\mathrm{m}^3$) in the upper layers of the ocean has been measured by the Moderate Resolution Imaging Spectrometer (MODIS) sensor at the 8-16 ($405 - 877$nm) bands, carried on the Aqua NASA Earth Science satellite mission during August 2012 to December 2013.

The Aqua mission is a part of the NASA-centered international Earth Observing System (EOS) and was formerly named EOS PM, signifying its afternoon equatorial crossing time. Aqua cross the equator daily at 1:30 p.m. as it heads North. The early afternoon observation time contrasts with the Terra satellite which crosses the equator between 10:30 and 10:45 a.m. daily. The two satellites, Aqua's afternoon observations and Terra's morning observations, yield important insights into the "diurnal variability," or the daily cycling of key scientific parameters such as precipitation and ocean circulation. Aqua is the sister satellite to NASA's Terra spacecraft, launched in December of 1999, Aqua's orbit is a sun synchronous, near-polar, with an inclination of 98° to the equator. The total orbit period is approximately 99 minutes and its altitude is about 705km .

On the other hand, the MODIS instrument is part of the sensor package aboard NASA's Aqua satellite. The MODIS instrument employs a conventional imaging-radiometer concept, consisting of a cross-track scan mirror and collecting optics, and a set of linear detector arrays with spectral interference filters located in four focal planes. The optical arrangement of MODIS instrument provides high radiometric sensitivity (12 bit) in 36 spectral bands ranging in wavelength from 0.4 to 14.5μm. Two bands (1-2) are imaged at a nominal resolution of 250 m at nadir[2], with five bands (3-7) at 500 m, and the remaining 29 bands (8-36) at 1 km. A $\pm 55°$ scanning pattern at the EOS orbit of 705 km achieves a 2,330 km swath and provides daylight reflection and day/night emission spectral imaging of any point on the Earth at least every two days [1].

2.2.6 Sea Surface Temperature.

Mapping the sea surface temperature (SST) is important in order to identify upwelling events as well as surface water masses. Water that rises to the surface as a result of upwelling (see section. 2.1.2.2) is typically colder and is rich in nutrients. On the other hand, SST reflects changes in the ocean temperature, then monitoring it become an important fact even for the climate change point of view as well. SST is also linked with surface flows caring the signature of specific water masses as they are transformed by different meteorological and mixing conditions. Monthly SST datasets from January to December 2013 were obtained through the Earth Observation Center database (EOWEB[3]) of the German Aerospace Center (DLR) from the NOAA advanced very high resolution radiometer (AVHRR/3), in the 3B to 5 bands ($3.55 - 12.50\mu$ m), carried on-board of the NOAA19 mission launched in Feb 6, 2009.

[2]direction pointing directly below a particular location.

[3]EOWEB page: `https://centaurus.caf.dlr.de:8443/eoweb-ng/template/default/welcome/entryPage.vm`

NOAA-19, designated NOAA-N' (NOAA-N Prime) is a television infrared observation satellite (TIROS) of NOAA satellites that observe Earth's weather and the environment. NOAA-N Prime carries a suite of instruments that provides critical global data for weather and climate predictions like the AVHRR/3 among others. NOAA-N Prime is a three-axis stabilized spacecraft with an orbital height about 870 ± 19 km in a sun-synchronous circular PM orbit with an inclination angle of 98.73° (retrograde) to the equator. The total orbital period is approximately $102.14 min$. The sunlight period is about $72 min$, and the Earth shadow period about $30 min$. Because the Earth rotates 25.59° during each orbit, the satellite observes a different portion of the Earth's surface during each orbit. The spacecraft cross the equator at about 2 p.m. northbound and 2 a.m. southbound local solar time ([69], [73]).

Additionally, the AVHRR/3 is a six channel cross track scanning imaging radiometer operating in the visible, near infrared (IR), mid IR and far IR wavelength regions with a 1.09 km resolution, which is part of the NOAA-19 satellite mission described above. Those spectral bands ranging in wavelength from $0.58 - 12.50 \mu m$, where channel 1 ($0.58 - 0.68 \mu m$) is typically used for daytime cloud and surface mapping, 2 channel - Land-water boundaries, 3A channel provides the ability to discriminate between clouds and snow and ice, 3B and 4 - night cloud mapping and sea surface temperature and 5 - sea surface temperature ([68]). The scientific purpose of the AVHRR/3 is to examine land surface imagery, cloud imagery, sea surface temperature, ice cover, snow cover extent, vegetation index, land/water boundary, volcanic ash and aerosol concentrations. Channels 1, 2 and 3A characterize radiance whereas Channels 3B, 4 and 5 measure scene brightness temperature in their respective pass bands ([68]).

2.2.7 Complex Correlation and veering estimation.

The average relative displacement or veering between two 2D time series can be obtained from the phase angle of the complex correlation coefficient as described in *Kundu*, 1976 [53]. We will apply this technical in order to compare the datasets previously mentioned (Geostrophic, wind and HFR velocity currents) seeking for Ekman driven phenomena. Let,

$$w(t) = u(t) + iv(t) \tag{2.61}$$

be the complex representation of the velocity time series at time t. The complex correlation coefficient between two vector time series 1 and 2 is defined as their normalized inner product,

$$p = \frac{\langle w_1^*(t) w_2(t) \rangle}{\langle w_1^*(t) w_1(t) \rangle^{\frac{1}{2}} \langle w_2^*(t) w_2(t) \rangle^{\frac{1}{2}}}, \tag{2.62}$$

where the asterisk represents the complex conjugate. p is a complex number whose magnitude gives the overall measure of correlation and whose phase gives the average counterclockwise angle of the second vector with respect to the first. Here the phase is meaningful only in the case the magnitude of the correlation is high.

The instantaneous product $w_1^*(t)w_2(t)$ can be rewritten as, $R(t)\exp(i\alpha(t))$, where $R(t)$ is the product of the instantaneous magnitudes of the velocity vectors and α is the instantaneous veering, so 2.62,

$$p = c\sum_{j=}^{N} R_j \exp(i\alpha_j) \tag{2.63}$$

with,

$$c = \frac{1}{\left[N\left\langle w_1^* w_1\right\rangle^{\frac{1}{2}}\left\langle w_2^* w_2\right\rangle^{\frac{1}{2}}\right]} \tag{2.64}$$

a real constant and j referring to the time t_j. Then the sum of all vectors $R_j\exp(i\alpha_j)$ at times t_j define the phase of the complex correlation coefficient. In terms of the east and west components Eq. 2.61 can be expressed as,

$$p = \frac{\langle u_1u_2 + v_1v_2\rangle}{\left\langle u_1^2+v_1^2\right\rangle^{\frac{1}{2}}\left\langle u_2^2+v_2^2\right\rangle^{\frac{1}{2}}} + i\frac{\langle u_1v_2 - u_2v_1\rangle}{\left\langle u_1^2+v_1^2\right\rangle^{\frac{1}{2}}\left\langle u_2^2+v_2^2\right\rangle^{\frac{1}{2}}}, \tag{2.65}$$

where the phase angle or average veering is,

$$\alpha_{av} = \tan^{-1}\frac{\langle u_1v_2 - v_1u_2\rangle}{\langle u_1u_2 + v_1v_2\rangle}. \tag{2.66}$$

2.2.8 Kinematic properties of an eddy.

We applied the method described by Sanderson, 1995 [99] in order to describe and examine the structure of the mesoscale detected in the Malta-Sicily channel using the lstranslate routine. The lstranslate routine was developed by the HFR radar group at the Naval Postgraduate School and resumes Sanderson's method. Assuming that there is an eddy with spatially uniform velocity gradients, which are independent of time.

$$g_{11} = \frac{\partial u}{\partial x} \tag{2.67a}$$
$$g_{12} = \frac{\partial u}{\partial y} \tag{2.67b}$$
$$g_{21} = \frac{\partial v}{\partial x} \tag{2.67c}$$
$$g_{22} = \frac{\partial v}{\partial y} \tag{2.67d}$$

From Eq. 2.67, divergence is defined as $d = g_{11} + g_{22}$, stretching deformation a $= g_{11} - g_{22}$, vorticity c $= g_{21} - g_{g12}$ and the shearing deformation $b = g_{21} + g_{g12}$ are functions of the velocity gradients. The method assumes that the center of the eddy is located at X,Y and moves with constant velocity (U, V), whereas at some distance from the center of the eddy the flow velocity has an added component due to the velocity gradients. X_0, Y_0 is defined as the initial position of the eddy. Then the flow center position can be written as,

$$X = X_0 + U(t) \tag{2.68a}$$
$$Y = Y_0 + V(t) \tag{2.68b}$$

so then the velocity $u_i(t_k), v_i(t_k)$ of the ith particle at time t_k is,

$$u_i(t_k) = U + g_{11}\left[x_i(t_k) - X_0 - Ut_k\right] + g_{12}\left[y_i(t_k) - Y_0 - Vt_k\right] + u_i^{'}(t_k) \tag{2.69a}$$
$$v_i(t_k) = V + g_{21}\left[x_i(t_k) - X_0 - Ut_k\right] + g_{22}\left[y_i(t_k) - Y_0 - Vt_k\right] + v_i^{'}(t_k) \tag{2.69b}$$

$x_i(t_k), y_i(t_k)$ is the position of the ith particle at time t_k and $u_i'(t_k), v_i(t_k)'$ is the residual velocity. These equations (Eq. 2.69) can be rewritten as a linear polynomial as follows,

$$u_i(t_k) = \alpha + \alpha_1 t_k + g_{11}x_i(t_k) + g_{12}y_i(t_k) + u_i'(t_k) \tag{2.70a}$$
$$v_i(t_k) = \beta + \beta_1 t_k + g_{21}x_i(t_k) + g_{22}y_i(t_k) + v_i'(t_k) \tag{2.70b}$$

where,

$$\alpha = U - g_{11}X_0 - g_{12}Y_0 \tag{2.71a}$$
$$\beta = V - g_{21}X_0 - g_{22}Y_0 \tag{2.71b}$$
$$\alpha_1 = -g_{11}U - g_{12}V \tag{2.71c}$$
$$\beta_1 = -g_{21}U - g_{22}V \tag{2.71d}$$

these equations can be written in matrix form,

$$A + PG + R \tag{2.72}$$

where,

$$A = \begin{pmatrix} u_1(t_1) & v_1(t_1) \\ \vdots & \vdots \\ u_n(t_1) & v_n(t_1) \\ \vdots & \vdots \\ \vdots & \vdots \\ u_1(t_m) & v_1(t_m) \\ \vdots & \vdots \\ u_n(t_m) & v_n(t_m) \end{pmatrix} P = \begin{pmatrix} 1 & t_1 & x_1(t_1) & y_1(t_1) \\ \vdots & \vdots & \vdots & \vdots \\ 1 & t_1 & x_n(t_1) & y_n(t_1) \\ \vdots & \vdots & \vdots & \vdots \\ \vdots & \vdots & \vdots & \vdots \\ 1 & t_m & x_1(t_m) & y_1(t_m) \\ \vdots & \vdots & \vdots & \vdots \\ 1 & t_m & x_n(t_m) & y_n(t_m) \end{pmatrix} \tag{2.73a}$$

(2.73b)

$$G = \begin{pmatrix} \alpha & \beta \\ \alpha_1 & \beta_1 \\ g_{11} & g_{21} \\ g_{12} & g_{22} \end{pmatrix} R = \begin{pmatrix} u_1'(t_1) & v_1'(t_1) \\ \vdots & \vdots \\ u_n'(t_1) & v_n'(t_1) \\ \vdots & \vdots \\ \vdots & \vdots \\ u_1'(t_m) & v_1'(t_m) \\ \vdots & \vdots \\ u_n'(t_m) & v_n'(t_m) \end{pmatrix} \tag{2.73c}$$

2

Standard linear regression lead to the solution,

$$G = [P^T P]^{-1} P^T A \tag{2.74}$$

where the residual velocities are,

$$R = [1 - P(P^T P)^{-1} P^T] A \tag{2.75}$$

Solving Eq. 2.71 for $U,\ V,\ X_0,\ Y_0$ yields,

$$U = \frac{g_{22}\alpha_1 - g_{12}\beta_1}{g_{12}g_{21} - g_{11}g_{22}} \tag{2.76a}$$

$$V = \frac{g_{11}\beta_1 - g_{21}\alpha_1}{g_{12}g_{21} - g_{11}g_{22}} \tag{2.76b}$$

$$X_0 = \frac{g_{22}(\alpha - U) - g_{12}(\beta - V)}{g_{12}g_{21} - g_{11}g_{22}} \tag{2.76c}$$

$$Y_0 = \frac{g_{11}(\beta - V) - g_{21}(\alpha - U)}{g_{12}g_{21} - g_{11}g_{22}} \tag{2.76d}$$

For our studies we will focus on the vorticity applied to the Malta Sicily channel since our aim is to individuate the mesoscales features associated with this specific area.

3 Results and Discussion

In this chapter, we show the results obtained during the development of this thesis. First section, describes the surface circulation and water masses evolution in the Sicily Channel using daily maps of absolute dynamic topography (MADT) from AVISO+ datasets (see section. 2.2.2) along with wind fields from the Cross-Calibrated Multi-Platform wind vector analysis (CCMP, see section. 2.2.3) in order to get a broad picture of the studied area. Section 2, introduces the Malta-Sicily channel and its surface circulation structures analyzed using an array of CODAR high frequency radars as part of the CALYPSO project (see section. 2.2.1). In section 3, sea surface temperature and sea surface chlorophyll in the Malta-Sicily channel alongside with drifter trajectories were analyzed. This is in order to validate the HFR observations and the influence of the surface currents in the distribution of certain properties, such as CHL and SST, which are important from the economic, ecological, biological and physical point of view. Section 4, discusses ADCP datasets from an oceanographic campaign in the Malta-Sicily channel carried out in October 2013. These data were analyzed using Ekman theory with the aim of getting an insight of how the the water column behaves in this area.

3.1 The Sicily channel

3.1.1 Mean surface circulation

The Sicily channel is a complex bathymetric system that exchanges water masses and other physical, biological and chemical properties with the two major basins in the Mediterranean; the western and eastern Mediterranean basins (WMED and EMED respectively). On the WMED, the Sicily strait is the major obstacle for the Atlantic water (AW) entering into the channel. This area is characterized by a two sill system as previously mentioned (see *Rovere and Wurtz*, 2015 [96]). On the other side, the exit towards the Ionian sea is delimited by the Malta plateau and the Medina Bank (Figure 1.3). The middle of channel is also composed for three important depressions, the Pantelleria graben ($\sim$ 1300 m depth), Linosa graben ($\sim$ 1500 m depth) and the Malta graben ($\sim$ 1700 m depth). These bathymetric complexities render the Sicily channel to be a high energy site with a dynamic and highly variable current system.

In a simpler way, the circulation in the Sicily channel can be characterized as a two-layer system. In the upper layer ($\sim$ 200 m thick), Atlantic water (AW) flows eastward from the Gibraltar strait through the SC towards the inner parts of the EMED. Levantine intermediate water (LIW) on the other hand, flows westwards as the deepest layer of incoming water entering the channel from the Ionian sea towards the WMED. Other studies like *Ismail et al.*, 2012 [46] and 2014 [47], suggested a more complex layering of the channel. For instance some transitional layers between the Levantine water and the Atlantic water have been identified. Since we are focusing on the surface circulation, we will not enter into details about the water column behavior.

Daily maps of absolute dynamic topography (MADT) from merged satellite missions Ssalto/Duacs, contain gridded L4 sea surface heights above the geoid with a spatial resolution of 0.125 degree $\times$ 0.125 degree (see 2.2.2). This data accounts for the time span starting from January 1993 to December 2015. We worked those data on the area comprising 10 to 16 °E longitude and 33 to 38 °N latitude. A 23 year filtered time series of sea surface height above the geoid, spatially averaged over the Sicily Channel is shown in fig 3.1. In order to see the long term MADT variability in the Sicily channel, the time series was fitted to a 4th degree polynomial which shows an oscillatory behavior. This might be related with the Adriatic-Ionian Bimodal Oscillatory System (BiOS) described by *Gacic et al.*, 2010, 2011 [33], [34] and *Civitarese et al.*, 2010 [21].

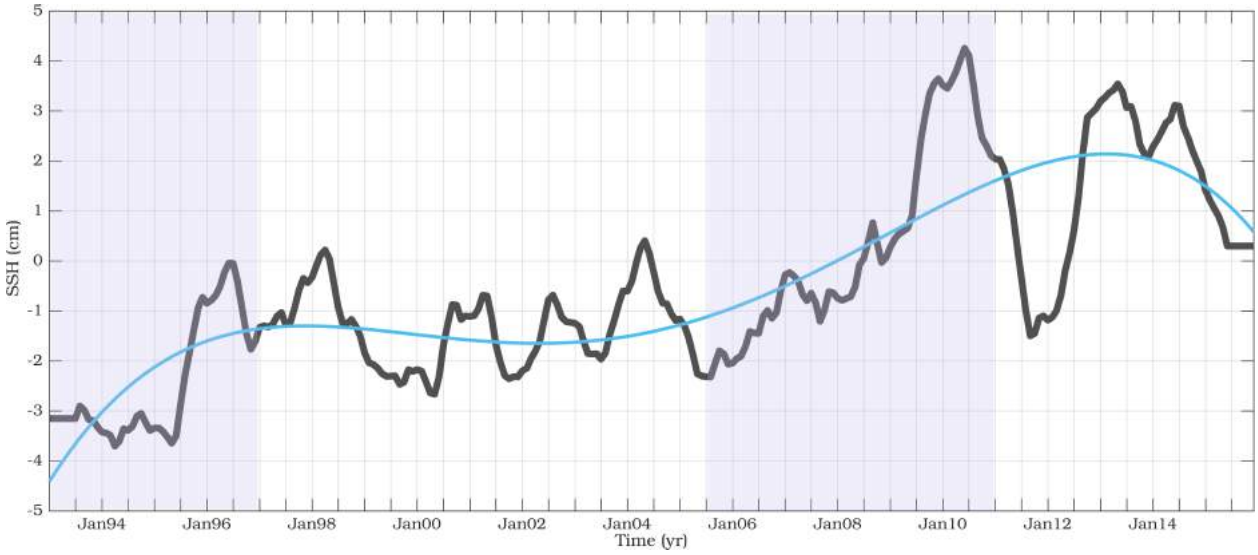

Figure 3.1: Filtered absolute dynamic topography (MADT) time series spatially averaged over the Sicilian channel (10-16 °E and 33-38 °N). The blue line represents the 4th polynomial fit which shows the pseudo-oscillatory behavior of the time series. The latest being associated with the BiOS mechanism.

The BiOS is a pseudo-periodic mechanism ($\sim$ 10 years), that reverses the circulation in the Ionian sea from cyclonic to anticyclonic (Figure. 3.2) in the North-Ionian Sea. Gacic et al., 2010 states that in the anticyclonic phase, the BiOS allows Atlantic water to flow into the Adriatic basin making it fresher in terms of salinity concentration. Subsequently, this processes dilutes the Adriatic deep water (ADW), which in turn deepens and spreads into the Ionian at the Otranto strait. The corresponding sea level increases gradually weakening the anticyclone upper circulation and inverting the surface pressure gradient, enhancing the cyclonic phase [*Civitarese et al.*, 2010 [21]; *Gacic et al.*, 2010 [33]]. The cyclonic phase on the other hand, allows the inflow of more saline water masses such that Levantine or Cretan waters into the Adriatic basin. This process increases the salinity of the Adriatic sea, lowering the sea level and reversing the surface pressure gradient restoring the anticyclonic circulation. The impact of this mechanism over the Sicily channel is synthesized in *Gacic et al.*, 2013 [35] where events of low (high)-salinity were associated with the anticyclonic (cyclonic) phase of the BiOS.

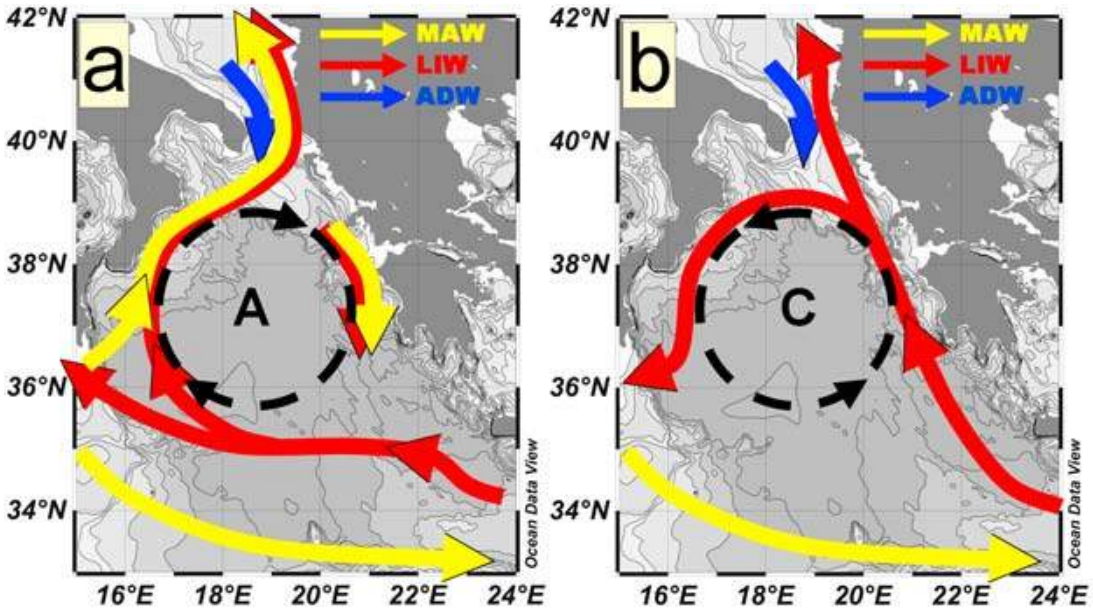

Figure 3.2: Schematic representation of the AdriaticIonian bimodal oscillating system: (a) anticyclonic mode and (b) cyclonic mode [taken from *Gacic et al.*, 2010 [33]].

The mechanism blocks the Atlantic Ionian Stream circulation coming from the Sicily Channel towards the North-Ionian Sea. In its *cyclonic phase* (1998-2005 and 2011-2016 *Bessieres et al.*, 2013 [8]), BiOS helps with the developing of the *mid Ionian jet*. On the other hand, during the *anticyclonic phase* (1993-1997 and 2006-2010, *Bessieres et al.*, 2013 [8]) the AIS flows towards the Otranto Strait leaving the Sicily channel and transporting Atlantic water towards the Adriatic as described

previously. Since our interest in this section is toward the Sicily Channel, we will not get much into details about what happens after the AIS leaves the channel.

Figure. 3.3 represents the Sicily Channel mean geostrophic circulation derived from MADT, averaged over the time period studied (1993-2015). Here we highlight the two major circulation structures in the Malta Sicily Channel (MSC): The anti-cyclonic Malta Sicily Gyre (MSG) and the Atlantic Ionian Stream (AIS), as well as some other predominant structures. Here the AIS has been the most studied structure among all (see *Robinson et al.*, 1999 [95]). Figure. 3.3 shows a dipole like sea level shape, with positive to negative at the Sicilian Strait. As we mentioned before, the Sicily channel is subdivided longitudinally into two sills. Here, the Italian side of the channel is narrower with a maximum depth of 430 m. In this part of the channel the sea level is lower than in the Tunisian side (which is shallower and bathymetrically wider).

Pascual et al., 2014 stated that due to baroclinic instabilities, the Atlantic current (AC) regularly forms meanders that can be eventually detached from the current and become both cyclonic and anticyclonic coastal eddies like the ones observed by *Iudicone et al.*, 1998 [48], *Larnicol et al.*, 2002 [55], *Olita et al.*, 2011 [76] and *Puillat et al.*, 2002 [88]. For example, the Adventure Bank Vortex ABV, derived from the geostrophic approximation is in our case located at 37.5°N 11.5°E and is anticyclonic in disagreement with *Robinson et al.*, 1999 [95], *Lermusiaux and Robinson*, 2001 [58] and *Jouini et al.*, 2016 [52]. In their case, the gyre is located at 37°N 12.5°E and is cyclonic instead. On the other hand, The anticyclonic Malta Sicily Gyre (MSG), the cyclonic Malta Gyre (MG) and Mesina Rise Vortex (MRV) are seasonal semi permanent structures. After passing by the MSC, the AIS, which is mainly composed by Modified Atlantic Water, exits and bifurcates into the Ionian sea which has a depth of $\sim$ 3000 m. One of the branches flows towards the North Ionian Sea and the other towards the mid Ionian. This because both signals from the anticyclonic and the Cyclonic BiOS are present. Besides the MSG, we also highlight the presence of the cyclonic Mesina Rise Vortex (MRV) close to the eastern Sicilian coast as well as the Malta gyre (MG) and the Libyan Shelf Break Vortex (LSBV) as described in *Jouini et al.*, 2016 [52] and *Jebri et al.*, 2016 [49] and 2017 [50].

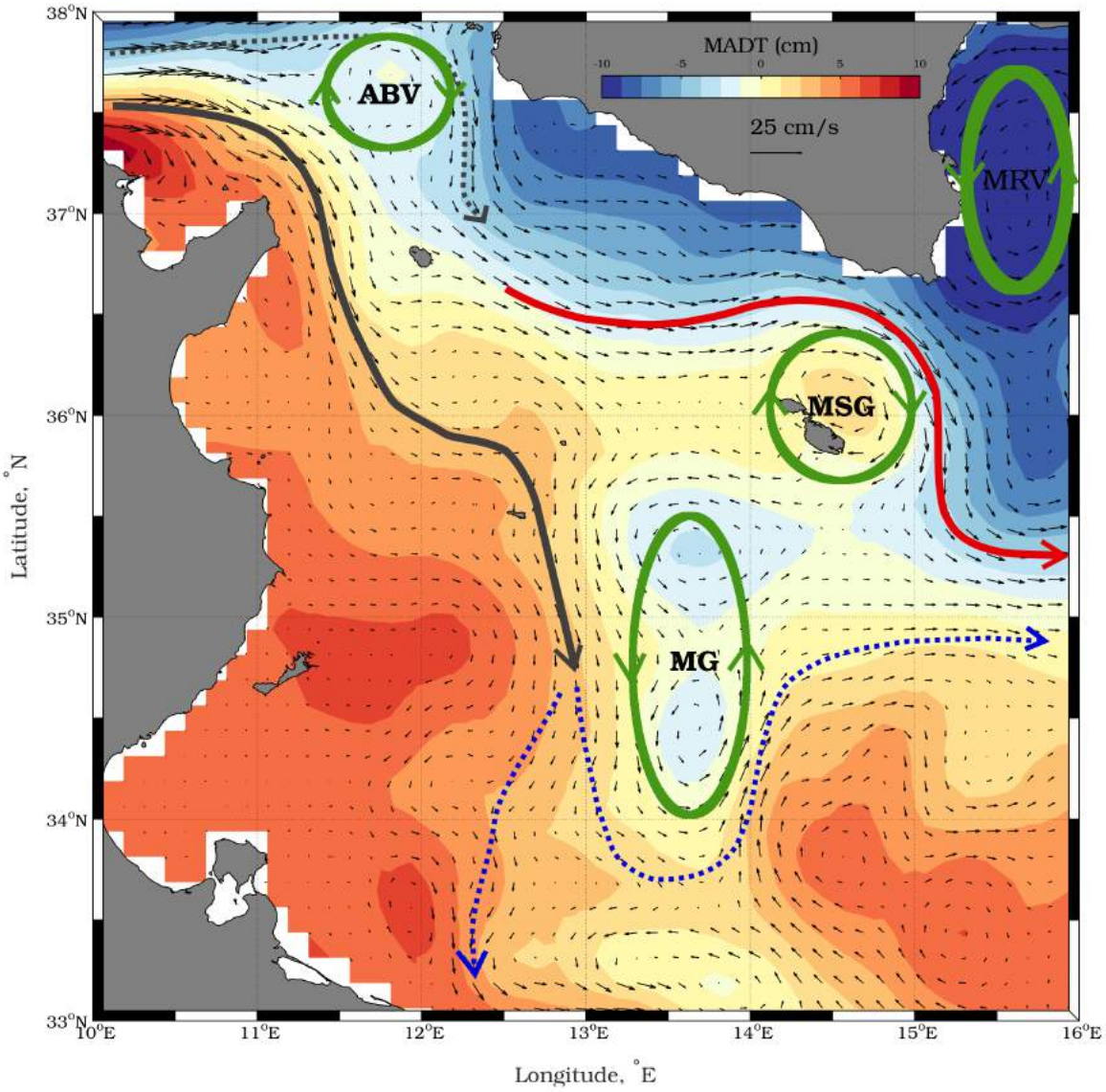

Figure 3.3: Interannual map of Mediterranean absolute dynamic topography and mean geostrophic circulation in the Sicilian channel. Permanent structures in black, summer in red, winter in blue and semipermanent structures in dashed lines. The most predominant gyres are highlighted in green.

For interpretation we adopt a seasonal approach: Winter, DJF (December, January, February); spring, MAM (March, April, May); summer, JJA (June, July, August) and Autumn, SON (September, October, November). MADT data was averaged over the time span covering January 1993 to December 2015 on each season. Figure. 3.4 shows winter mean geostrophic circulation. The Algerian current (AC) which is composed by Atlantic water, bifurcates at the opening of the strait in two branches: the Bifurcation Atlantic/Algerian current (BAC), that flows toward the northern tip of Sicily and the Atlantic Tunisian Current (ATC) that enters into the

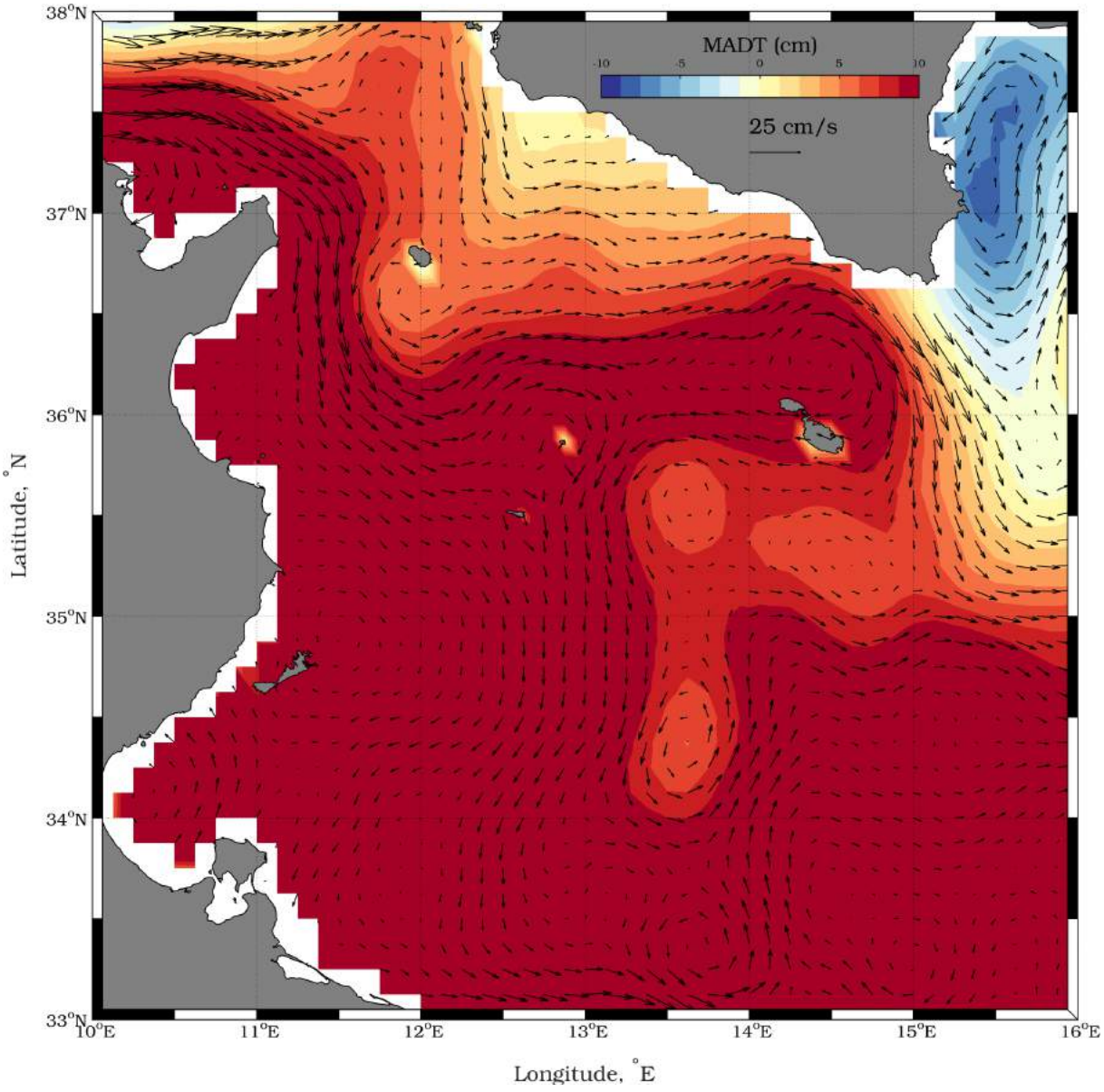

Figure 3.4: Interannual Winter map of Mediterranean absolute dynamic topography and mean geostrophic circulation in the Sicilian channel.

Sicilian channel. For the winter period we also spot a new structure of about 50 km radius at 14.5°E 36.1°N. This structure is recurrent in the Malta Sicily channel (MSC) for this period. We will reefer to it as the Malta-Sicily Gyre (MSG).

This gyre appears in winter-spring time overall, driving the circulation in the area while the AIS is not strong enough to maintain the circulation. This might be a result of conservation of potential vorticity as described by *Lermusiaux and Robinson*, 2001 [58] and *Drago et al.*, 2003 [28]. For example, the bathymetry in the Malta Sicily channel abruptly changes from a depth of $\sim$ 700 m (Malta graben) to shallow $\sim$ 100

m in the MSC (see Figure. 1.3). Here the gyre velocity oscillates between 5-10 cm/s as seen in Figure. 3.4.

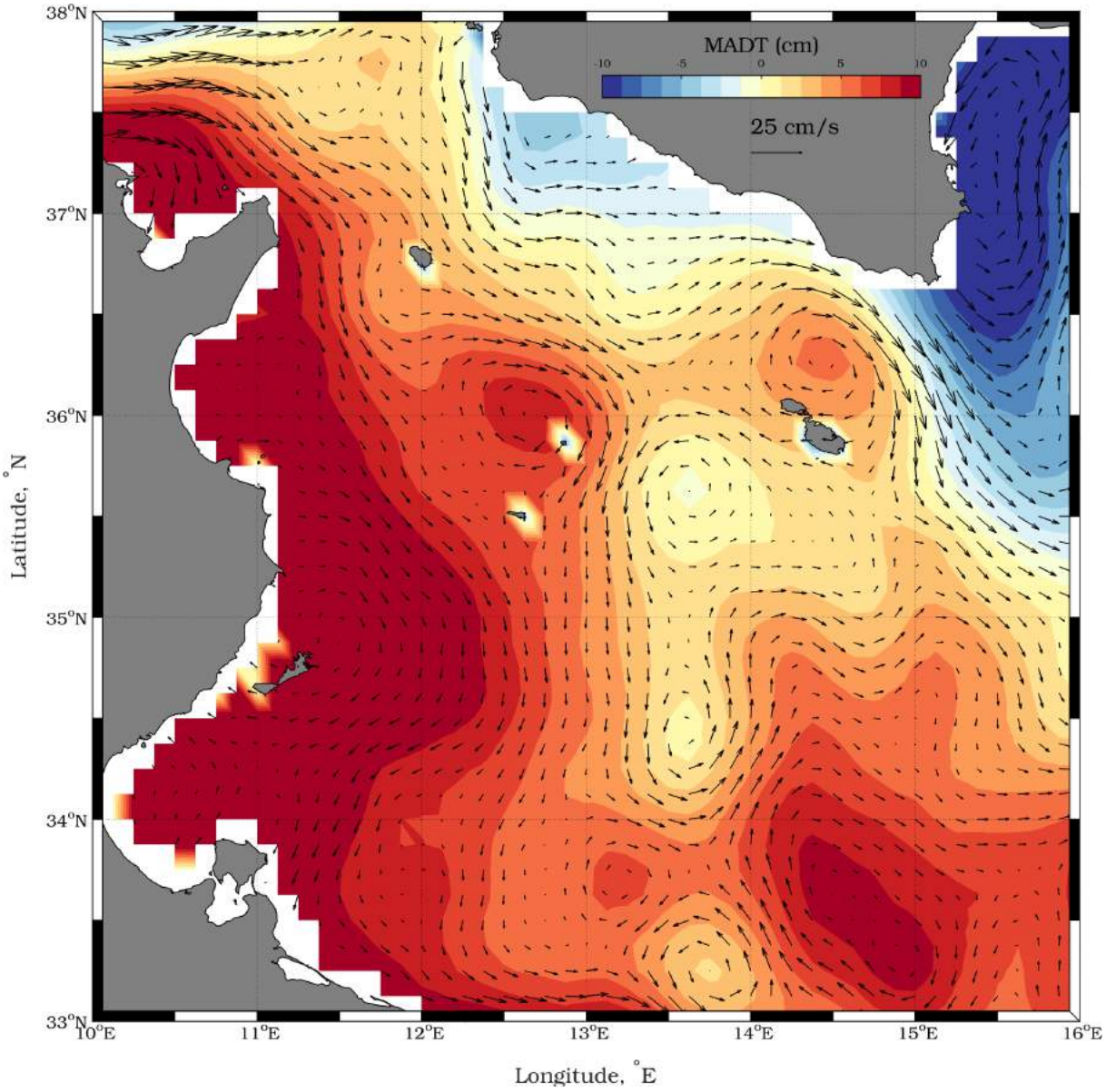

Figure 3.5: Interannual Spring map of Mediterranean absolute dynamic topography and mean geostrophic circulation in the Sicilian channel.

Figure. 3.5 represents the mean in Spring. We were able to identify some of the winter patterns in *Jouini et al.*, 2016 [52] for instance the ATC which in turns bifurcates at about 35°N into the Atlantic Libyan Current (ALC) and the Bifurcation Atlantic Tunisian Current (BATC). The BATC flows towards Sicily creating two vortexes, the cyclonic MG and one anticyclonic probably due to the influence of the Linosa graben at 36°N. Also in this period we can see the recurrence of the

anticyclonic Malta Sicily gyre (MSG) at the MSC, as well as the LSBV (Libyan Shelf Break Vortex) close to the Libyan coast. Again we see the split of the AW current at the exit of the Malta Sicily channel flowing towards the mid and northern Ionian Sea. Besides this, in the northern tip of Sicily, there is a recirculation of the AW that enters into the Sicilian channel reinforcing the Malta Sicily gyre. This period is a mixing state between the AIS that starts forming in the northern tip of Sicily and the Malta Sicily gyre. Also, neither in DJF or MAM we were able to observe the cyclonic Pantelleria vortex (PV) presented in *Lermusiaux and Robinson*, 2001 [58] and *Jouini et al.*, 2016 [52] as a winter structure.

Figure. 3.5 represents the mean in Spring. We were able to identify some of the winter patterns in *Jouini et al.*, 2016 [52] for instance the ATC which in turns bifurcates at about 35°N into the Atlantic Libyan Current (ALC) and the Bifurcation Atlantic Tunisian Current (BATC). The BATC flows towards Sicily creating two vortexes, the cyclonic MG and one anticyclonic probably due to the influence of the Linosa graben at 36°N. Also in this period we can see the recurrence of the anticyclonic Malta Sicily gyre (MSG) at the MSC, as well as the LSBV close to the Libyan coast. Again we see the split of the AW current at the exit of the Malta Sicily channel flowing towards the mid and northern Ionian Sea. Besides this, in the northern tip of Sicily, there is a recirculation of the AW that enters into the Sicilian channel reinforcing the Malta Sicily gyre. This period is a mixing state between the AIS that starts forming in the northern tip of Sicily and the Malta Sicily gyre. Also, neither in DJF or MAM we were able to observe the cyclonic Pantelleria vortex (PV) presented in *Lermusiaux and Robinson*, 2001 [58] and *Jouini et al.*, 2016 [52] as a winter structure.

For the summer period June-July-August, we were able to observe the big influence of the Atlantic Ionian Stream (AIS) over the channel. The AIS as we can see in Figure. 3.6 is a very strong current that behaves like a jet stream in the Sicilian strait. It is characterized by a velocity of about 25 cm/s but it can reach higher values. This current is mainly composed by Atlantic water (AW) which slightly changes properties as it passes by the strait as previously mentioned. Then it deepens into the Ionian bifurcating either towards the North or to the Mid Ionian sea depending on the BiOS phase (*Gacic et al.*, 2010 [33] and 2013 [35], *Bessieres et al.*, 2013 [8] and *Jebri et al.*, 2017 [50]). On the other hand, we observed some mesoscales like the anticyclonic Maltese Channel Crest (MCC) and the cyclonic Mesina Rise Vortex (MRV) as well as the some other mesoscales towards the Libyan side probably being associated with the LSBV. We also point out that the cyclonic Adventure Bank Vortex (ABV) and the Ionian Shelf Break Vortex (ISV) were not found on the seasonal decomposition nor in the interannual geostrophic circulation (both of the mesoscales being associated as summer structures in *Robinson et al.*, 1999 [95], *Lermusiaux and Robinson*, 2001 [58] and *Jouini et al.*, 2016 [52]). Although over the monthly means we were able to see

them, they seem to be temporary and appear just in some years. Still the reason why they are triggered is yet under study.

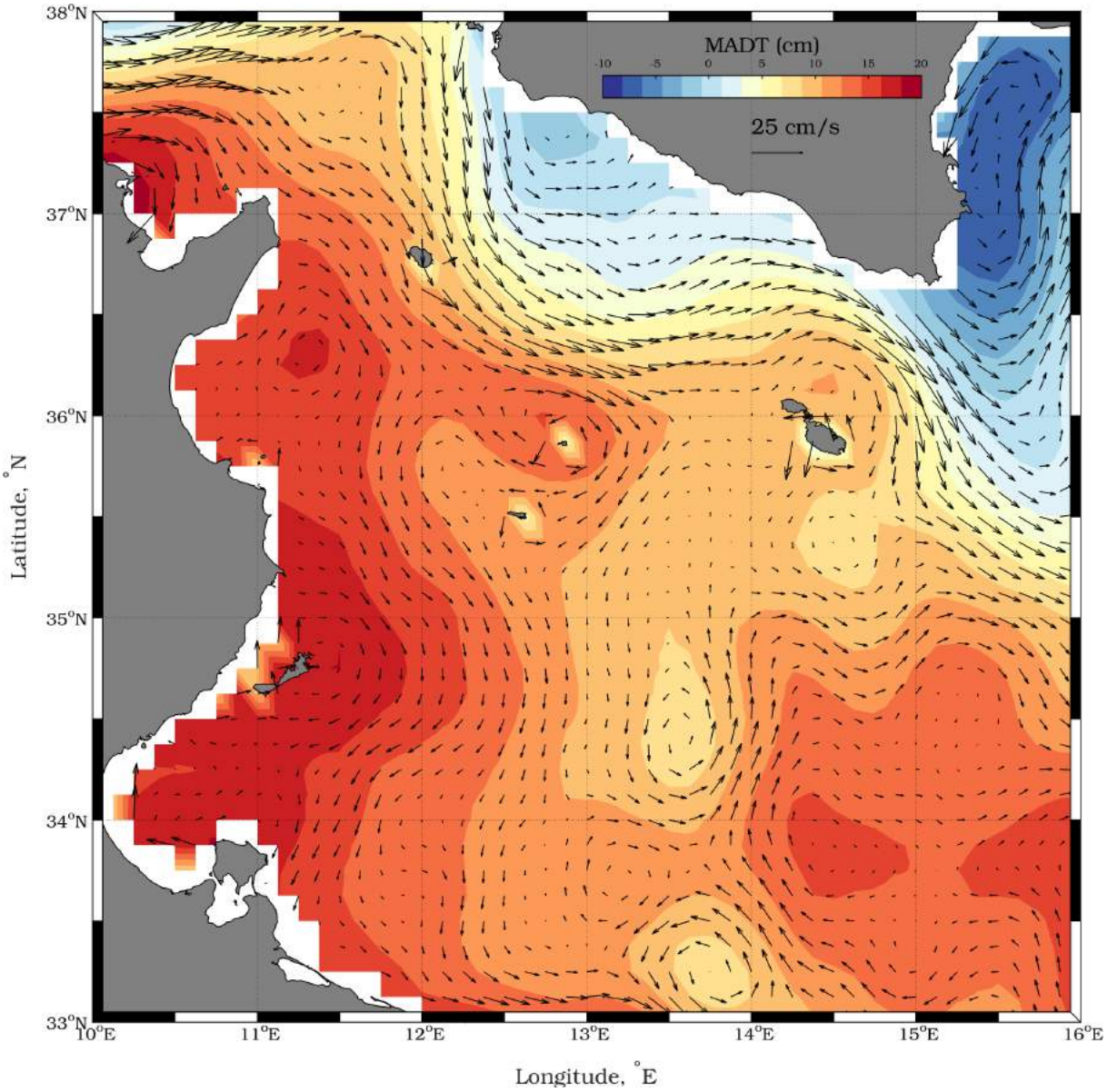

Figure 3.6: Interannual Summer map of Mediterranean absolute dynamic topography and mean geostrophic circulation in the Sicilian channel.

Figure. 3.7 shows SON (September, October, November) mean geostrophic circulation, which is still being driven by the AIS and reinforced by AW coming from the BAC and the ATC. The Algerian Current (AC) and the ATC bifurcate at the Sicilian strait and then meet again close to the pelagie islands. We can also observe some other mesoscale structures like the cyclonic MRV, a weaker anticyclonic MCC and the

triggering of the anticyclonic MSG. This weakening probably since these mesoscales may have shorter life times and are not well represented by the total mean.

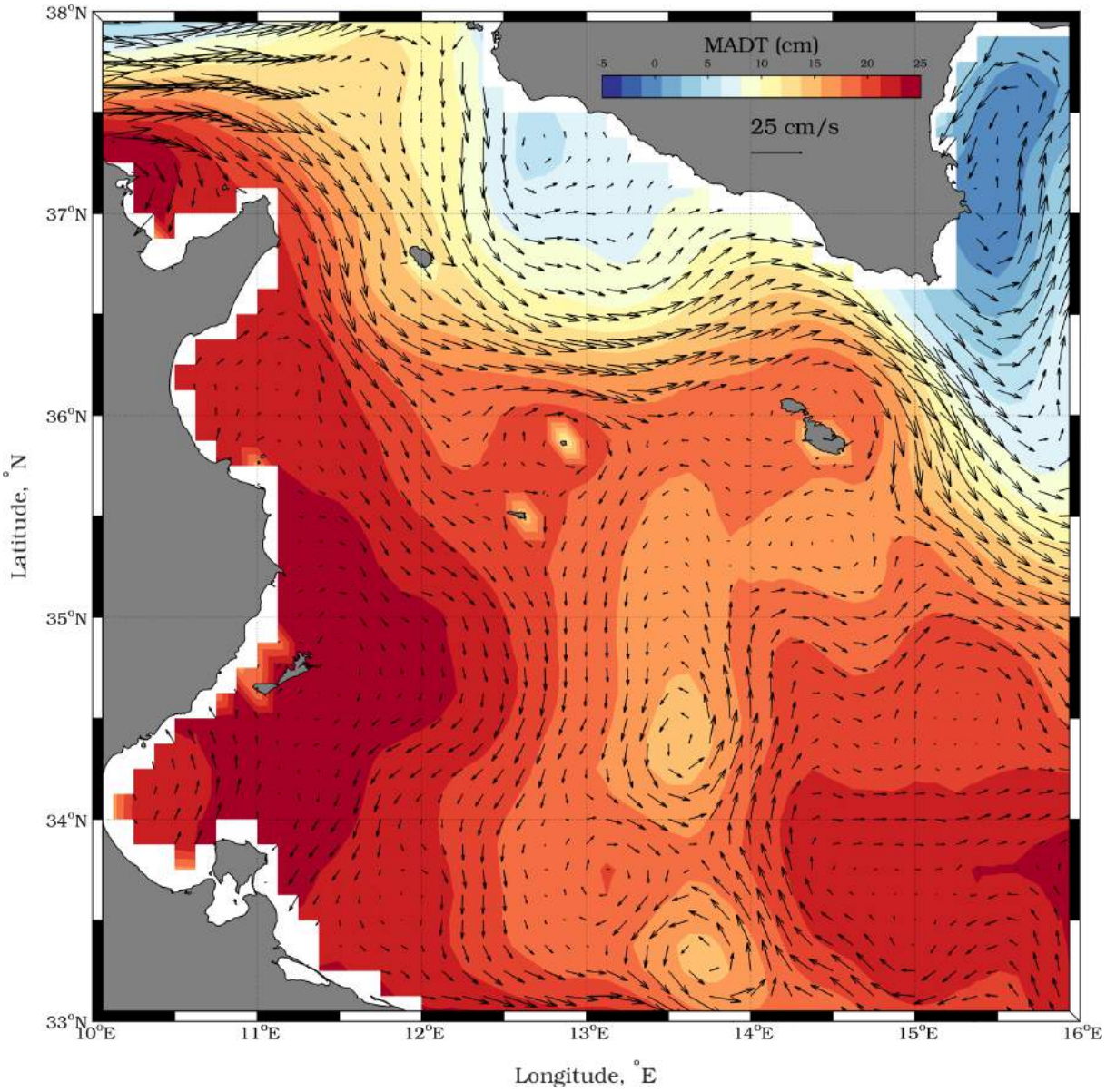

Figure 3.7: Interannual Autumn map of Mediterranean absolute dynamic topography and mean geostrophic circulation in the Sicilian channel.

Annual and monthly geostrophic currents show a strong signal of the Algerian Current, the Atlantic Tunisian Current and the Atlantic Ionian Stream. For some years the AIS is triggered by the ATC instead of the BAC instead of just being a phenomena occurring due to the action of the BAC as described by *Robinson et al.*, 1999 [95]. From 2011 to 2015 the ATC is stronger (except for 2013), flowing through the center of the Sicily channel and making the AIS weaker. On the other hand

for most of the data available, there is a notorious and strong AIS signal. We also observed the influence of the BiOS, which from the time span 1993-1997 (anticyclonic phase) allows the Atlantic water to flow towards the North Ionian Sea. Then in its cyclonic phase the BiOS, blocks the AIS due to the presence of the cyclonic North Ionian Gyre (NIG) making the AIS to head towards the Ionian Sea as the mid-Ionian jet (1998-2006). For the period 2007 until 2015, the AIS path is not yet clear and a bit confusing. Even thought we would expect an anticyclonic phase of the BiOS and subsequently AW going towards the North Ionian, what happens is the opposite. For this period the cyclonic Mesina Rise Vortex (MRV) has stretched blocking the pathway of the AIS.

3.1.2 Eddy Kinetic Energy (EKE).

Here we use the MADT anomalies, removing the temporal mean at each grid point of the dataset. We calculated the geostrophic EKE in order to measure and identify regions of highly variable phenomena. Figure 3.8 shows the mean geostrophic EKE calculated from the MADT anomalies and averaged over the time span studied. As expected, most of the variability is located at the Malta Sicily Channel and at the Sicily strait. At the Sicilian Strait (between 37° and 38°N) we can notice high EKE values $\sim$300 cm^2/s^2. Here most of the Atlantic water is trapped an deviated into the channel channel. This creates a tongue of Atlantic water which can be seen from 37.5 to about 36°N. This signature of $\sim$180 cm^2/s^2 is associated with the Atlantic Tunisian Current, ATC. On the other hand, a branch of the Bifurcation Algerian Current BAC (between 100 and 150 cm^2/s^2) is also highlighted and being weaker than the ATC signature close to the northern tip of Sicily. Another highly variable area is the MSC, as expected due to the recurrent action of the Atlantic Ionian Stream. Here we have again high EKE values (300 cm^2/s^2) close to the Sicilian coast. In contrast the southwestern side of the channel has values lower than 50 cm^2/s^2 where more calm and shallow areas can be found. Signals of $\sim$120 cm^2/s^2 can be seen at 35°N 13°E and 35.5°N 13°E representing the MCC and MG. A broader EKE study of the Mediterranean sea can be found in *Pujol and Larnicol*, 2005 [90], where a 11 year altimetry dataset was used to describe the Eddy kinetic variability in the Mediterranean sea.

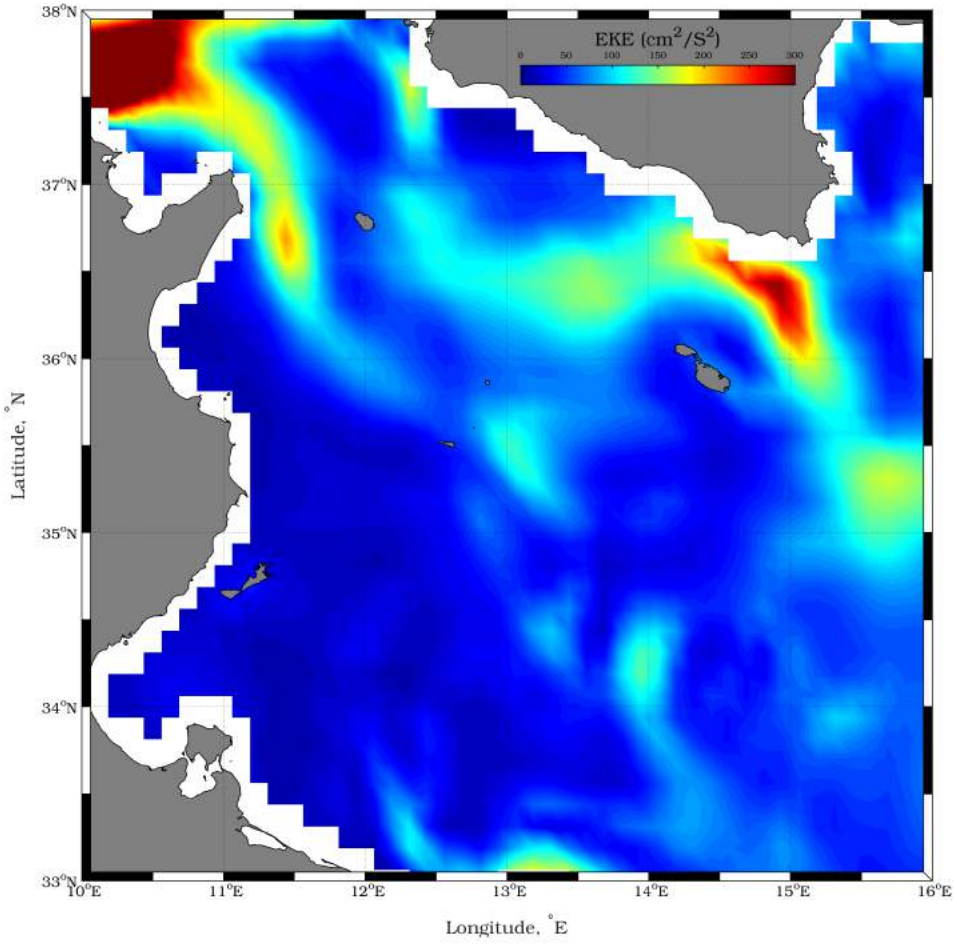

Figure 3.8: Sicily channel mean geostrophic eddy kinetic energy (EKE) derived from MADT Aviso datasets over the time span 1993-2015. Colorbar represents eddy kinetic energy in cm^2/s^2

3.1.3 Empirical Orthogonal Functions (EOF)

We employ Empirical Orthogonal Functions (EOF) or principal component analysis (PCA) in our MADT time series in order to extract the leading lagged modes of MADT variance over the Sicily channel in order to determine its spatial and temporal variations. We normalize the EOF maps to unit variance so our PCs time series have units of cm (*Vigo et al.*, 2005 [111]. Here we filtered our data with a low-pass 13 month moving average filter with the aim of smoothing the data to form a trend following indicator, in this case removing the seasonal signatures (*Thomson and Emery*, 2014 [108]). Each EOF represents a mode of Variability i,e. and oscillation, and the expansion coefficients of the mode i.e, the PC, show how the each mode oscillates in time *Björnsson and Venegas*, 1997 [14]].

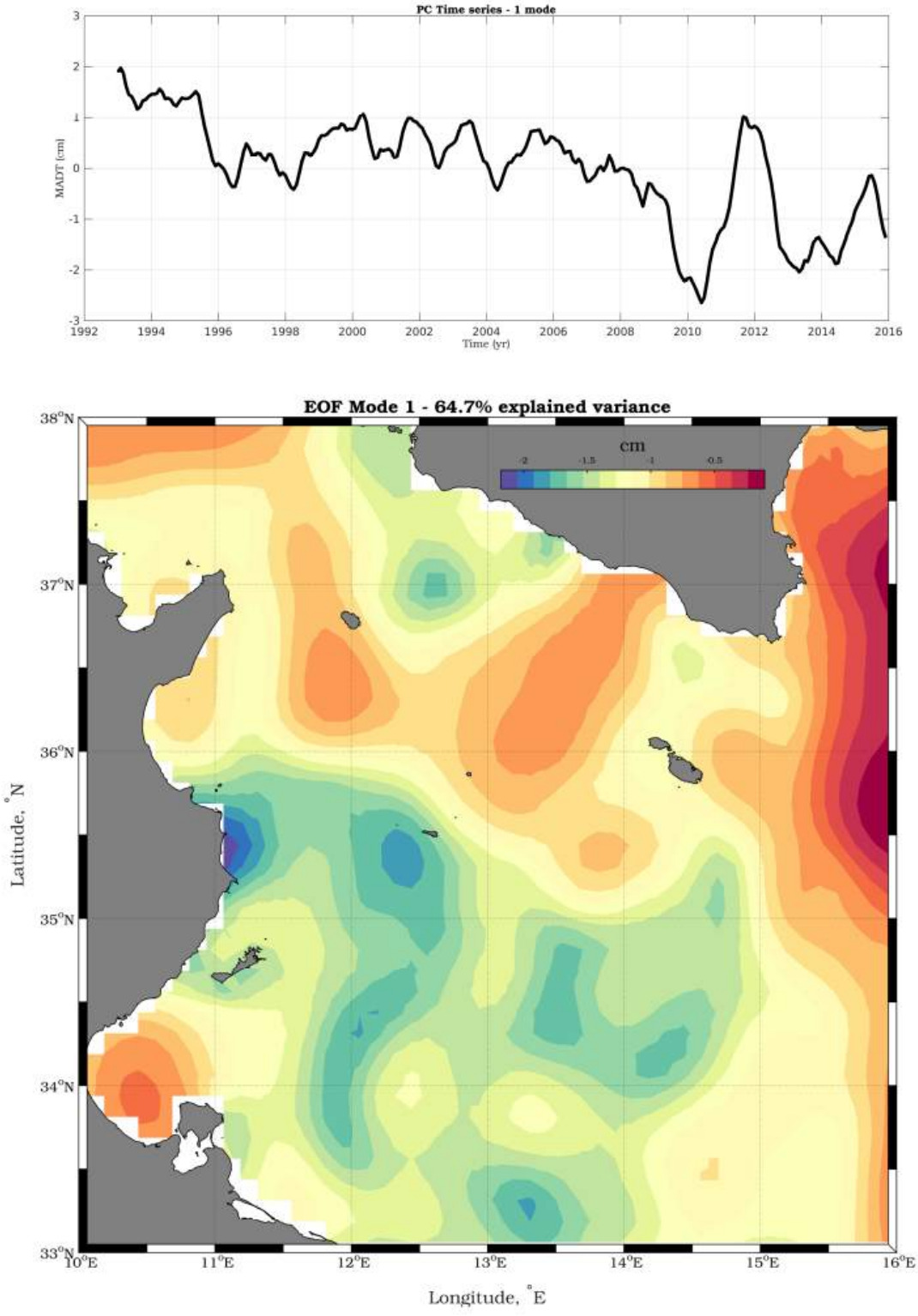

Figure 3.9: First EOF/PC mode of SSH in the Sicilian channel, dataset spanning from January 1993 to December 2015.

Figure 3.9 represents the first EOF/PC mode and explains the 64.7% variance of the original time series. The upper panel show the PC time series and the lower one, the EOF. The first eigenvector (EOF1) shows positive values in the north part of the channel, while the south is mostly negative. Most of the Positive part, oscillates around the deep canyons in the SC. It is also possible to see the most of the AIS pathway. Starting at 38°N and going towards the Sicilian coast. Then again at the Malta Escarpment we can see most of the variability. Then the places where we see most of the change in variance are where the bathymetry is more complex (like the Linosa graben, Malta graben and Pantelleria graben). The corresponding PC is periodic with a period of about 12 months, showing an annual cycle. The time series also shows a change on the trend around 2009. Here there is a decrease in the sea level and then an increase in 2012, this might be due to the cyclonic MRV which is also linked with the BiOS circulation. In this case, even though being on the anticyclonic phase, an unusual cyclonic MRV blocks the AIS on its pathway towards the north-Ionian *Bessieres et al.*,2013 [8]. This changing the pressure gradient and reverting the MSC sea level from positive (high pressure) to negative (Low pressure) as seen in Figure. 3.10 and in turn changing the circulation as seen in Figure. 3.11. Here we can see a weakening of the AIS, as well a more strong signal in the ATC (in 2012).

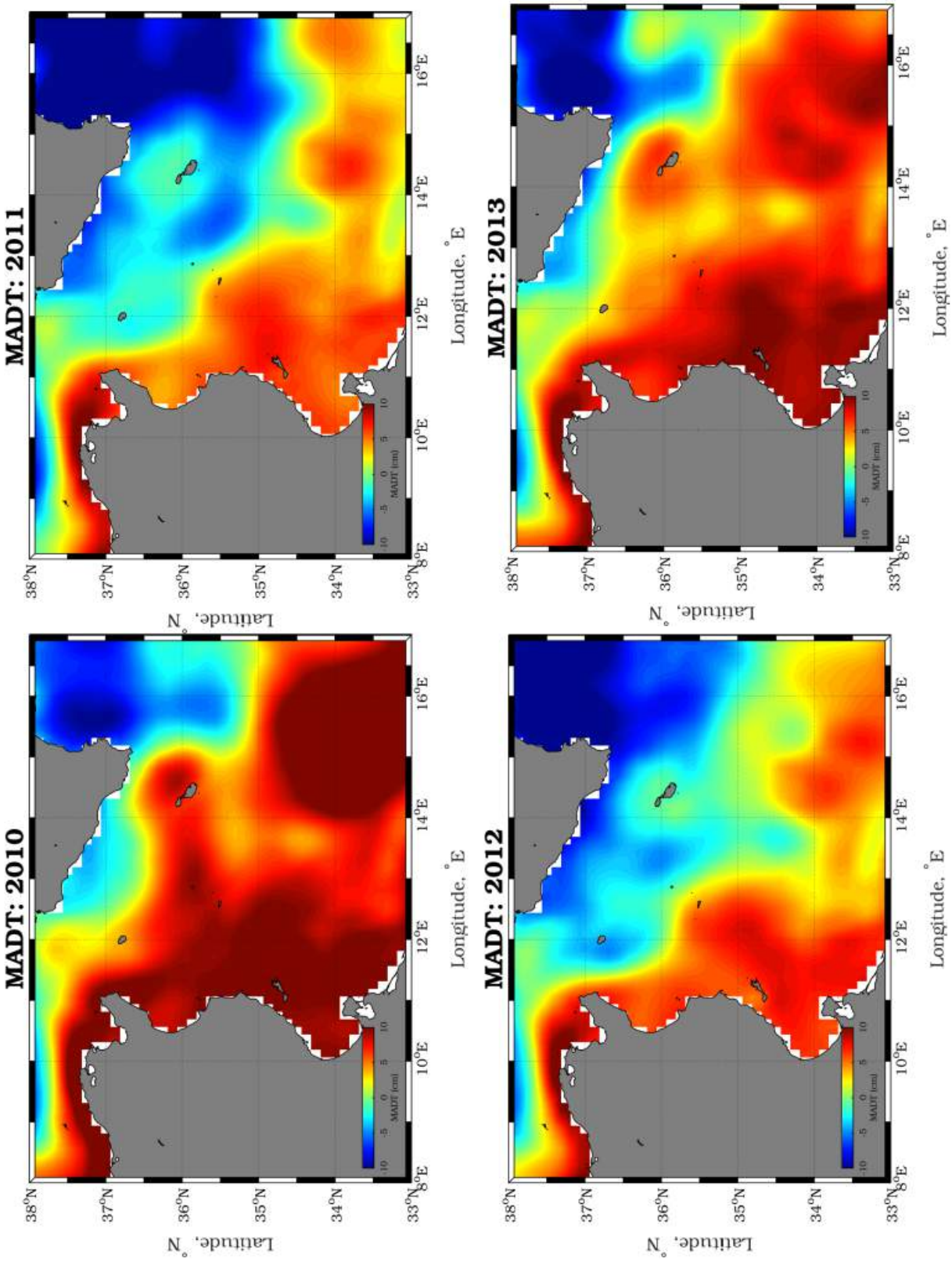

Figure 3.10: Sea surface heights from 2010 to 2013.

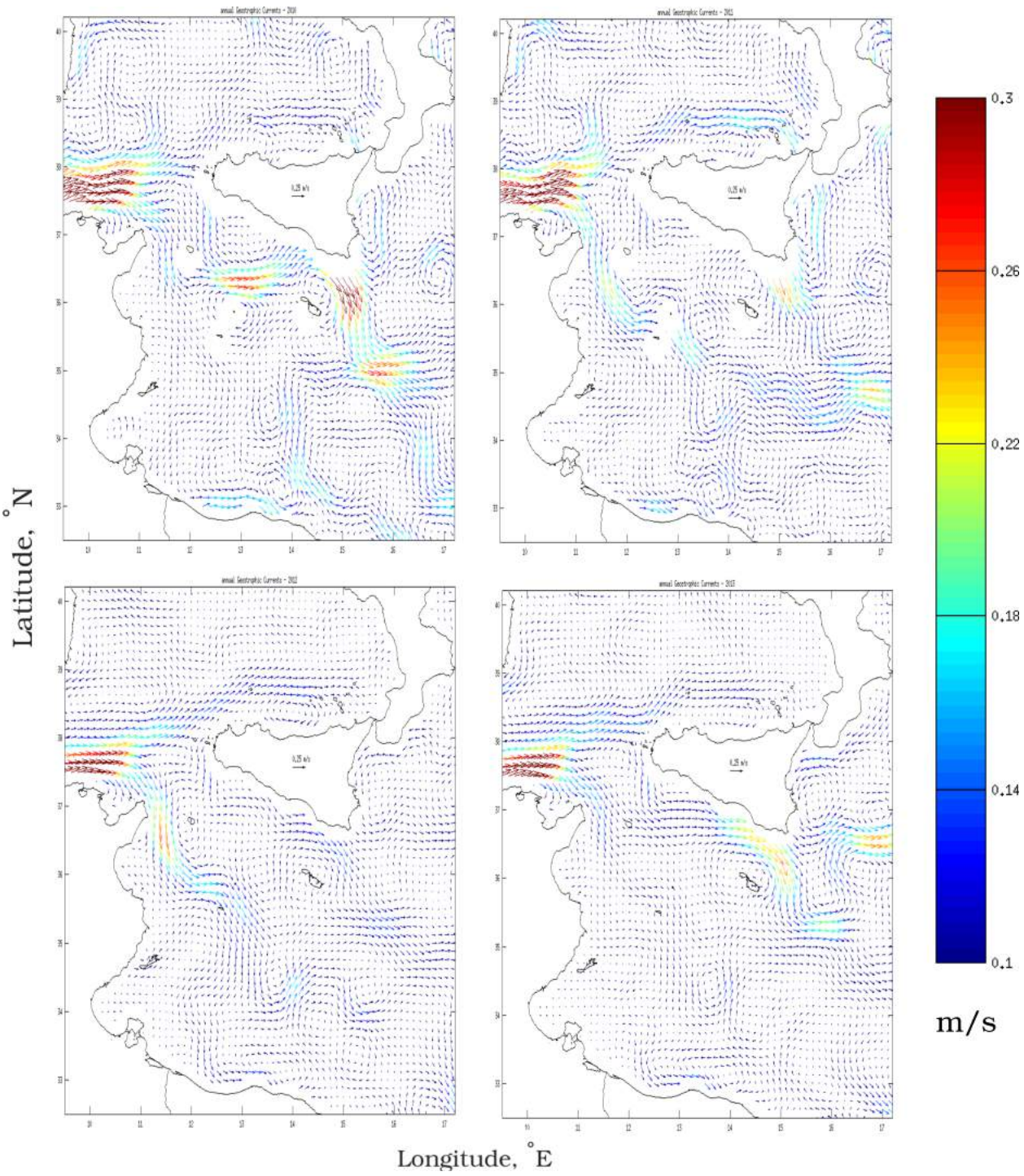

Figure 3.11: Geostrophic Currents from 2010 to 2013.

The second leading mode is depicted in Figure. 3.12. Here the second mode accounts for the 18.5% of the expected variance. Its corresponding PC is semi-periodic, matching with the BiOS phase. For the first anticyclone (1993-1996), since the water is flowing towards the North-Ionian, the sea level drops due to changes in the pressure

gradients. Then the reversal of the North Ionian Gyre (NIG) from anticyclonic to cyclonic (1997-2006), retains Atlantic Water at the MSC, increasing the sea level. For the last anticyclone, again a drop in the sea level can be seen. But due to the influence of the mesoscale close to Messina (cyclonic MRV ∼2010 to 2012) the time series is not as clear as the first anticyclone. The second eigenvector, shows a dipole-like behavior. Negative at the Northwestern side and positive at the southeastern part of the channel, implying a breathing or oscillating mode. In this case the negative part is believed to make reference to the BiOS (which normally appear in the second EOF mode *Bessieres et al.*,2013 [8] and *Vigo et al.*, 2005[111]). Then the positive part explains the Atlantic Tunisian Current (ATC) as well as the Atlantic water entering into the channel through the Sicilian strait. Possible reasons of this behavior could be; cooling in the 1992-2008 period as showed in the its corresponding PC where the MADT is negative for that period and heating for the 2008-2015 as is seen an increment on the sea level of the basin. Other reasons could be; addition or loss of watter mass that enter or exit the strait, or wind driven mass transport along the strait (*Vigo et al.*, 2005[111]).

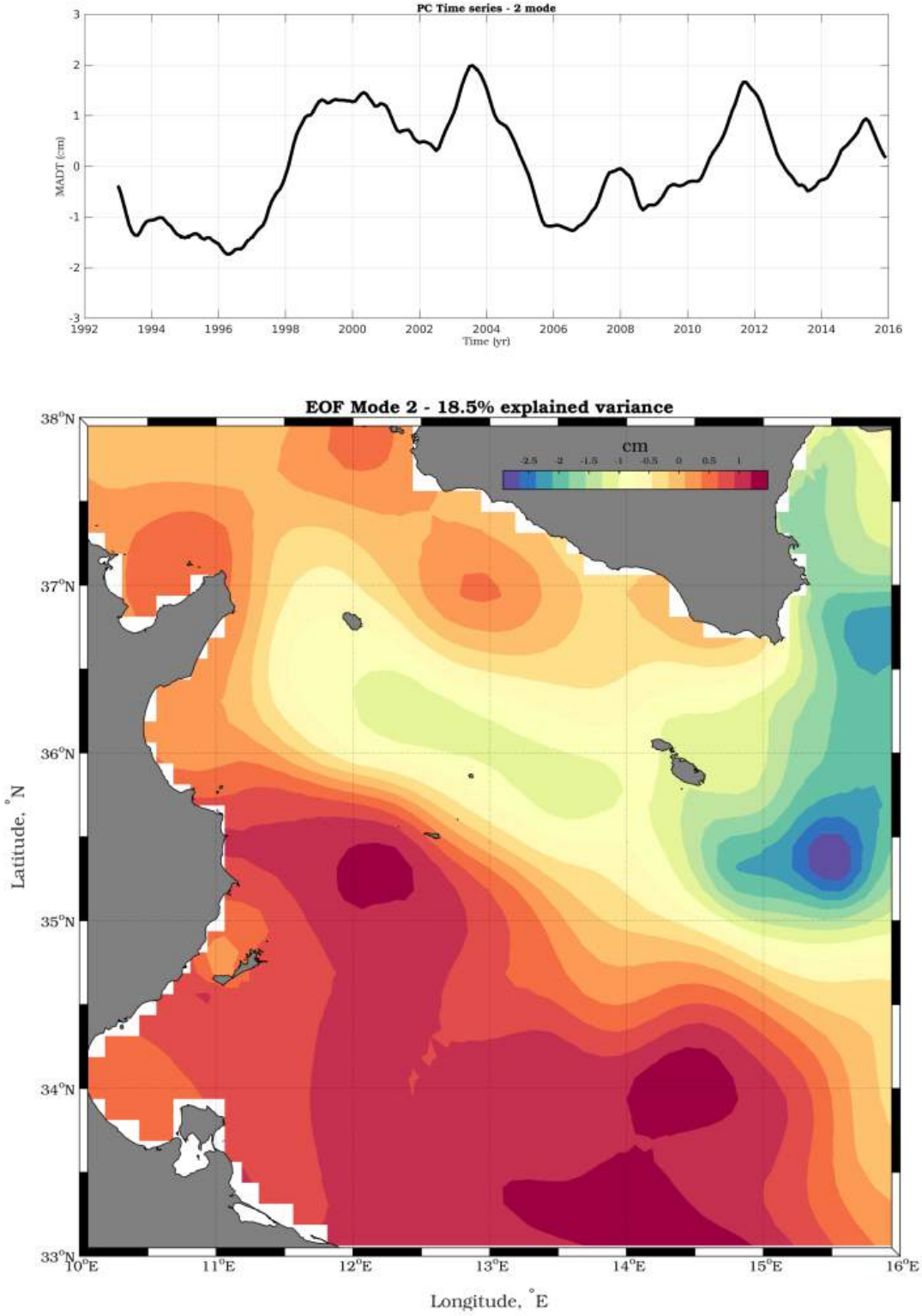

Figure 3.12: Second EOF/PC mode of SSH in the Sicilian channel, dataset spanning from January 1993 to December 2015.

3.1.4 Wind Fields

Surface wind fields were obtained from CCMP (Cross-Calibrated Multi-Platform wind vector analysis) at $1/4 \times 1/4$ degree spatial resolution and 6-hour temporal resolution, spanning from January 1988 to December 2011. Wind stress fields were computed and averaged seasonally for the whole time series available to see its influence on the seasonal patterns.

Fig. 3.13 shows a very strong winter pattern (DJF) which blows south-westward with a strength of $\sim 14 \times 10^{-3}$ N/m^2. For the MAM, JJA and SON the wind influence is not crucial on the enhancing of circulation in the area. For instance for the AIS period we see that the wind is not strong enough so the circulation is mainly thermohaline driven than wind-driven, but the wind helps on reinforcing the current and mixing the water in the Sicily channel.

Wind stress curl fields ($\bigtriangledown \times \tau = d\tau_y/dx - d\tau_x/dy$) in Fig. 3.14 were solved by finite difference method from the wind stress fields. Negative wind stress curl shows places of downwelling or Ekman suction, which happen to be mostly in the Tunisian side of the Sicily channel. On the Sicilian side we can see the contribution of the wind on the upwelling on the Sicilian coast (positive wind stress) as reported by *Drago et al.*, 2003 [28], making this zone of great importance from the biological point of view. One interesting thing is that even for the winter period (DJF), the area close to Sicily maintains the upwelling events probably due to the combined action of the Malta gyre. Then for autumn (SON) and spring, few or no-upwelling events are found even-though the wind seems to be blowing to the same side and with the same strength. For the AIS period (JJA, summer time) there are very recurrent upwelling events in the Sicilian coast. Here momentum and heat are exchanged with the wind, making these events stronger when the thermohaline forcing is stronger (Malta gyre and AIS). Wind forcing gives us an indirect influence in the current field, which even if neglected in the geostrophic approximation, helps to build up the sea level generating the pressure gradient needed to balance the Coriolis force.

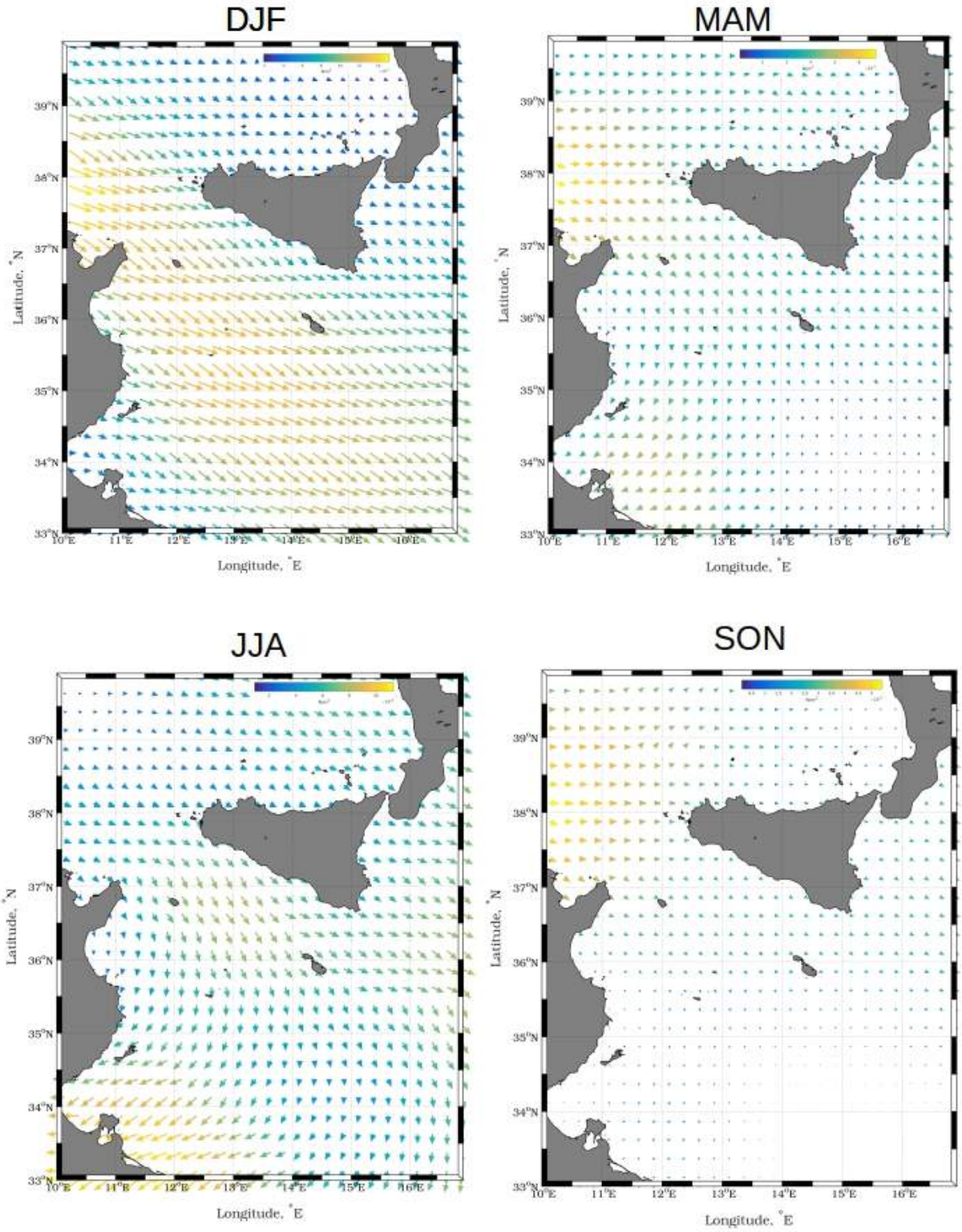

Figure 3.13: Wind stress fields averaged seasonally for the whole CMPP time series available (1988-2011).

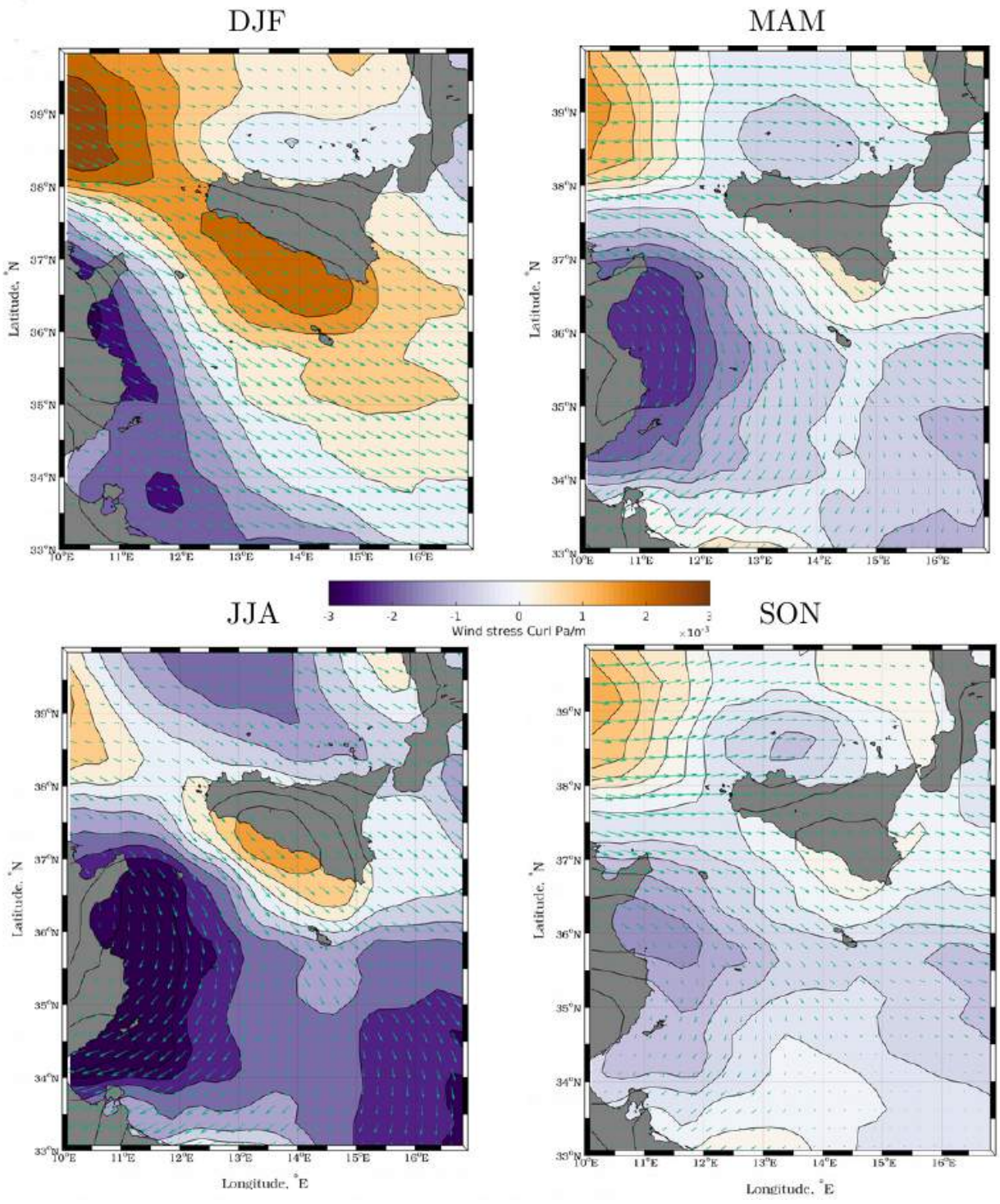

Figure 3.14: Wind stress curls fields averaged seasonally for the whole CMPP time series available (1988-2011). Orange (positive wind stress curl) represents upwelling or Ekman pumping events. Violet (negative wind stress curl) show places of Ekman suction or downwelling. Green arrows represent wind stress as in Fig. 3.13

3.2 The Malta Sicily channel

Large scale studies have shown that, the Sicily channel is a highly dynamic area showing seasonal, intra-annual and inter-annual variability as it was described in the previous section. These studies helped us to understand the main forcing functions and patterns driving the circulation in the Sicilian channel this in order to be able to study the Malta Sicily Channel area, which is the main feature under discussion in this thesis.

With the development of ports and free-ports in Malta, around 20% of all oil transported by sea passes by this area, this heavy marine traffic accounts for an annual flux of 350 million tons of crude oil and refined products, which makes the Malta-Sicily channel a highly risky zone in terms of marine pollution from oil among other hazardous substances [*Drago et al.*, 2003 [28]]. On the other hand, from the fisheries point of view, the limited extend of this area makes the ecosystem vulnerable due to bad fishing practices and unsustainable fishing efforts [*Drago et al.*, 2003 [26]]. For this reason, an appropriate knowledge of the physical and biological oceanography (such as the patterns and dynamical process driving the circulation in the area and the biological transport like fish larval dispersion) for the area is necessary in terms of risk prevention and prediction. This area has been relatively studied, with about 104 CTD stations, 1014 XBT and 1407 MBT within the MEDATLAS-I (1997) where sea current measurements are commonly lacking. Satellite Imagery (thermal infrared images *Philippe and Harange.*, 1982 [83]; *Le Vourch et al.*, 1992 [56]) has helped in the identification of synoptic variability and mesoscale phenomena, in particular the upwelling system along the southern coast of Sicily [*Manzella et al.*, 1988 [63]; *Le Vourch et al.*, 1992 [56]].

High frequency (HF) radars constitute a well established technique capable of resolving accurately oceanic structures in space and time [*Paduan and Graber*, 1997 [80]]. This is specially true, in combination with Lagrangian drifters, floats, Eulerian current measurements, temperature-salinity profiles, satellite imagery and the appropriate analysis tools.

Surface currents measured by high-frequency radar were mapped from the computation of hourly surface current vectors in the Malta-Sicily channel spanning two years from August 2012 to January 2015. The array of the high-frequency (13.5 MHz) direction-finding stile system (CODAR Ocean Sensor, angular resolution 5°, range resolution 1.6 Km) was set at Ta'Sopu (Malta), Ta'Barkat (Malta) and Pozzallo Harbor (Sicily) as in Figure.2.8. Those hourly data are organized in time series of hourly averaged velocity vectors with u (Meridional, East-West) and v (Latitudinal, North-South) components of the total velocity.

The dataset has been provided by A. Drago from the University of Malta and were collected as part of the Calypso project [16] partly sponsored by European Union Founding (EU). The CALYPSO system operating set-up and resolution, provides radar measurements that are representative of the surface 1 m ocean layer over ocean grid sizes in the range of 0.3-8.3 Km^2. The radars share the same transmit frequency using a GPS-synchronization module, and operate with both the ideal and measured antenna beam patterns. Hourly sea surface current maps are derived on a Cartesian grid with 3×3 km^2 horizontal resolution by least-squares fitting of the radial components of the ocean currents from two or more radar stations in areas of common overlap. Grid points were included in the analysis just if they satisfied a minimum data return of 50% (*Cosoli et al.*, 2015 [23]).

High frequency radars provide continuous time series which can be exploited using different methods of analysis such as spectral analysis. The spectral analysis is used in order to describe the distribution (over frequency) of the power contained in the signal, based on a finite set of data. We estimated the power spectral density (PSD) using the *non-parametric* Welch method, in which the PSD is estimated from the signal itself (*Welch*, 1967[112]).

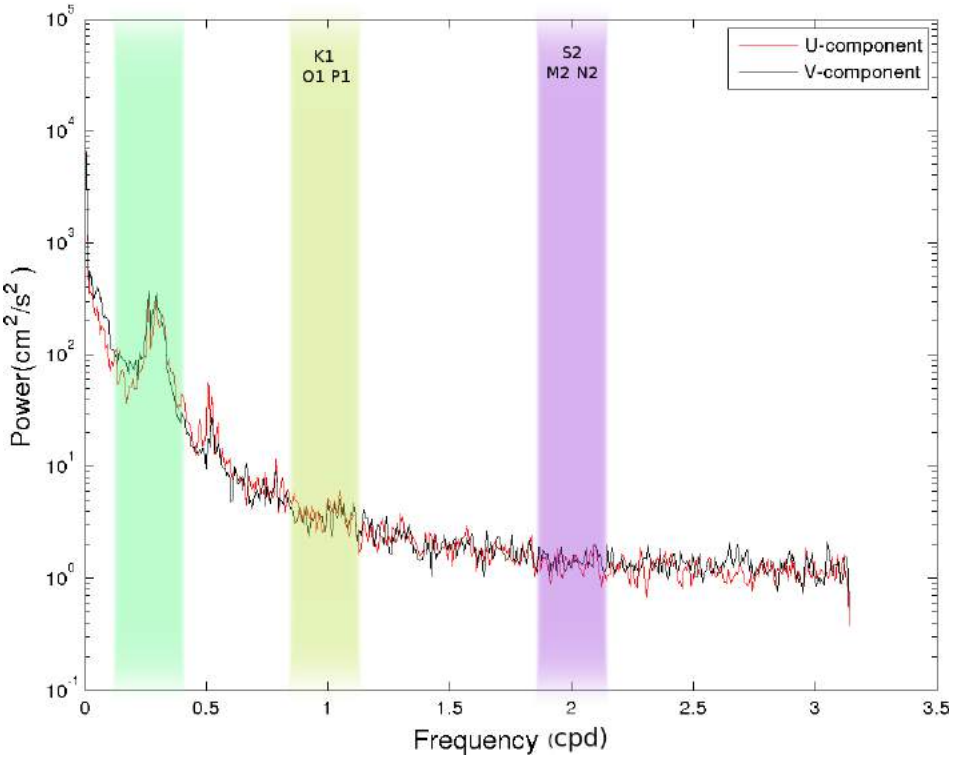

Figure 3.15: Power spectra of HF-radar components showing diurnal K1, O1, P1 (1 cpd, yellow shaded area) and semi-diurnal M2, S2, N2 (2 cpd, purple shaded area) tidal components in the Malta Sicily Channel.

In Figure 3.15, some fundamental frequencies have been identified at 1 cpd and 2 cpd, such as frequencies belong to diurnal K1, O1, P1 and semi-diurnal M2, S2, N2 which agree with *Cosoli et al.*, 2015 [23]. It is seen that some low frequencies with periods greater than 20 hours appear to highly influence the area, like barotrophic, non tidal wind-driven components and inertial oscillations. The latter were proved to be present thanks to the deployment of some drifters from the National Institute of Oceanography and Experimental Geophysics (OGS) on June 2013. The trajectories include oscillations $\sim$ 24 hours. Figure. 3.16, shows the strong influence of the AIS where one of the drifters followed the Atlantic Ionian Stream Pathway.

On the other hand, drifter trajectories can be used as a way to validate the data obtained from the HF Radars [*Shadden et al.*, 2009 [101], *Chiang et al.*, 2013 [19], *Salabarrieta et al.*, 2013 [102], *Salabarrieta et al.*, 2016[103]]. This can be done generating numerical particles or drifters that are set with the HFR velocities, which in turn "predict" the possible trajectories from the real ones. For this area, as we addressed in section. 2.2.4, we selected three drifter deployments from the Instituto Nazionale di Oceanografia e Geofisica Sperimentale (INOGS), one in September and October 2013 and the other one in March 2014 [1]. Since our coverage is not good at all grid points, mostly due to the addition of a third antenna in Sicily around September 2013 as well as gaps due to geometric distortion of precision (GDOP). The numerical drifters were deployed over a grid in which there was at least 95% of the data for the whole time span (August 2012 to January 2015; see Figure. 3.17). This algorithm will stop the numerical particles when it encounters no data. This is because within 95% coverage area, the observations were linearly interpolated in order to have contiguous data.

[1]This dataset can be found at OGS page, inside the Argo / drifters project `http://nettuno.ogs.trieste.it/sire/drifter_italy.php?active=0`

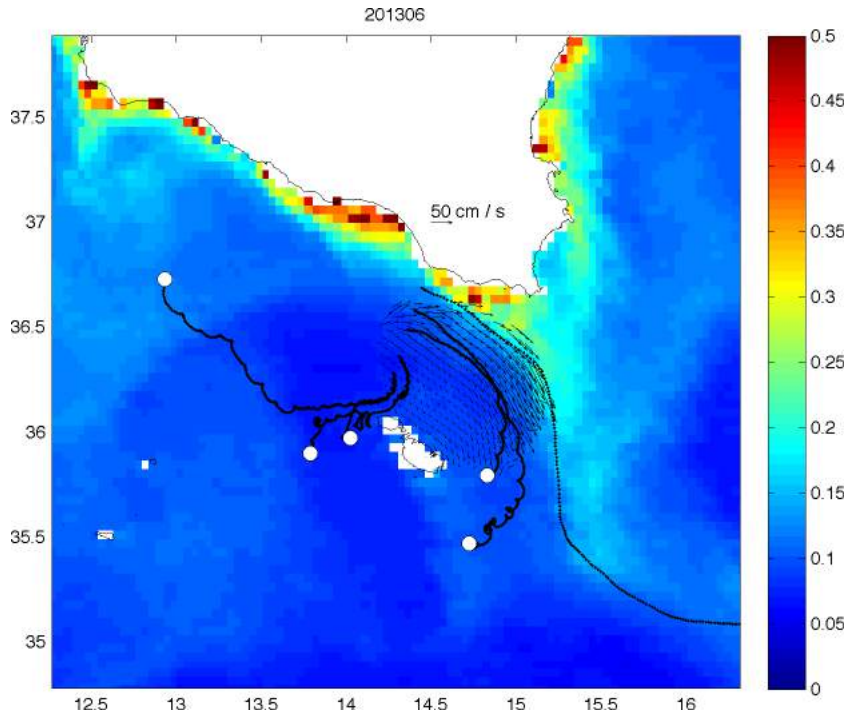

Figure 3.16: 1 month recording trajectories from Drifters deployed on July 2013 by the National Institute of Oceanography and Experimental Geophysics OGS (image has been provided by Dr. Simone Cosoli by official mail).

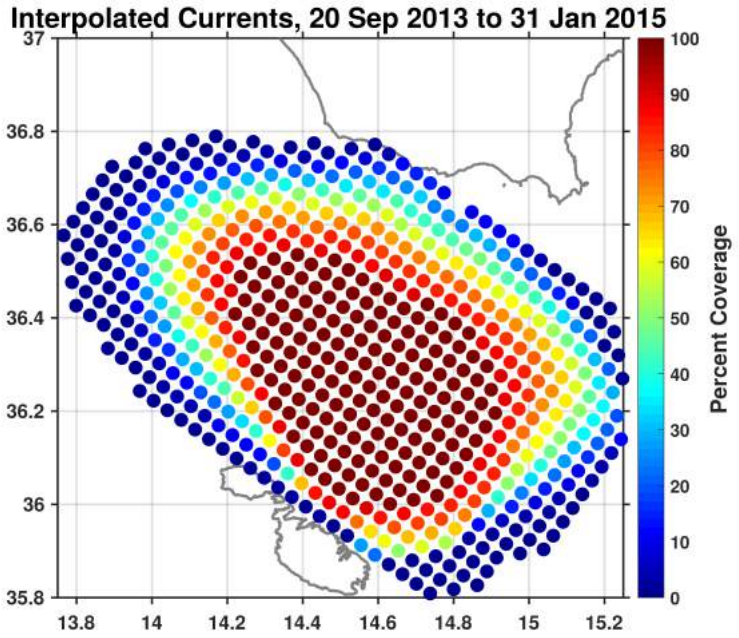

Figure 3.17: Interpolated best grid coverage from HFR datasets. Here each grid point satisfies a minimum data return of 95%.

Numerical drifters were deployed every 24 hours at different points of the real drifters trajectories since after a period of more or less a day the numerical and the real drifters will be way apart one from each other or will leave the domain [*Salabarrieta et al.*, 2016[103]]. Figure. 3.18 show numerical drifters in black and real ones in red, where green dots represent the locations where numerical drifters were deployed after 24 hours. As we can see, in the upper panel both the numerical and real drifters were trapped presumably by the MS gyre. In the case of M4906, the drifters were outside the selected grid and probably advected by the gyre wiggling north of the domain. The drifters corresponding to October and September leave the channel after a day and the numerical drifter seem to follow them pretty well. Special attention should be given to drifters referenced as O4883 and S4882. The fist case exhibits inertial currents and the second case shows poor agreement with the numerical trajectories trending perpendicularly to the drifter trajectory.

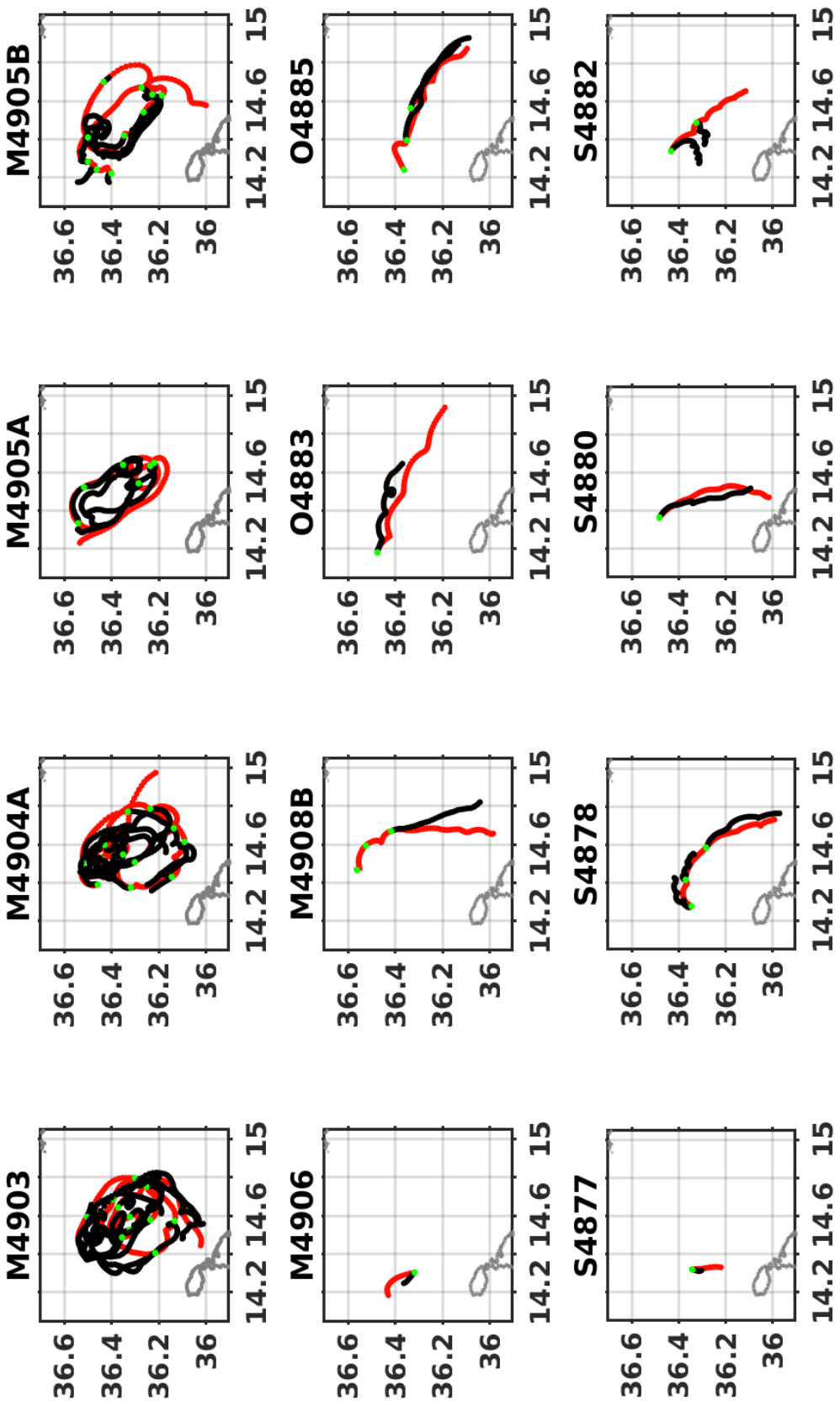

Figure 3.18: Show numerical (black) and real (red) drifters. The numbers represent the OGS identification number and the letter in front of them represent the month in which the drifter was deployed. Green dots represents the places in which the numerical drifters were deployed.

Calculation of the separation distance between the numerical particles and the real drifters is useful for the HFR data validation [*Shadden et al.*, 2009 [101], *Chiang et al.*, 2013 [19], *Salabarrieta et al.*, 2013 [102], *Salabarrieta et al.*, 2016[103]]. Figure. 3.19 shows the separation distance of the numerical and real drifters up to 72 h. After a day, the separation between the drifters is to big ($\sim$ 9 km) and the drifters (numerical and real) are way apart one from each other. Moreover, HFR data is able to reproduce real drifter trajectories in the first hours of deployment, even if the drifters account for velocities 10 m below the surface (this due to the drogue is placed at 10 m below the surface).

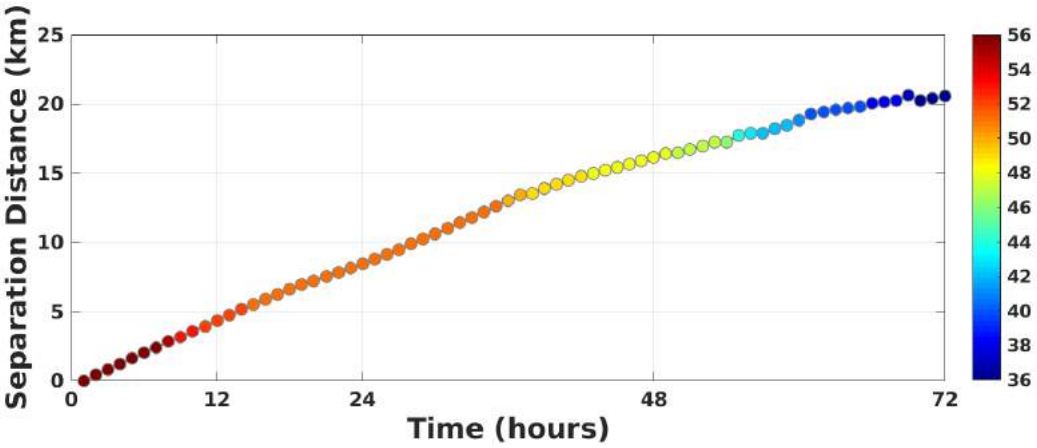

Figure 3.19: Separation distance between the numerical drifters computed from HFR and the real ones deployed by OGS in October and September 2013 and March 2014. Colorbar represents the number of numerical drifters with a separation distance $x(t)$ at certain time t over the grid in Figure. 3.17.

3.2.1 Correlation coefficients

As we mentioned before, due to the good coverage of our time series, we are able also to extract the spatial information of the HF radar data using techniques such as computing the spatial correlation coefficients. We used the Pearson product-moment correlation coefficient, which has been widely used as a measure of the degree of linear dependence between two variables X and Y (giving a value between +1 and –1. +1 represents total positive correlation, 0 is no correlation, and –1 is total negative correlation), to calculate the spatial correlation coefficients from the time series.

Pearson's correlation coefficient is the covariance of the two variables ,$\mathbf{C}(\mathbf{x}, \mathbf{x}')$, divided by the product of their standard deviations, σ. The form of the definition involves a "product moment", that is, the mean (the first moment about the origin) of the product of the mean-adjusted random variables; hence the modifier product-moment is the same.

The correlation coefficient $\rho(\mathbf{x}, \mathbf{x}')$, between any two grid points is,

$$\begin{aligned}\rho(\mathbf{x}, \mathbf{x}') &= \begin{bmatrix} \frac{1}{\sigma_u(\mathbf{x})} & 0 \\ 0 & \frac{1}{v(\mathbf{x})} \end{bmatrix} \mathbf{C}(\mathbf{x}, \mathbf{x}') \begin{bmatrix} \frac{1}{\sigma_u(\mathbf{x}')} & 0 \\ 0 & \frac{1}{\sigma_v(\mathbf{x}')} \end{bmatrix} \\ &= \begin{bmatrix} \rho_{uu} & \rho_{uv} \\ \rho_{vu} & \rho_{vv} \end{bmatrix}\end{aligned} \tag{3.1}$$

The correlation coefficients in Eq. 3.1, between surface currents at different grid points show the statistical spatial structure of surface currents such as the decorrelation length scale ($\sim$ 30 km for u and $\sim$ 95 km for v and u-v) and the shape of the correlation function. For decorrelation scale we reefer to the number of lags that takes for the autocorrelation function to reach zero correlation. If the process is very random the time (length) scale will be very short. Whereas if the process is persistent then the time (length) scale will be longer. The decorrelation length scale characterizes the typical scales of variability, and the correlation can identify inconsistent or abrupt features in the spatial domain and detect bad points.

The correlations of meridional (east-west) currents, $\rho_{uu}(\mathbf{x}, \mathbf{x}')$ between a central point of the grid ($\mathbf{x}$) and all other points ($\mathbf{x}'$) are shown in Figure. 3.20.

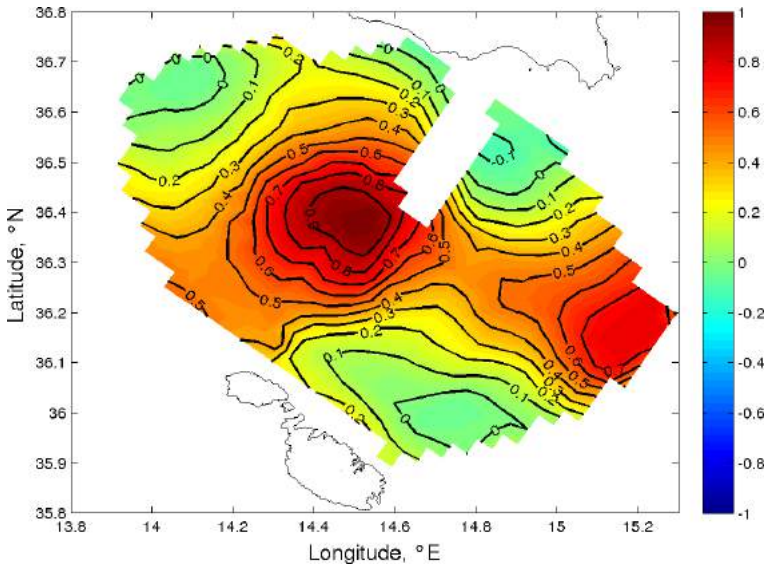

Figure 3.20: U Spatial correlation between a central point of the grid with the ones surrounding.

In the same way, the correlations of latitudinal (north-south) currents $\rho_{vv}(\mathbf{x}, \mathbf{x}')$, are shown in Figure. 3.21.

A Gaussian-like shape can be seen from the correlation of meridional currents meanwhile for the north-south flows is more elliptic having a more directional preference than the east-west ones. The cross-correlation, $\rho_{uv}(\mathbf{x}, \mathbf{x}')$ its seen to have more

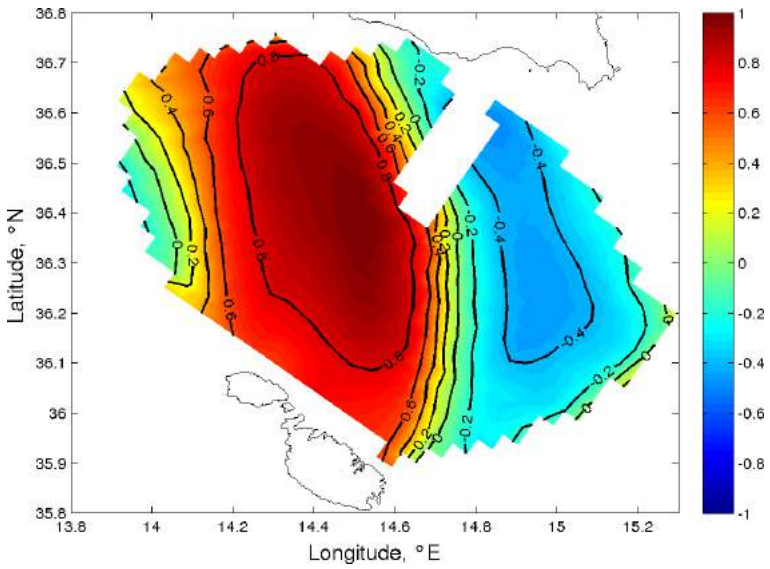

Figure 3.21: V Spatial correlation between a central point of the grid with the ones surrounding.

complicated structures in space and being u mostly anti-correlated with v Figure. 3.22.

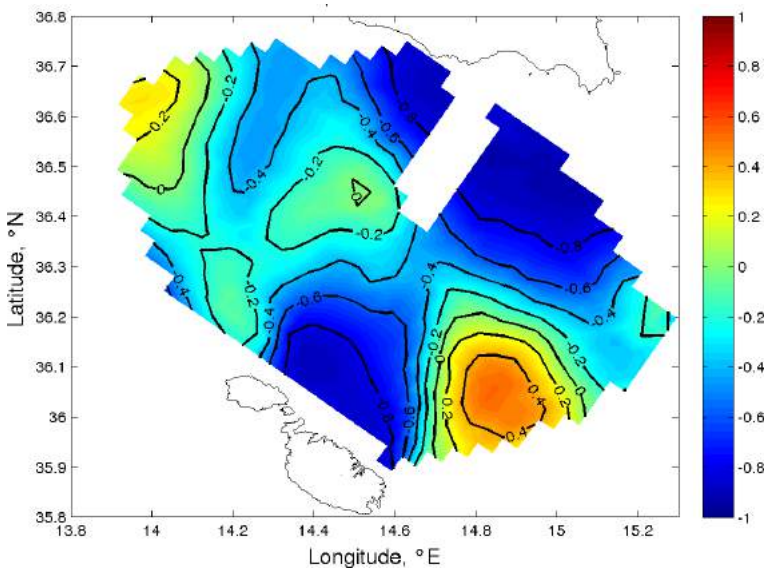

Figure 3.22: U-V Spatial correlation between a central point of the grid with the ones surrounding.

3.2.2 Comparison among available spatial data

Currents in the ocean can be depicted as a result of geostrophic plus wind driven components. HF Radars offer besides resolution in time and space, the capability of measure near real time and complete currents [*Paduan and washburn*, 2013 [82]],

in the sense that we have a measure of both, wind-driven and geostrophic currents influencing the sea surface. A time series comparison of the data is depicted section. 3.3 Fig. 3.27 and 3.28.

Altimetry data can help in calculating surface geostrophic velocity fields as we saw in section 2.1.4. In Figure. 3.23 the velocity field from HF radar fits quite well with the geostrophic velocity field, which means that the Malta-Sicily channel is in geostrophic balance at weekly and monthly time scales. Geostrophic balance was identified for all the period studied (August 2012-November 2013). The stretching and squeezing of the anticyclonic gyre described with the HF radar data is now shown clearly. This mesoscale anticyclonic gyre is about $\sim$ 80 km wide and seems to drive the circulation in the area together with the AIS which was also identified through out the the geostrophic velocity field.

Wind forcing give us an indirect influence in the current field (at larger time scales, like weekly and monthly), which even if neglected in the geostrophic approximation, helps to build up the sea level generating the pressure gradient needed to balance the Coriolis force.

Other available spatial observations for this area include satellite derived SST and CHL. 12 months of satellite data from January to December 2013 shows clearly a variable and complex SST field. The AIS evolution towards the east varies from 17° to 26°C at the end of summer. Figure. 3.24 show the AIS as it flows toward the Ionian. A well defined front is seen, which do not allow mixing in the area. This front is also seen to be strongly influenced by the AIS which at follows is controlled by bathymetry and thermohaline driven.

Generally water masses on the south-eastern coastal area of Malta are associated with the circulation of the mesoscale anticyclonic gyre described around the island, which tends to trap water against the coast maintaining slightly higher temperatures (*Drago et al.*, 2010.[27]).

Monthly data of chlorophyll concentration form August 2012 to December 2013 show the geostrophic current field (the mesoscale anticyclonic gyre and the Atlantic Ionian Stream) not only drives the circulation but advects the nutrients in the area as well. In this case, chlorophyll data follows almost perfectly the geostrophic current over the dataset available. It is seen a well defined front which confines chlorophyll concentration as described with SST data. This front separates the channel into two zones; one with high chlorophyll concentration from another with low concentration. This is due to the specific properties of the AIS which moves Chlorophyll along all the coast of Sicily (Figure. 3.25).

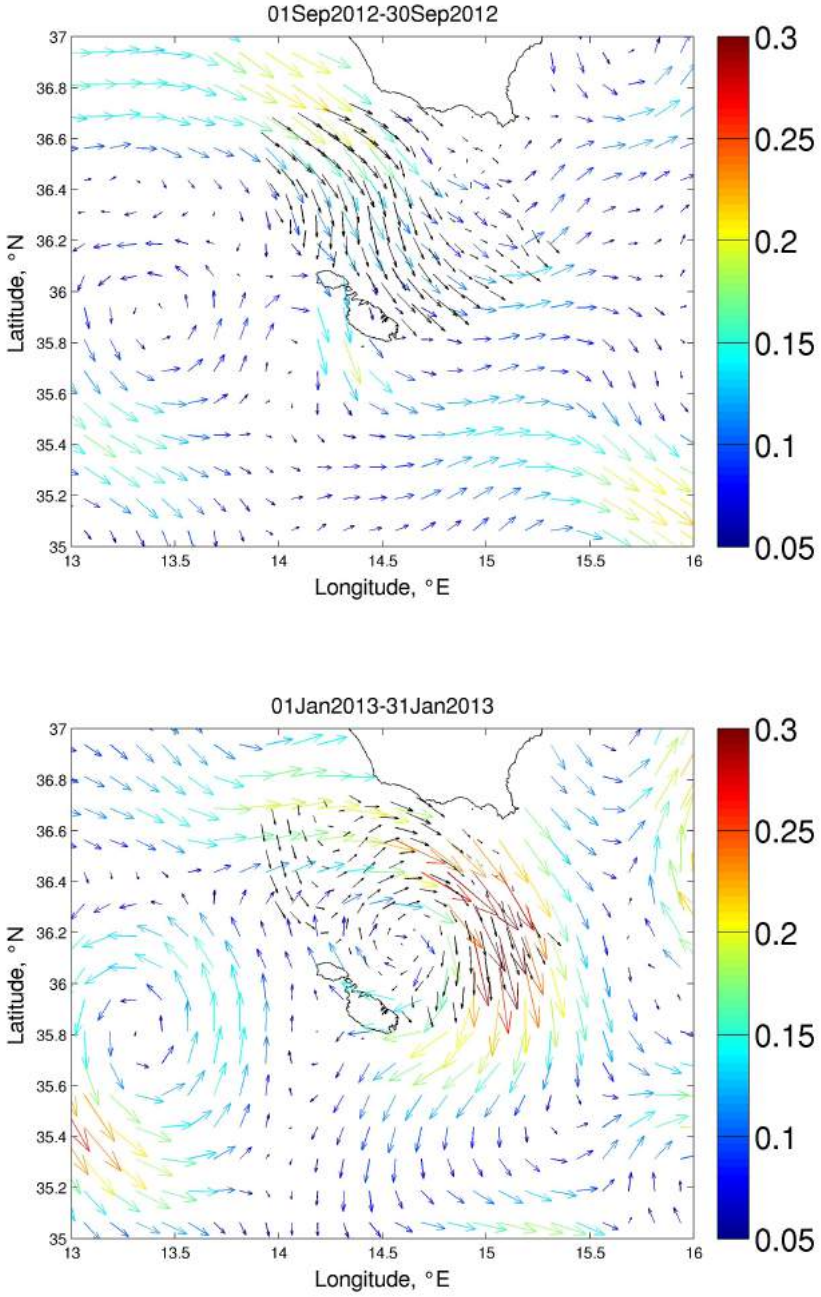

Figure 3.23: Geostrophic currents calculated form altimetry datasets, showing the mesoscale anticyclonic gyre identified on February 2014 (down) and the pathway of Atlantic Ionian Stream on September 2012 (down). Black lines represent the current field form HF radar data. Color arrows represent the geostrophic current field and colorbar gives the magnitude of each velocity vector.

In summer, a really strong influence of the AIS is shown transporting and confining chlorophyll along the Sicilian coast. However in winter due to strong mixing, the

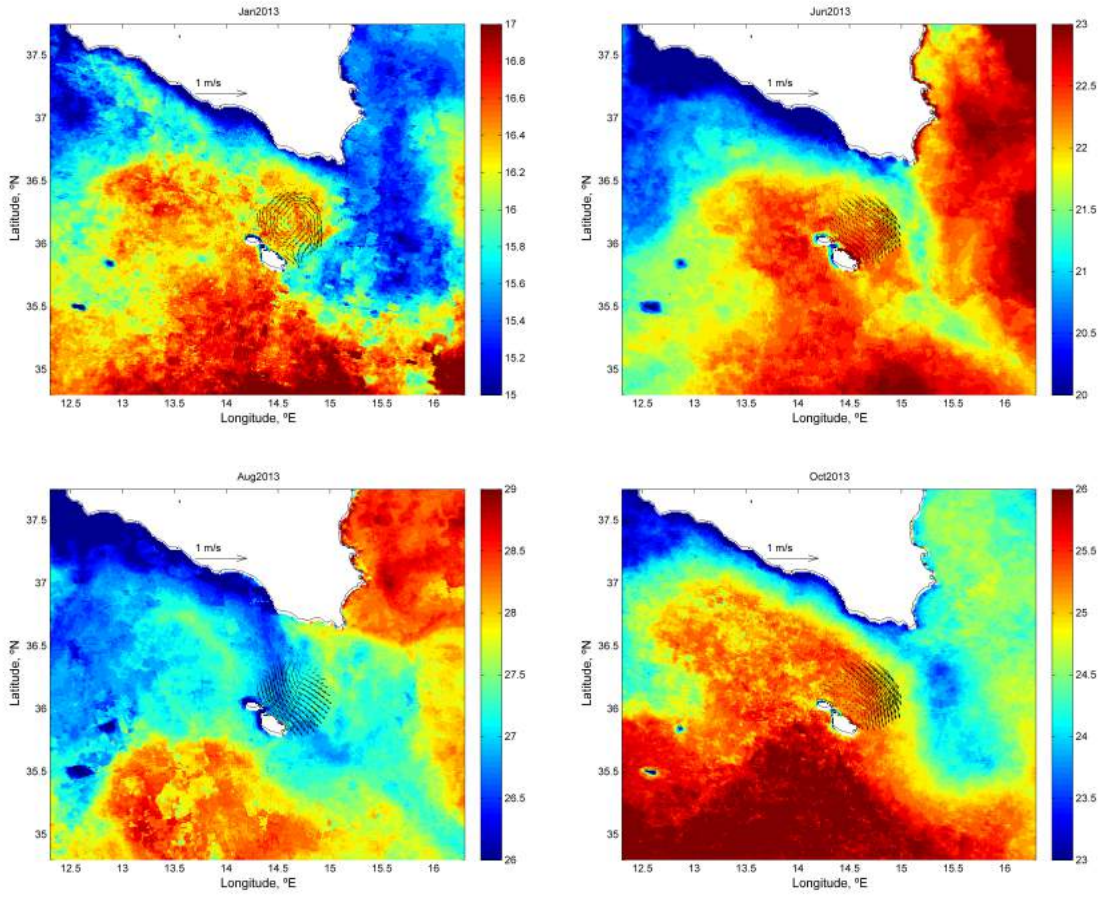

Figure 3.24: Sea surface temperature from Aqua/MODIS satellite mission showing the mesoscale anticyclonic gyre on January 2013 (upper left) and the Atlantic Ionian Stream pathway on May, August and October 2013. Black lines represent current field form HF radar data and the Temperature in °C.

transport in the area is principally driven by the mesoscale anticyclonic gyre. Then, due to this processes phytoplankton biomass can increase giving a proxy for fishing in the Malta-Sicily channel. Upwelling in this zone seems to be driven by currents more than by wind-driven circulation, as we saw in the Section. 3.1.4. Upwelling follow the whole Southern coast of Sicily and extends offshore significantly. This results also show persistent upwelling for almost the whole year, being more evident in summer and winter when the water column becomes well stratified and the thermocline is able to arise close to the southern part of the Sicilian coast. In summer the upwelling is more probable to be driven by the action of the AIS.

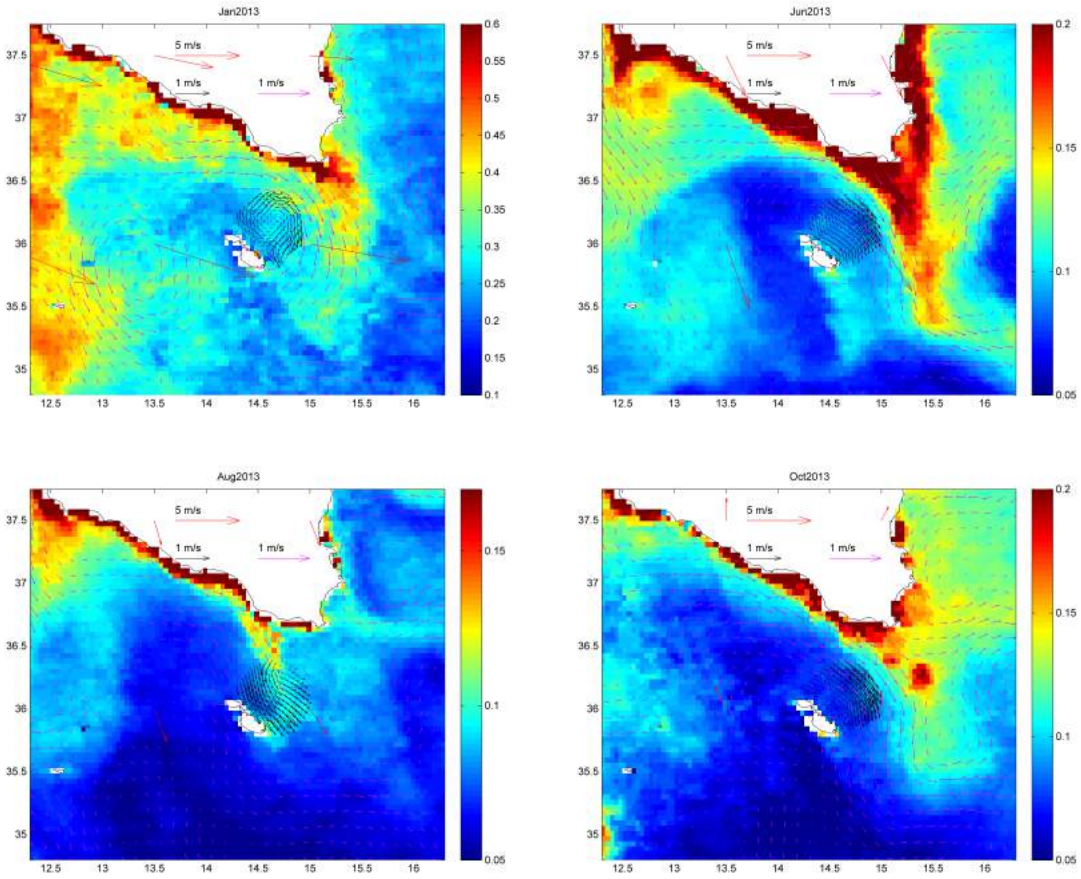

Figure 3.25: Chlorophyll concentration from NOAA N' satellite mission showing the influence of the mesoscale anticyclonic gyre and the Atlantic Ionian Stream on the Malta-Sicily channel on August 2012, January, March and October 2013. Black lines represent current field form HF radar data, magenta lines the geostrophic velocity field, red ones the wind velocity field and the colorbar represents chlorophyll concentration in mg $pigment/\mathrm{m}^3$.

3.3 Short time scales in the Malta-Sicily channel

In the previous section we saw that at longer time scales (weekly and so on), the circulation behaves in geostrophic balance. Here we want to include the total flow that is measured by the HF radar, which has both the geostrophic (low frequency) and wind driven flow (wind driven can support both high frequency as well as low frequency motions). Since we are interested in the high frequency motions which are generated in shorter time scales (from hours to days), from the original HFR grid, a subset from 13.5-15.5°E to 35.8-36.8°N was subtracted in order to compare with the wind and the geostrophic currents. We interpolate the grids to a 0.25 degree 6×7 grid for each of the datasets as in Figure. 3.26.

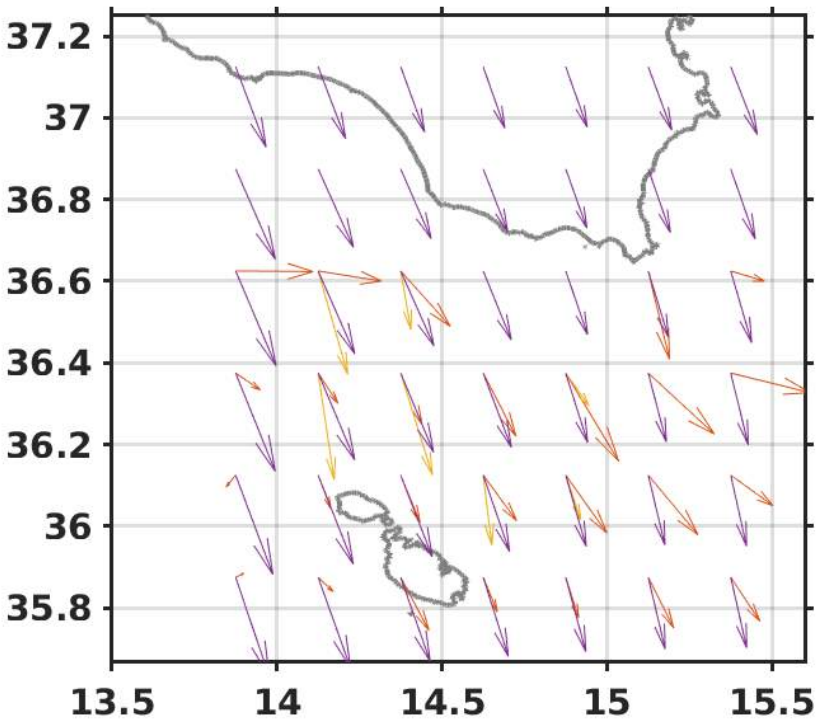

Figure 3.26: Interpolated grid for each of the datasets. Violet arrows represent wind vectors, red arrows represent geostrophic currents derived from MADT data and yellow arrows are the velocity vectors from HFR on 01 August 2012.

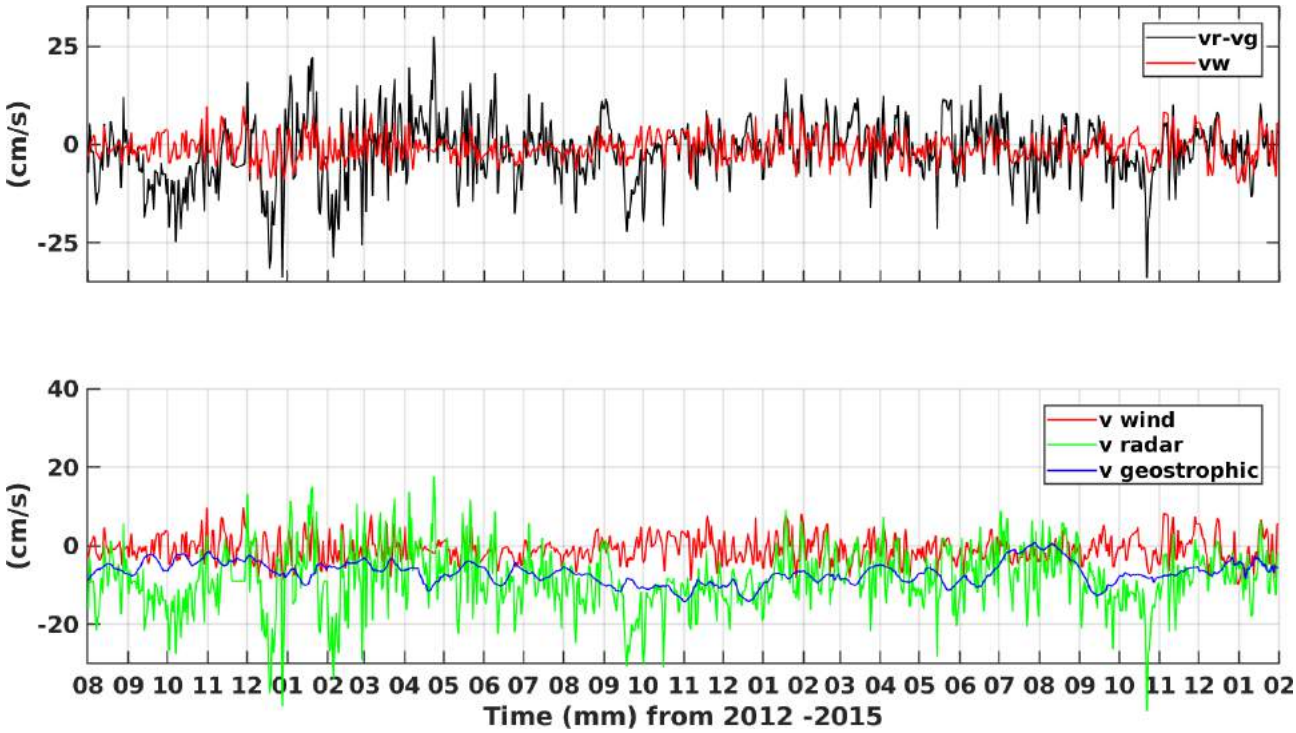

Figure 3.28: V component time series of Wind, geostrophic and HFR velocities. Upper panel compares the residual latitudinal (North-South) v velocity ($V_{residual} = V_{radar} - V_{geostrophic}$) with the latitudinal v velocity wind component. Lower panel shows the time series of each dataset; wind (red), geostrophic (blue) and HF radar (green).

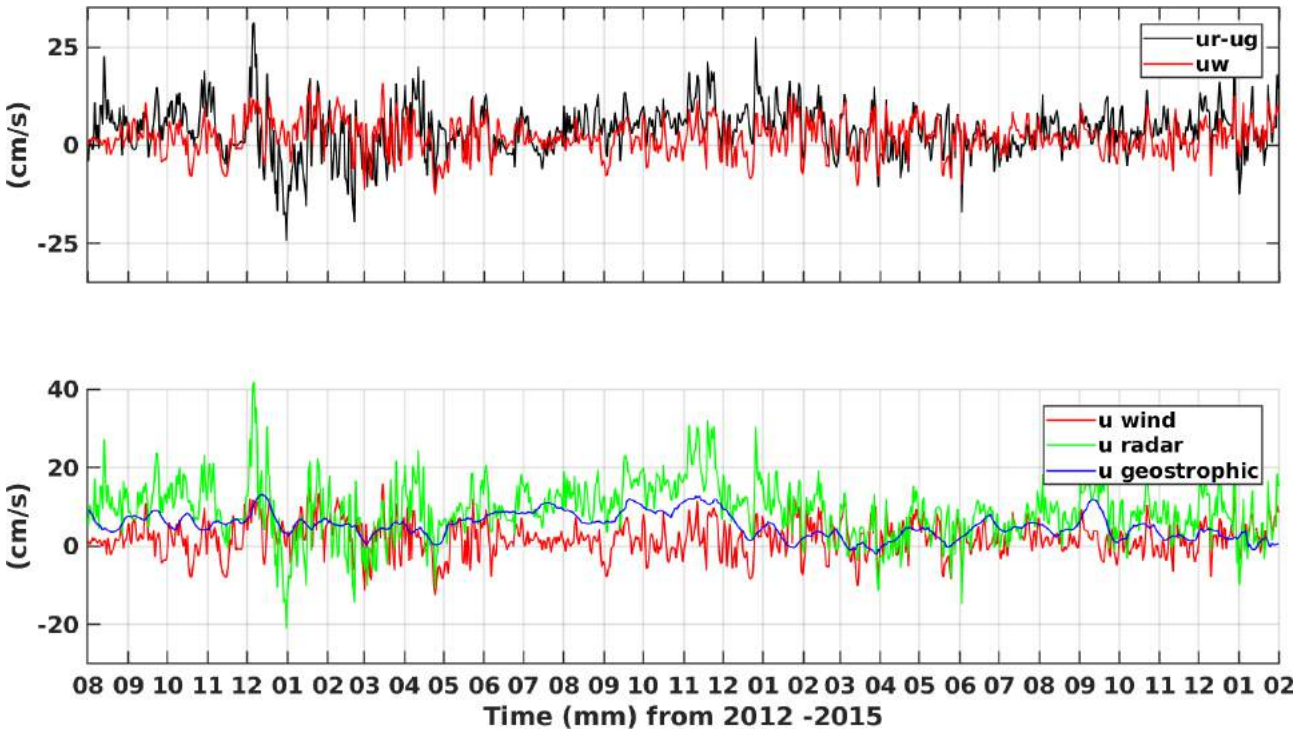

Figure 3.27: U component time series of Wind, geostrophic and HFR velocities. Upper panel compares the residual meridional (East-West) u velocity ($U_{residual} = U_{radar} - U_{geostrophic}$) with the meridional u velocity wind component. Lower panel shows the time series of each dataset; wind (red), geostrophic (blue) and HF radar (green).

Figure. 3.27 and 3.28, show the times series of each dataset on the interpolated grid. The upper panel compares the wind velocity time series with the residual velocity. This residual velocity is the result of geostrophic velocities subtracted from HFR ones i.e, we are getting rid of the geostrophic component of the velocity (as we saw in section. 2.1 velocity has a geostrophic and wind-driven components), which should be in pretty much agreement with the wind velocities. Here, the u component shows good agreement with the residual as expected except from some time intervals such that January to March 2013 in which the time series are behaving opposite; one is positive (wind) and the other negative and stronger (residual). The latitudinal v residual component of the velocity behaves differently from the wind on the first months (until September 2013), then is in agreement with some variation on the strength of the current. This is possibly due to data availability since the HFR have data missing on some parts of the grid (as seen in Figure. 3.26) in the averaging process they might play an important role on the magnitude of the vectors. For the comparison of the three datasets (lower panel in Figure. 3.28), the geostrophic v component look like a low pass filter of the HFR time series from (October 2013), with some high frequencies being in agreement with the wind. On the other hand wind and radar time series have more variability since most of the high frequency motions

are included. Whereas for the geostrophic one, since the adjustment happens in a longer time scale, we can see it a low pass filter of the time series. In this sense, we can see that at shorter time scales the wind plays an important role on the circulation of the channel.

3.3.1 Complex correlation.

As *Kundu*, 1976 [53] described, the phase angle of the complex correlation coefficient is a good measure of the average relative angular displacement (veering) between a pair of two-dimensional vector series. This method, as described in section. 2.2.7, has been used to compute the vectorial correlation over our interpolated time series described above (Fig. 3.28, 3.27). In this velocity decomposition we expect that the components of the residual currents should be most related with the wind. We tested this hypothesis using complex or vectorial correlation, in order to obtain the Ekman veering or the phase angle of the complex correlation coefficient over the grid in Figure. 3.29.

Table. 3.3.1 shows complex correlation coefficients and veering angles for each time series (HFR, geostrophy, residual) with the wind.

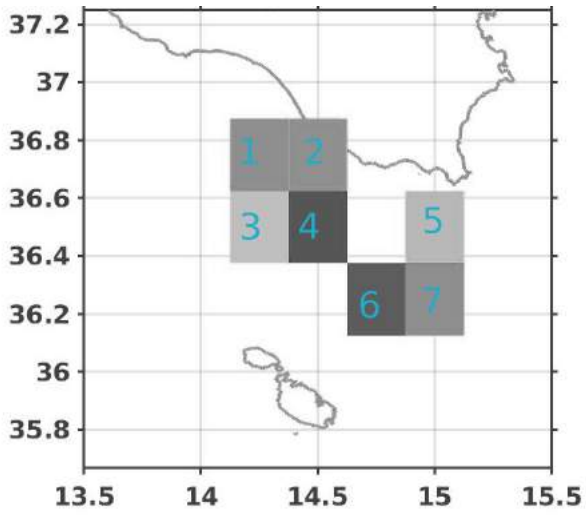

Figure 3.29: grid cells where complex correlation is computed. Number are used to reference each parameter to the grid point which they belong to. So, p_1, θ_1 are the parameters corresponding to box 1.

Time series	correlation coefficient	Phase angle
Residual to wind	$p_1 = 0.4669$	$\theta_1 = 37.9316$
	$p_2 = 0.3749$	$\theta_2 = 38.9211$
	$p_3 = 0.4030$	$\theta_3 = 49.3575$
	$p_4 = 0.4424$	$\theta_4 = 31.4394$
	$p_5 = 0.3145$	$\theta_5 = 45.5068$
	$p_6 = 0.2920$	$\theta_6 = 59.7371$
	$p_7 = 0.3202$	$\theta_7 = 42.1535$
Radar to wind	$p_1 = 0.3848$	$\theta_1 = 34.1950$
	$p_2 = 0.3586$	$\theta_2 = 36.9490$
	$p_3 = 0.3515$	$\theta_3 = 40.1103$
	$p_4 = 0.3554$	$\theta_4 = 23.1126$
	$p_5 = 0.3249$	$\theta_5 = 44.4289$
	$p_6 = 0.2475$	$\theta_6 = 53.4827$
	$p_7 = 0.2971$	$\theta_7 = 33.9368$
Geostrophic to wind	$p_1 = 0.0566$	$\theta_1 = -101.4697$
	$p_2 = 0.0230$	$\theta_2 = -14.4575$
	$p_3 = 0.1082$	$\theta_3 = -86.2521$
	$p_4 = 0.0876$	$\theta_4 = -97.4430$
	$p_5 = 0.0511$	$\theta_5 = -34.6377$
	$p_6 = 0.0961$	$\theta_6 = -99.0749$
	$p_7 = 0.0712$	$\theta_7 = -91.4430$

Radar to the wind complex correlation (as seen in table. 3.3.1) show the Ekman veering ∼40 degrees to the right (which in Ekman theory is 45 degrees to the right). Here we find angles oscillating between 23 to 53 degrees of the velocity vector to the wind vector, with correlation between 0.24 to 0.35 demonstrating that wind forcing is important at shorter time scales and that an Ekman layer is set as well. This results are also true for the residual to wind vector correlation, with higher correlation coefficients and with θ closer to 45 degrees, this since geostrophic components have been removed from the time series (see Table. 3.3.1). On the other hand, as expected, the complex correlation between the geostrophic flow and the wind is really low, since processes in both time series evolve at different time scales. Being the wind component at short time scales imputing rapid and variable motions into the ocean, whereas the geostrophic field evolves at larger scales accounting for low frequency phenomena.

3.3.2 The Malta Sicily gyre

As stated in section. 3.1, there is evidence of mesoscale activity in the Malta Sicily channel. Such structure has been evidenced by the datasets studied in this thesis; for instance MADT, HFR, CHL and SST. In order to individuate the mesoscales in the MSC, we compute vorticity in the time series using the method described by *Sanderson*, 1995 [99] (section. 2.2.8). Here we have chosen the HFR time series on a

subset of the original HFR grid, as depicted in Figure. 3.30, due to its high resolution and continuity (hourly data). Also considering that this is the place where the MS gyre was identified with the radar velocity maps and with the geostrophic current analysis.

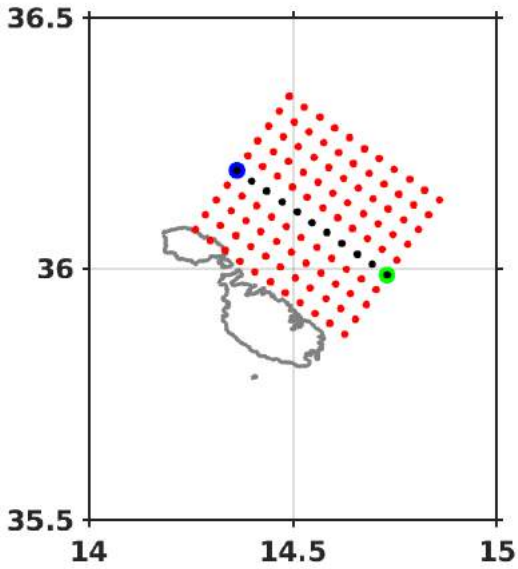

Figure 3.30: subgrid of the HFR original grid to calculate vorticity with *Sanderson*, 1995 [99] method. Red dots denote grid points where data was available for most of the time period studies. Blue, green and black dots represent grid points where velocity will be compared with vorticity.

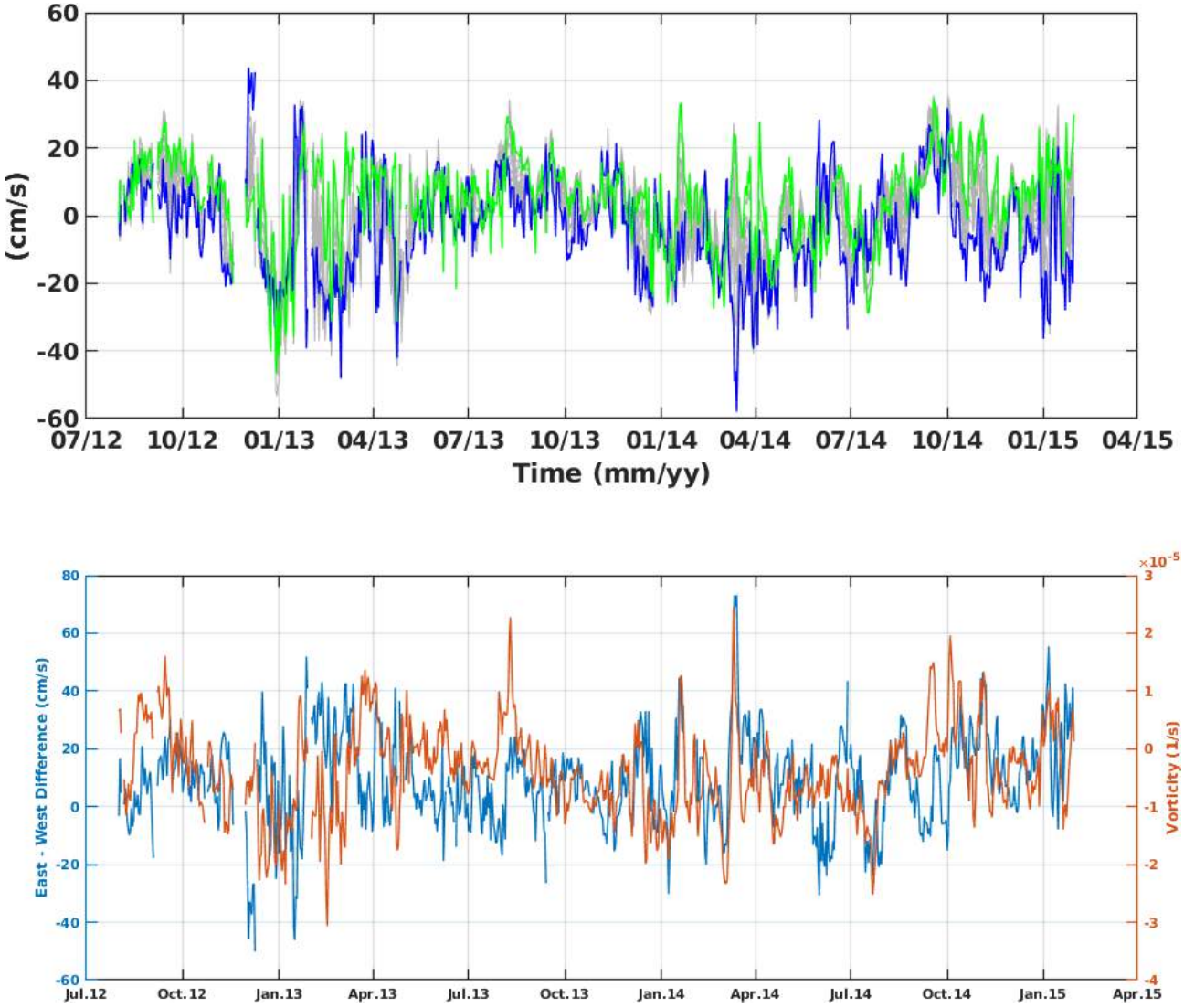

Figure 3.31: Upper panel represents the meridional velocity time series on Figure. 3.30. Blue time series corresponds to the blue dot in Figure. 3.30, as well as the green dot corresponds to the green time series. Intermediate black dots time series in Figure. 3.30 are represented in gray in the current figure. Lower panel depicts the East - West difference (left hand side) time series calculated from the difference between blue and green velocity time series from the HFR radar dataset and vorticity (right hand side) calculated using *Sanderson*, 1995[99] method through the lstranslate routine developed by the HFR radar group at the Naval Postgraduate School.

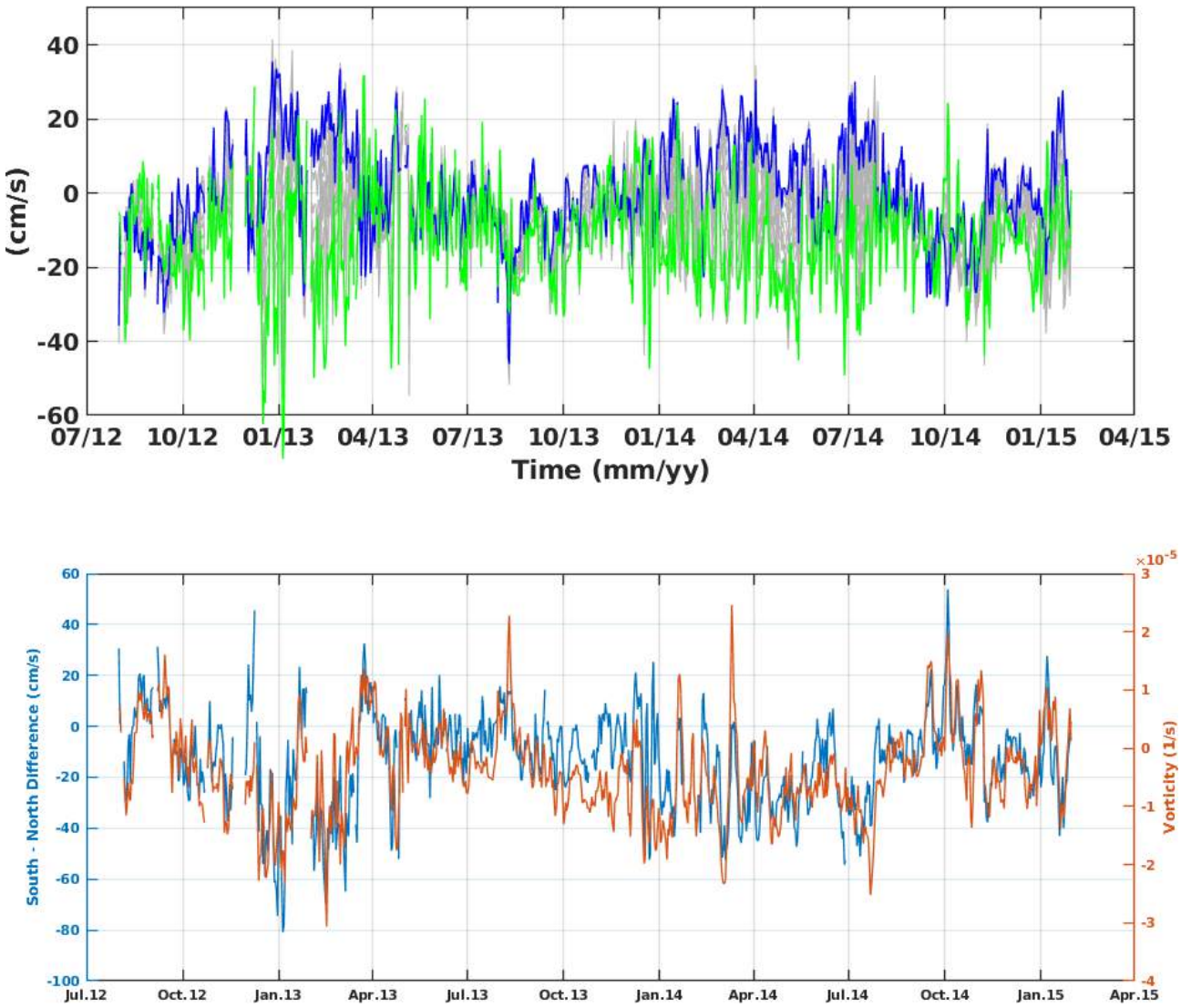

Figure 3.32: Upper panel represents the latitudinal velocity time series on Figure. 3.30. Blue time series corresponds to the blue dot in Figure. 3.30, as well as the green dot corresponds to the green time series. Intermediate black dots time series in Figure. 3.30 are represented in gray in the current figure. Lower panel depicts the South-North difference (left hand side) time series calculated from the difference between blue and green velocity time series from the HFR radar dataset and vorticity (right hand side) calculated using *Sanderson*, 1995[99] method through the lstranslate routine developed by the HFR radar group at the Naval Postgraduate School.

Figures. 3.31 and 3.32 represent the time series at the grid points in Figure. 3.30. They show the presence of the anticyclonic MS gyre over the winter in January-March 2013 and January-March 2014, with the later being persistent until fall 2014 (more evident with the South-North component). This can be corroborated in the lower panel in Figures. 3.31 and 3.32, where vorticity calculated with Sanderson method was employed. The gyre is strongly anticyclonic with vorticity around $c = -2 \times 10^{-5} s^{-1}$. Here it can be seen that vorticity and the South-North (East-West) differences are in agreement with the periods previously stated (winter times for the anticyclonic gyre,

Figure. 3.33), so a quantitative description of the gyre has been found. On the other hand we were also able to individuate another mesoscale happening on the AIS period (Figure. 3.33 bottom right panel) with this method. This case can be included on a future work, since it might be related with a recirculation due to the BiOS.

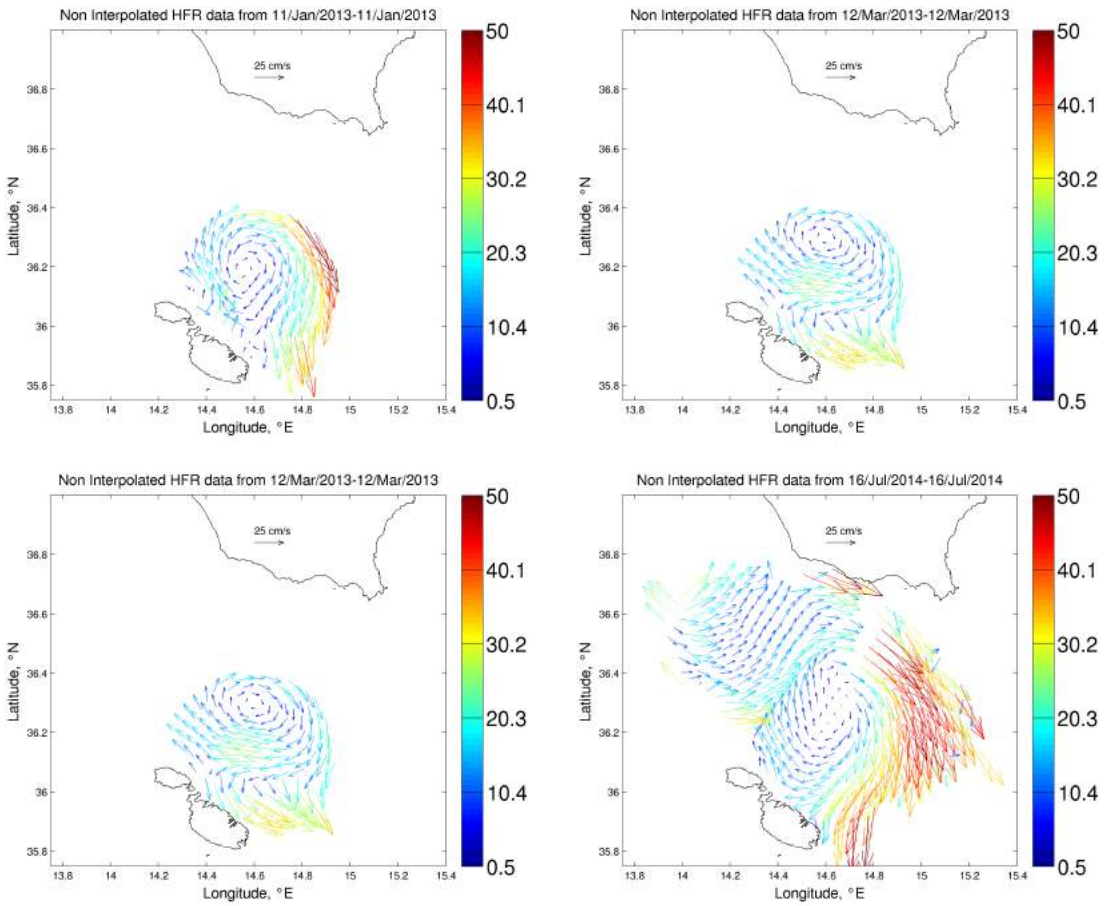

Figure 3.33: Anticyclonic gyres in agreement with vorticity calculated from Sanderson's method.

3.4 Ekman pumping in the Malta Sicily channel

Datasets of sea surface velocity from High Frequency radar and water column velocity from an ADCP (Acoustic Doppler Current Profiler) were collected at different stations (Table.3.4.1) on the 2nd and 3rd November 2013. We aim to analyze and estimate if it is suitable or not to apply classical Ekman theory in the area. where this theory is valid, and if it is accurate to make this approximation.

3.4.1 Ekman Layer

One of the difficulties making this approximation is to assume the wind stress (τ) and the eddy vertical viscosity ν_E, as constants, for example, different values of ν_E ranging the $1 \times 10^4\ m^2/s$ could give us different results. On the other hand a constant value of ν_E is not consistent with the reality due to turbulent components in the first meters of the water column, where the mixing layer is susceptible to changes in salinity, temperature and density.

Station	Position	Date
P 1.1	36.4345958 °N, 14.3263527 °E	02/10/2013 12 : 11 : 59
P 1.2	36.4317096 °N, 14.3433005 °E	02/10/2013 12 : 59 : 31
P 2.1	36.3542443 °N, 14.4256840 °E	02/10/2013 13 : 57 : 51
P 2.2	36.3518127 °N, 14.4309154 °E	02/10/2013 14 : 15 : 43
P 3	36.3021704 °N, 14.4600936 °E	02/10/2013 15 : 02 : 00
P 4	36.2239186 °N, 14.4871430 °E	02/10/2013 16 : 02 : 56
T 5	36.3801987 °N, 14.7237430 °E	03/10/2013 10 : 03 : 48
T 6	36.3227515 °N, 14.7186831 °E	03/10/2013 11 : 02 : 53
T 7	36.2970532 °N, 14.6923354 °E	03/10/2013 11 : 58 : 18
T 8	36.2721440 °N, 14.6256294 °E	03/10/2013 12 : 58 : 25
T 9	36.2468305 °N, 14.4874536 °E	03/10/2013 14 : 10 : 07
T 10	36.2187300 °N, 14.4533167 °E	03/10/2013 15 : 00 : 31

Classical Ekman theory assumes situations as depicted in Fig.3.34, where an ocean region with interior flow field $(\bar{u}, \bar{v})$ is subjected to wind stress (τ^x, τ^y) along its surface. Assuming steady conditions, an homogeneous fluid, and a geostrophic interior, we obtain the following equations for the flow field (u, v) in the surface Ekman layer,

$$-f(v - \bar{v}) = \nu_E \frac{\partial^2 u}{\partial z^2}, \tag{3.2a}$$

$$f(u - \bar{u}) = \nu_E \frac{\partial^2 v}{\partial z^2}. \tag{3.2b}$$

with the following boundary conditions,

$$\text{Surface } (z = 0): \quad \rho_0 \nu_E \frac{\partial u}{\partial z} = \tau^x, \quad \rho_0 \nu_E \frac{\partial v}{\partial z} = \tau^y, \tag{3.3a}$$

$$\text{Toward interior } (z \to \infty): \quad u = \bar{u}, \quad v = \bar{v}. \tag{3.3b}$$

ν_E is the vertical eddy viscosity and d the Ekman depth defined as,

$$d = \sqrt{\frac{2\nu_E}{f}} \tag{3.4}$$

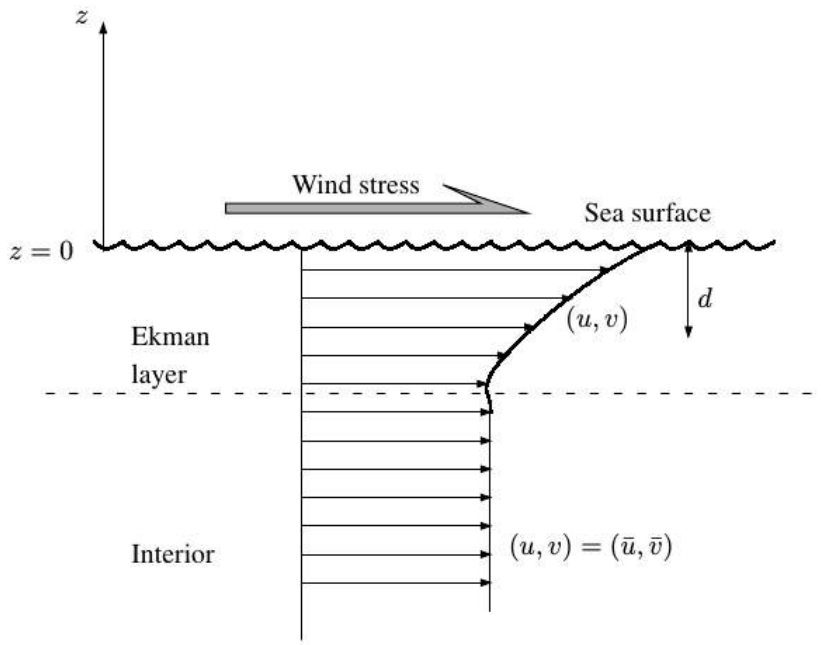

Figure 3.34: The surface Ekman layer generated by a wind stress on the ocean.

where the solution is,

$$u = \bar{u} + \frac{\sqrt{2}}{\rho_0 f d} e^{-z/d} \left[\tau^x \cos\left(\frac{z}{d} - \frac{\pi}{4}\right) - \tau^y \sin\left(\frac{z}{d} - \frac{\pi}{4}\right) \right], \tag{3.5a}$$

$$v = \bar{v} + \frac{\sqrt{2}}{\rho_0 f d} e^{-z/d} \left[\tau^x \sin\left(\frac{z}{d} - \frac{\pi}{4}\right) - \tau^y \cos\left(\frac{z}{d} - \frac{\pi}{4}\right) \right]. \tag{3.5b}$$

Now we rewrite this solution in terms of our experimental datasets. First of all our new boundary conditions are:

$$\begin{aligned} \text{Surface}(z = 0): &\quad u, v = u_{\text{Radar}}, v_{\text{Radar}} \quad \text{and} \quad \tau = \tau^{x,y} \\ \text{At the Ekman layer depth}(z = -d): &\quad \bar{u}, \bar{v} = u_{\text{ACDP}}, v_{\text{ADCP}} \quad \text{and} \quad \tau^{x,y} = 0, \end{aligned}$$

where the ADCP velocity values are taken from the deepest value measured by from the current-meter. Now integrating Eq.3.3a with respect to z, from the surface

to the Ekman depth,

$$\begin{aligned}
\int_{-d}^{0} \mathrm{d}u &= \int_{-d}^{0} \frac{\tau^x}{\rho_0 \nu_E} \mathrm{d}z \\
u(0) - u(-d) &= \frac{\tau^x}{\rho_0 \nu_E} \int_{-d}^{0} \mathrm{d}z \\
u_{\mathrm{Radar}} - u_{\mathrm{ADCP}} &= \frac{\tau^x}{\rho_0 \nu_E} (z(0) - z(-d)) \\
&= \frac{\tau^x}{\rho_0 \nu_E} d,
\end{aligned}$$

the same procedure is applied for the y direction where we obtain,

$$\tau^x = (u_{radar} - u_{ADCP}) \frac{\rho_0 \nu_E}{d} \tag{3.8a}$$

$$\tau^y = (v_{radar} - v_{ADCP}) \frac{\rho_0 \nu_E}{d} \tag{3.8b}$$

we assumed values of constant density $\rho_0 = 1027kg/m3$ (density of sea water), constant eddy vertical velocity $\nu_E = 1 \times 10^4\ m^2/s$, $f = 2\Omega \sin\phi$ where ϕ is latitude. We preceded to compute the Ekman layer in the stations mentioned in table 3.4.1, where we found that Ekman theory could be applicable: P1.1, P2.1, T5, T6, T7 and T9 as we can see in the following plots (Fig.3.35).

The plots show agreement with the theory in those points, but on the other hand the other stations did not show the same. This could probably be because of the influence of the rapid Atlantic Ionian Stream which was present in the area as we can see in Fig.3.36 but most important the constant values of the vertical eddy viscosity and the density which greatly affect the approximation.

Since momentum is carried by the wind and goes down into the interior due to turbulent motions (rather than by molecular processes). So it is of importance to have those terms into account. As in the classical Ekman theory, when we assume a height independent (barotrophic) wind, we are considering that there is no vertical shear of the wind, which is an extreme simplification from the turbulent point of view. So incorporating a vertically variable eddy viscosity and a baroclinic boundary layer into the Ekman solution could give us a better estimation assuming $\nu_E = \nu_E(z,t)$ and $\rho = \rho(T,S)$.

The vertical eddy viscosity, may be derived directly from measurements of the Reynolds stress using the definition equation, $\nu_E = -\langle uw \rangle \frac{\mathrm{d}U}{\mathrm{d}z}$, if the stress can be

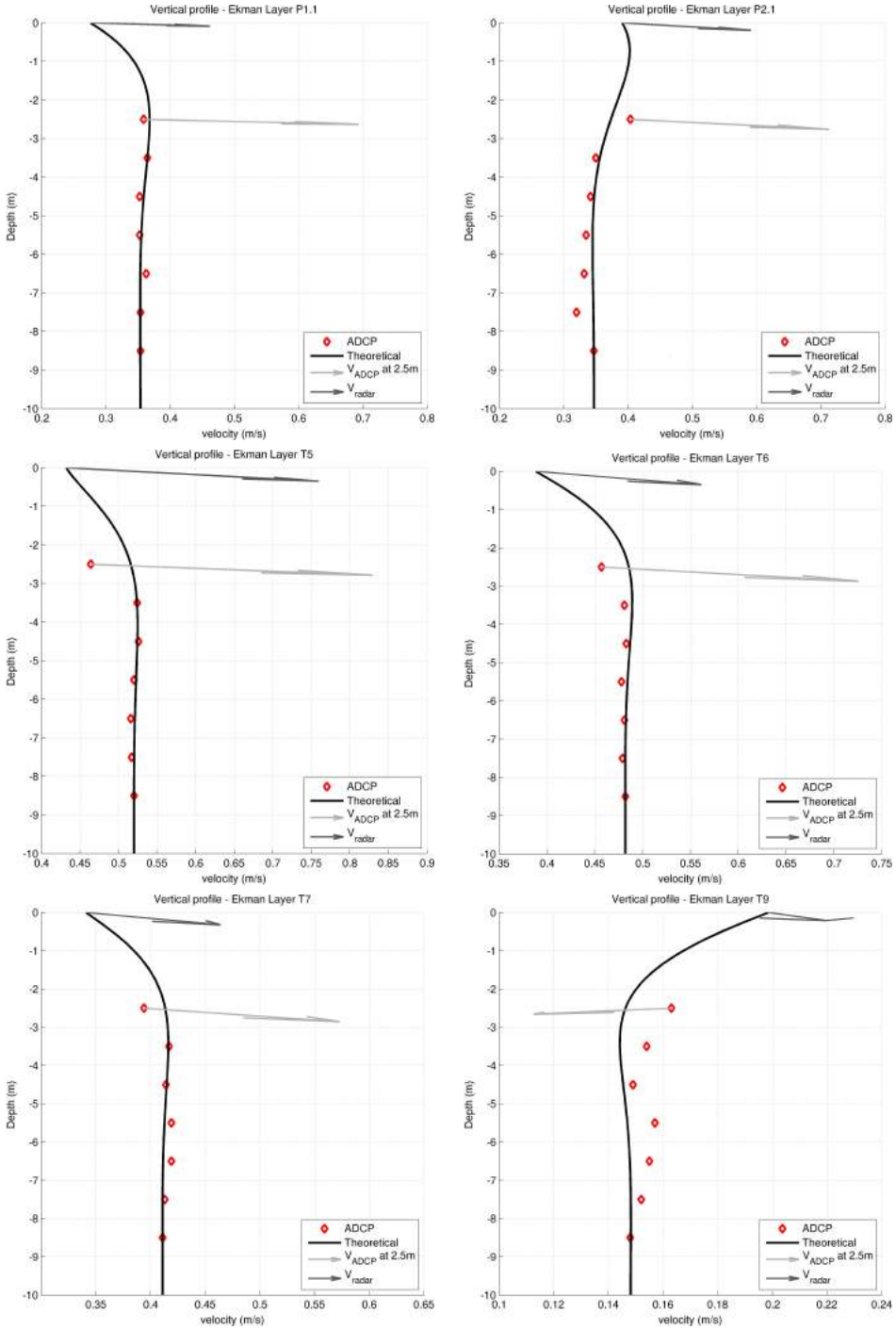

Figure 3.35: Theoretical Ekman layer compared with ADCP data at different stations in the Malta-Sicily channel.

measured by measuring u and w fluctuations of the mean flow and its variation with height, $\frac{\mathrm{d}U}{\mathrm{d}z}$ (*Thorpe*, 2005 [109]).

We need to point out that the values of the current meter are not so close enough to the surface to see the mixed layer which from Figure.3.35 is in the first 3 meters of the water column.

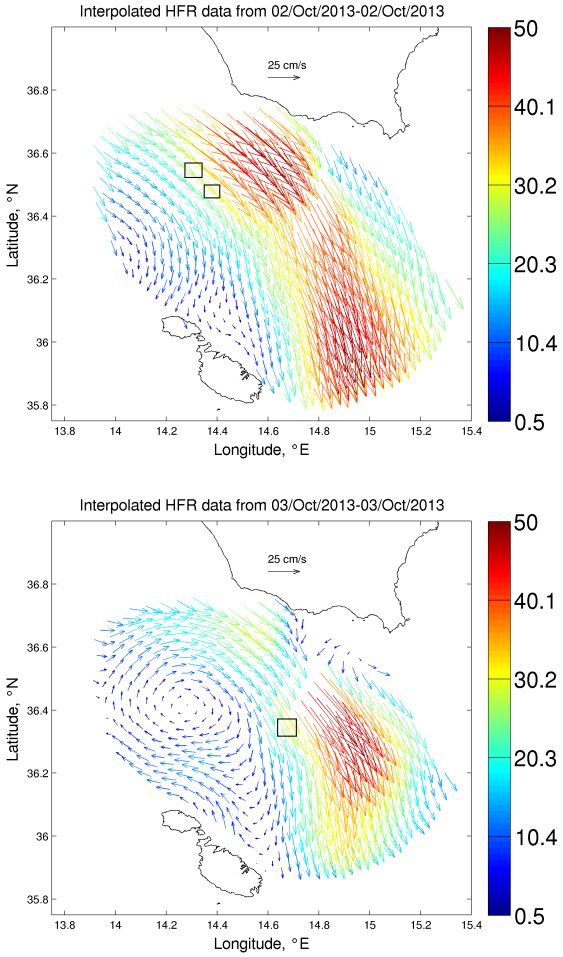

Figure 3.36: Surface velocity fields obtained from HFR (High frequency Radar) measurements on The 2nd and the 3rd October 2013. The black boxes show the average position of the stations.

4 Conclusions

For this thesis our main focus was to determine and describe the patterns and dynamical processes driving the surface circulation of the Malta-Sicily channel applying various techniques and data products. For this, estimates of high-frequency radar velocities, Maps of Absolute Dynamic Topography (MADT), sea surface temperature (SST), Chlorophyll concentration (CHL), drifters trajectories and wind velocity fields as described in Chapter. 2 were used.

Since the Malta-Sicily channel belongs to the Sicily channel system, we were able to study the whole system using using Maps of Absolute Dynamic Topography (MADT) and wind velocity fields. This with the aim of having a perception of the dynamical processes undergoing the circulation around the Malta Sicily channel. We computed geostrophic currents and compared them with previous studies carried out in the Sicily channel. We were able to identify some of the main structures governing the circulation as described by the studies of Lermusiaux, 1999 [57] and lately by Joiuni et al., 2016 [52]. Some of these structures were found to be present in the area, like the Algerian current, the Bifurcation Atlantic current, the Atlantic Tunisian current and the Atlantic Ionian Stream. These permanent structures, along with some mesoscales drive the circulation in the Sicilian channel. A new mesoscale, which was not present in the previous studies was found to be persistent in the Malta Sicily channel; the anticyclonic Malta Sicily gyre. This gyre has a radius of about 50 km and spins with a velocity of $\sim$ 10 cm/s. This discover motivated us to track and individuate the gyre.

Our studies show that at the surface, is the Atlantic water coming from the Gibraltar strait that after entering into the Sicily channel (through the strait of Sicily) is able to flow towards the Sicilian coast. Here due to bathymetry and a system of deep canyons, the currents is deviated towards the Malta sill, where bathymetry rise from 1000 m to about 200 m. There due to changes in potential vorticity the Atlantic Ionian stream is triggered, showing that bathymetry controls its pathway and being feed by the two branches of the Algerian current; the bifurcation Tunisian current and the Atlantic Tunisian current, behaving like a jet stream with an average velocity of 40 cm/s. Then this Jet stream deepens into the Ionian, where changes in bathymetry

at the Malta Escarpment (3000 m) make the current exit the channel and depending on the phase of the Adriatic-Ionian Bimodal Oscillating system (BiOS), it flows following the phase of the North Ionian Jet (NIG).

We were able to identify the influence of the BiOS in our are of study. When in the its cyclonic phase the BiOS (cyclonic NIG), blocks the water in the Malta Sicily channel, namely the Atlantic Ionian stream at the Malta Escarpment. Since the AIS is blocked towards the North Ionian, instead flows as the Mid Ionian Jet towards Creta. This process makes the Adriatic basin to be more saline and the surface water in Creta fresher due to the direct input of Atlantic water. On the other hand when the North Ionian Gyre is on its anticyclonic phase (anticyclonic BiOS) the AIS flows towards the North Ionian sea, bringing fresh water into the Adriatic basin and on the contrary of the cyclonic phase of the BiOS, making the surface water in Creta saltier supporting the studies being carried out by Gacic et al [33], [34], [21], [35], [8].

Our studies showed that geostrophic balance is a good approximation to describe the dynamics in the area at more than weekly time scales. The geostrophic currents in the area (AIS and Gyre) are responsible for advection of biogeochemical properties. This can give an input for the modeling of the productivity and the effects on biological cycles (carbon and nitrogen cycling among others) since phytoplankton is an important interface in the exchange of carbon dioxide and nitrogen fixation from atmosphere to ocean and vice versa. This fact is also important for upwelling since if phytoplankton is over produced and zooplankton is not able to eat it, then the phytoplankton sinks down to the bottom of the sea being absorbed by the soil and then rising back to the surface nutrients through upwelling events. As winds are SE, then there is a contributions on the reinforcement of the AIS, which even if neglected in the geostrophic approximation, helps to build up the sea level generating the pressure gradient needed to balance the Coriolis force.

On the other hand, wind velocity fields were almost constant for the period studied, where monthly, seasonal, and inter-annual variabilities were computed for both datasets. Wind stress curl over showed coastal Ekman upwelling and downwelling happening in the coast of Sicily. Here the wind even if neglected in the geostrophic approximation help to build up the pressure gradient needed to balance the Coriolis force in the area at scales longer than a week.

Due to the high resolution of high frequency radar estimates, we were able to study the Malta Sicily channel surface circulation. At first, we validated the data using different datasets which showed to be in agreement with the velocity fields estimated by the HF radar. The images from satellite Chlorophyll showed the influence of the Atlantic Ionian stream as well as the Malta Sicily gyre. Due to the action of

these structures, chlorophyll concentrations are confined along the Sicilian coast constraining mixing between the two zones as it was shown. phytoplankton is advected then by the AIS towards the Ionian. On the other hand when the anticyclonic MS gyre is present the chlorophyll concentrations are constrained and concentrated in the channel.

On the other hand, maps of sea surface temperature showed that the cold front from the Atlantic water mass enters into the channel mostly for the late-spring, summer and early-fall, showing typical values for this water mass. Drifters also showed the strength of the AIS and the MS gyre. These drifters were used as well to validate the HFR datasets. We deployed numerical drifters in order to calculate the separation distance between the real drifters and the numerical ones. Here We found that the radar derived currents are able to simulate the drifters trajectories up to 24 hours, having into account that the drifters were submerged at 10 m from the surface. We also were able to identify inertial currents either with the numerical particles as well as with the real drifters. So the High frequency radar technology is a good tool to estimate current patterns.

In order to individuate the anticyclonic Malta Sicily gyre, we used Sanderson's method [Sanderson et al., 1995 [99]] to find the kinematic properties of the eddy. Our studies revealed that the eddy prevails through out the winter period in agreement with the qualitative studies we carried out previously, identifying then the anticyclonic mesoscale also in the quantitatively sense.

The analysis of the time series using complex correlation was used to look at the high frequency components. Since the phase angle of the complex correlation coefficient is a good measure of the average relative angular displacement (veering) between a pair of two-dimensional vector series, we were able to identify Ekman transport in the area with our datasets. The correlation was made taking the advantage of the high resolution and the nature of HFR data, using the residual velocity (i.e, removing the geostrophic component of the HFR flow) with the wind. It showed a veering angle of ~ 40 degrees. Corroborating the influence of the wind field, which plays an important role at shorter time scales too.

On the other hand we used the classical Ekman theory in order to get an insight of the water column in the Malta Sicily channel using ADCP's and Hf radar data. We considered no vertical shear of the wind, which is an extreme simplification from the turbulent point of view. We ere able to identify Ekman layers for some of the ADCP stations but in general the approach was not successful. We suggest incorporating a vertical variable eddy viscosity and a baroclinic boundary layer into the Ekman solution, which could give us a better estimation assuming $\nu_E = \nu_E(z,t)$ and $\rho = \rho(T,S)$. We need to point out that the values of the current-meter are not so close

enough to the surface to see the mixed layer is in the first 3 meters of the water column.

Bibliography

[1] N. Aeronautics and N. Space Administration, *AQUA*, 2002.

[2] M. Astraldi, S. Balopoulos, J. Candela, J. Font, M. Gacic, G. Gasparini, B. Manca, A. Theocharis, and J. Tintoré, *The role of straits and channels in understanding the characteristics of mediterranean circulation*, Progress in Oceanography, 44 (1999), pp. 65–108.

[3] M. Astraldi, F. Conversano, G. Civitarese, G. Gasparini, M. R. d'Alcalà, and A. Vetrano, *Water mass properties and chemical signatures in the central mediterranean region*, Journal of Marine Systems, 33 (2002), pp. 155–177.

[4] M. Astraldi, G. Gasparini, S. Sparnocchia, M. Moretti, and E. Sansone, *The characteristics of the water masses and the water transport in the sicily strait at long time scales*, BULLETIN-INSTITUT OCEANOGRAPHIQUE MONACO-NUMERO SPECIAL-, (1996), pp. 95–116.

[5] R. Atlas, R. N. Hoffman, J. Ardizzone, S. M. Leidner, J. C. Jusem, D. K. Smith, and D. Gombos, *A cross-calibrated, multiplatform ocean surface wind velocity product for meteorological and oceanographic applications*, Bulletin of the American Meteorological Society, 92 (2011), pp. 157–174.

[6] K. Béranger, L. Mortier, and M. Crépon, *Seasonal variability of water transport through the straits of gibraltar, sicily and corsica, derived from a high-resolution model of the mediterranean circulation*, Progress in Oceanography, 66 (2005), pp. 341–364.

[7] K. Béranger, L. Mortier, G.-P. Gasparini, L. Gervasio, M. Astraldi, and M. Crépon, *The dynamics of the sicily strait: a comprehensive study from observations and models*, Deep Sea Research Part II: Topical Studies in Oceanography, 51 (2004), pp. 411–440.

[8] L. Bessières, M. Rio, C. Dufau, C. Boone, and M. Pujol, *Ocean state indicators from myocean altimeter products*, Ocean Science, 9 (2013), p. 545.

[9] J. Bethoux, *Budgets of the mediterranean sea-their dependance on the local climate and on the characteristics of the atlantic waters*, Oceanologica acta, 2 (1979), pp. 157–163.

[10] J. Bethoux and B. Gentili, *Functioning of the mediterranean sea: past and present changes related to freshwater input and climate changes*, Journal of Marine Systems, 20 (1999), pp. 33–47.

[11] J. Bethoux, B. Gentili, P. Morin, E. Nicolas, C. Pierre, and D. Ruiz-Pino, *The mediterranean sea: a miniature ocean for climatic and environmental studies and a key for the climatic functioning of the north atlantic*, Progress in Oceanography, 44 (1999), pp. 131–146.

[12] J. Bethoux and D. Tailliez, *Deep-water in the western mediterranean sea, yearly climatic signature and enigmatic spreading*, in Ocean processes in climate dynamics: global and mediterranean examples, Springer, 1994, pp. 355–369.

[13] N. Bialystocki and D. Konovessis, *On the estimation of ship's fuel consumption and speed curve: A statistical approach*, Journal of Ocean Engineering and Science, 1 (2016), pp. 157–166.

[14] H. Björnsson and S. Venegas, *A manual for eof and svd analyses of climatic data*, CCGCR Report, 97 (1997), pp. 112–134.

[15] G. E. Borzelli, M. Gacic, P. Lionello, and P. Malanotte-Rizzoli, *The Mediterranean Sea: Temporal variability and spatial patterns*, John Wiley & Sons, 2014.

[16] CALYPSO, *Real-time viewing of sea surface currents in the malta channel.*

[17] J. Candela, *The gibraltar strait and its role in the dynamics of the mediterranean sea*, Dynamics of Atmospheres and Oceans, 15 (1991), pp. 267–299.

[18] D. B. Chelton, M. G. Schlax, and R. M. Samelson, *Global observations of nonlinear mesoscale eddies*, Progress in Oceanography, 91 (2011), pp. 167–216.

[19] W.-S. Chiang, W.-C. Yang, J.-W. Lai, K.-I. Lin, et al., *An application of hfr data on estimation of drifter velocities off eastern taiwan*, in The Twenty-third International Offshore and Polar Engineering Conference, International Society of Offshore and Polar Engineers, 2013.

[20] A. C. Ciappa, *Surface circulation patterns in the sicily channel and ionian sea as revealed by modis chlorophyll images from 2003 to 2007*, Continental Shelf Research, 29 (2009), pp. 2099–2109.

[21] G. Civitarese, M. Gačić, M. Lipizer, and G. Eusebi Borzelli, *On the impact of the bimodal oscillating system (bios) on the biogeochemistry and biology of the adriatic and ionian seas (eastern mediterranean)*, Biogeosciences, 7 (2010), pp. 3987–3997.

[22] M. e. m. s. COPERNICUS, *MEDITERRANEAN SEA GRIDDED L4 SEA SURFACE HEIGHTS AND DERIVED VARIABLES REPROCESSED (1993-ONGOING): Quality Information Document (CMEMS-SL-QUID-008-032-051)*.

[23] S. Cosoli, A. Drago, G. Ciraolo, and F. Capodici, *Tidal currents in the malta–sicily channel from high-frequency radar observations*, Continental Shelf Research, 109 (2015), pp. 10–23.

[24] J. Craddock, *Problems and prospects for eigenvector analysis in meteorology*, Journal of the Royal Statistical Society. Series D (The Statistician), 22 (1973), pp. 133–145.

[25] K. Dohan, *Ocean surface currents from satellite data*, Journal of Geophysical Research: Oceans, (2017).

[26] A. Drago, *Addressing the need of marine observations for fisheries*, Proceedings of the Fourth APS Annual Seminar on the Development of Agriculture and Fisheries in Malta, (2003), pp. 33–73.

[27] A. Drago, R. Sorgente, and A. Olita, *Sea temperature, salinity and total velocity climatological fields for the south-central mediterranean sea*, MedSudMed Technical Documents, (2010), p. 35.

[28] A. Drago, R. Sorgente, and A. Ribotti, *A high resolution hydrodynamic 3d model simulation of the malta shelf area*, in Annales geophysicae, vol. 21, 2003, pp. 323–344.

[29] B. M. Emery, L. Washburn, and J. A. Harlan, *Evaluating radial current measurements from codar high-frequency radars with moored current meters*, Journal of Atmospheric and Oceanic Technology, 21 (2004), pp. 1259–1271.

[30] M. Fieux, *Observations hydrologiques hivernales dans le "rech" lacaze-duthiers (golfe du lion).*, Cahiers Ocanographiques, 23 (1971), pp. 677–686.

[31] R. Frassetto, *A study of the turbulent flow and character of the water masses over the sicilian ridge in both summer and winter*, Rapp. PV CIESM, 18 (1965), pp. 812–815.

[32] A. Fukuoka, *The central meteorological observatory, a study on 10-day forecast (a synthetic report)*, Geophysical Magazine, 22 (1951), pp. 177–208.

[33] M. Gačić, G. Borzelli, G. Civitarese, V. Cardin, and S. Yari, *Can internal processes sustain reversals of the ocean upper circulation? the ionian sea example*, Geophysical Research Letters, 37 (2010).

[34] M. Gačić, G. Civitarese, G. Eusebi Borzelli, V. Kovačević, P.-M. Poulain, A. Theocharis, M. Menna, A. Catucci, and N. Zarokanellos, *On the relationship between the decadal oscillations of the northern ionian sea and the salinity distributions in the eastern mediterranean*, Journal of Geophysical Research: Oceans, 116 (2011).

[35] M. Gačić, K. Schroeder, G. Civitarese, S. Cosoli, A. Vetrano, and G. Eusebi Borzelli, *Salinity in the sicily channel corroborates the role of the adriatic–ionian bimodal oscillating system (bios) in shaping the decadal variability of the mediterranean overturning circulation*, Ocean Science, 9 (2013), pp. 83–90.

[36] S. Garzoli and C. Maillard, *Hydrologie et circulation hivernales dans les canaux de sicile et de sardaigne*, Int. rep. of the Laboratoire dÕOcéanographie Physique du Museum, Paris, (1976).

[37] G. Gelsi and F. Mosetti, *An attempt to calculate the water flow through the strait of sicily*, Boll. Oceanol. Teorica ed Appl, 2 (1984), pp. 53–69.

[38] H. C. Graber, B. K. Haus, R. D. Chapman, and L. K. Shay, *Hf radar comparisons with moored estimates of current speed and direction: Expected differences and implications*, Journal of Geophysical Research: Oceans, 102 (1997), pp. 18749–18766.

[39] G. Grancini, A. Lavenia, and F. Mosetti, *A contribution to the hydrology of the strait of sicily*, in Oceanography of the Strait of Sicily, Saclantcen Conference Proceedings, vol. 7, 1972, pp. 68–81.

[40] G. Grancini and A. Michelato, *Current structure and variability in the strait of sicily and adjacent area*, Annales Geophysicae, 5 (1987), pp. 75–88.

[41] T. P. group, *General circulation of the eastern mediterranean*, Earth Science Reviews, 32 (1992), pp. 285–309.

[42] J. Harlan, E. Terrill, L. Hazard, C. Keen, D. Barrick, C. Whelan, S. Howden, and J. Kohut, *The integrated ocean observing system high-frequency radar network: status and local, regional, and national applications*, Marine Technology Society Journal, 44 (2010), pp. 122–132.

[43] C. Herbaut, F. Codron, and M. Crépon, *Separation of a coastal current at a strait level: case of the strait of sicily*, Journal of physical oceanography, 28 (1998), pp. 1346–1362.

[44] T. Hopkins, *Physics of the sea*, in Western Mediterranean, 1985.

[45] R. X. Huang, *OCEAN CIRCULATION, Wind-Driven and Thermohaline Processes*, Cambridge University Press, 20.

[46] S. B. Ismail, C. Sammari, G. P. Gasparini, K. Beranger, M. Brahim, and L. Aleya, *Water masses exchanged through the channel of sicily: evidence for the presence of new water masses on the tunisian side of the channel*, Deep Sea Research Part I: Oceanographic Research Papers, 63 (2012), pp. 65–81.

[47] S. B. Ismail, K. Schroeder, C. Sammari, G. P. Gasparini, M. Borghini, and L. Aleya, *Interannual variability of water mass properties in the tunisia–sicily channel*, Journal of Marine Systems, 135 (2014), pp. 14–28.

[48] D. Iudicone, R. Santoleri, S. Marullo, and P. Gerosa, *Sea level variability and surface eddy statistics in the mediterranean sea from topex/poseidon data*, Journal of Geophysical Research: Oceans, 103 (1998), pp. 2995–3011.

[49] F. Jebri, F. Birol, B. Zakardjian, J. Bouffard, and C. Sammari, *Exploiting coastal altimetry to improve the surface circulation scheme over the central mediterranean sea*, Journal of Geophysical Research: Oceans, 121 (2016), pp. 4888–4909.

[50] F. Jebri, B. Zakardjian, F. Birol, J. Bouffard, L. Jullion, and C. Sammari, *Interannual variations of surface currents and transports in the sicily channel derived from coastal altimetry*, Journal of Geophysical Research: Oceans, (2017).

[51] O. M. Johannessen, D. Good, and C. Smallenburger, *Observation of an oceanic front in the ionian sea during early winter 1970*, Journal of Geophysical Research, 82 (1977), pp. 1381–1391.

[52] M. Jouini, K. Béranger, T. Arsouze, J. Beuvier, S. Thiria, M. Crépon, and I. Taupier-Letage, *The sicily channel surface circulation revisited using a neural clustering analysis of a high-resolution simulation*, Journal of Geophysical Research: Oceans, 121 (2016), pp. 4545–4567.

[53] P. K. Kundu, *Ekman veering observed near the ocean bottom*, Journal of Physical Oceanography, 6 (1976), pp. 238–242.

[54] H. Lacombe, P. Tchernia, and L. Gamberoni, *Variable bottom water in the western mediterranean basin*, Progress in Oceanography, 14 (1985), pp. 319–338.

[55] G. Larnicol, N. Ayoub, and P.-Y. Le Traon, *Major changes in mediterranean sea level variability from 7 years of topex/poseidon and ers-1/2 data*, Journal of Marine Systems, 33 (2002), pp. 63–89.

[56] J. Le Vourch, C. Millot, N. Castagne, P. Le Borgne, and J. Olry, *Atlas of thermal fronts of the mediterranean sea derived from satellite imagery*, Memoires de lInstitut oceanographique, Monaco, 16 (1992), p. 146p.

[57] P. Lermusiaux, *Estimation and study of mesoscale variability in the strait of sicily*, Dynamics of Atmospheres and Oceans, 29 (1999), pp. 255–303.

[58] P. Lermusiaux and A. Robinson, *Features of dominant mesoscale variability, circulation patterns and dynamics in the strait of sicily*, Deep Sea Research Part I: Oceanographic Research Papers, 48 (2001), pp. 1953–1997.

[59] E. Lodolo and Z. Ben-Avraham, *A submerged monolith in the sicilian channel (central mediterranean sea): Evidence for mesolithic human activity*, Journal of Archaeological Science: Reports, 3 (2015), pp. 398–407.

[60] E. N. Lorenz, *Empirical orthogonal functions and statistical weather prediction*, (1956).

[61] P. Malanotte-Rizzoli and A. R. Robinson, *Ocean processes in climate dynamics: global and Mediterranean examples*, vol. 419, Springer Science & Business Media, 2012.

[62] G. M. Manzella, T. Hopkins, P. Minnett, and E. Nacini, *Atlantic water in the strait of sicily*, Journal of Geophysical Research: Oceans, 95 (1990), pp. 1569–1575.

[63] G. M. R. Manzella, G. P. Gasparini, and M. Astraldi, *Water exchange between the eastern and western mediterranean through the strait of sicily*, Deep Sea Research A, 35 (1988), pp. 1021–1035.

[64] C. Millot and I. Taupier-Letage, *Circulation in the mediterranean sea*, in The Mediterranean Sea, Springer, 2005, pp. 29–66.

[65] C. Morelli, C. Gantar, and M. Pisani, *Bathymetry, gravity and magnetism in the strait of sicily and in the ionian sea*, Boll. Geofis. teor. appl, 17 (1975), pp. 39–58.

[66] M. Moretti, E. Sansone, G. Spezie, and A. De Maio, *Results of investigations in the sicily channel (1986–1990)*, Deep Sea Research Part II: Topical Studies in Oceanography, 40 (1993), pp. 1181–1192.

[67] E. Napolitano, G. Sannino, V. Artale, and S. Marullo, *Modeling the baroclinic circulation in the area of the sicily channel: The role of stratification and energy diagnostics*, Journal of Geophysical Research: Oceans, 108 (2003).

[68] National Oceanic and Atmospheric Administration NOAA, *Advanced very high resolution radiometer - avhrr*. http://noaasis.noaa.gov/NOAASIS/ml/avhrr.html.

[69] ——, *NOAA-N Prime*.

[70] G. R. North, *Empirical orthogonal functions and normal modes*, Journal of the Atmospheric Sciences, 41 (1984), pp. 879–887.

[71] A. Obukhov, *Statistically homogeneous fields on a sphere*, Usp. Mat. Nauk, 2 (1947), pp. 196–198.

[72] ——, *The statistically orthogonal expansion of empirical functions*, Bulletin of the Academy of Sciences of the USSR. Geophysics Series (English Transl.), 1 (1960), pp. 288–291.

[73] N. Oceanic and A. Administration-NOAA, *NOAA-N prime (NOAA-19) satellite*. http://www.osd.noaa.gov/Spacecraft$%$20Systems/Pollar_Orbiting_Sat/NOAA_N_Prime/noaanprime.html.

[74] U. of Malta, C. project, and A. Drago, *Kaptan*. https://www.um.edu.mt/__data/assets/pdf_file/0005/282119/Kaptanpdf.pdf.

[75] U. of Malta, N. O. C. (UK), N. I. of Water, A. R. N. Zealand), U. C. D. (Ireland), and I. N. di Oceanografia e Geofisica (Italy), *Cumecs-2*. http://cumecs2.blogspot.it/p/home_3.html.

[76] A. Olita, A. Ribotti, R. Sorgente, L. Fazioli, and A. Perilli, *Sla–chlorophyll-a variability and covariability in the algero-provençal basin (1997–2007) through combined use of eof and wavelet analysis of satellite data*, Ocean Dynamics, 61 (2011), pp. 89–102.

[77] R. ONKEN, A. R. ROBINSON, P. F. LERMUSIAUX, P. J. HALEY, and L. A. ANDERSON, *Data-driven simulations of synoptic circulation and transports in the tunisia-sardinia-sicily region: Physical and biochemical evolution of the eastern mediterranean in the'90s (pbe)*, Journal of geophysical research, 108 (2003), pp. PBE24–1.

[78] R. Onken and J. Sellschopp, *Seasonal variability of flow instabilities in the strait of sicily*, Journal of Geophysical Research: Oceans, 103 (1998), pp. 24799–24820.

[79] E. Ozturgut, *Temporal and spatial variability of water masses: The strait of sicily (medmiloc 72).*, tech. rep., DTIC Document, 1975.

[80] J. D. Paduan and H. C. Graber, *Introduction to high-frequency radar: reality and myth*, Oceanography, 10 (1997), pp. 36–39.

[81] J. D. Paduan and L. K. Rosenfeld, *Remotely sensed surface currents in monterey bay from shore-based hf radar (coastal ocean dynamics application radar)*, Journal of Geophysical Research: Oceans, 101 (1996), pp. 20669–20686.

[82] J. D. Paduan and L. Washburn, *High-frequency radar observations of ocean surface currents*, Annual review of marine science, 5 (2013), pp. 115–136.

[83] M. Philippe and L. Harang, *Surface temperature fronts in the mediterranean sea from infrared satellite imagery*, Elsevier Oceanography Series, 34 (1982), pp. 91–128.

[84] A. Piccioni, M. Gabriele, E. Salusti, and E. Zambianchi, *Wind-induced upwellings off the southern coast of sicily*, Oceanologica Acta, 11 (1988), pp. 309–314.

[85] M. H. Pickett and J. D. Paduan, *Ekman transport and pumping in the california current based on the us navy's high-resolution atmospheric model (coamps)*, Journal of Geophysical Research: Oceans, 108 (2003).

[86] S. Pierini and A. Rubino, *Modeling the oceanic circulation in the area of the strait of sicily: the remotely forced dynamics*, Journal of physical oceanography, 31 (2001), pp. 1397–1412.

[87] N. Pinardi, M. Zavatarelli, M. Adani, G. Coppini, C. Fratianni, P. Oddo, S. Simoncelli, M. Tonani, V. Lyubartsev, S. Dobricic, et al., *Mediterranean sea large-scale low-frequency ocean variability and water mass formation rates from 1987 to 2007: a retrospective analysis*, Progress in Oceanography, 132 (2015), pp. 318–332.

[88] I. Puillat, I. Taupier-Letage, and C. Millot, *Algerian eddies lifetime can near 3 years*, Journal of Marine Systems, 31 (2002), pp. 245–259.

[89] M.-I. Pujol, Y. Faugère, G. Taburet, S. Dupuy, C. Pelloquin, M. Ablain, and N. Picot, *Duacs dt2014: the new multi-mission altimeter data set reprocessed over 20 years.*, Ocean Science, 12 (2016).

[90] M.-I. Pujol and G. Larnicol, *Mediterranean sea eddy kinetic energy variability from 11 years of altimetric data*, Journal of Marine Systems, 58 (2005), pp. 121–142.

[91] H. Qian, Y. Li, R. He, and D. Eggleston, *Connectivity in the intra-american seas and implications for potential larval transport*, Coral Reefs, 34 (2015), pp. 403–417.

[92] M. P. M. Reedy, *Descriptive Physical Oceanography*, A. A. BALKEMA Publishers, 2001.

[93] A. R. Robinson, W. G. Leslie, A. Theocharis, and A. Lascaratos, *Mediterranean sea circulation*, Ocean currents: a derivative of the Encyclopedia of Ocean Sciences, (2001), pp. 1689–1705.

[94] A. R. Robinson, P. Malanotte-Rizzoli, A. Hecht, A. Michelato, W. Roether, A. Theocharis, Ü. Ünlüata, N. Pinardi, A. Artegiani, A. Bergamasco, et al., *General circulation of the eastern mediterranean*, Earth-Science Reviews, 32 (1992), pp. 285–309.

[95] A. R. Robinson, J. Sellschopp, A. Warn-Varnas, W. G. Leslie, C. J. Lozano, P. J. Halley, L. A. Anderson, and P. F. J. Lermusiaux, *The atlantic ionian stream*, Journal of Marine Systems, 20 (1999), pp. 129–156.

[96] M. Rovere and M. Wurtz, *Atlas of the mediterranean seamounts and seamount-like structures*, Gland, Switzerland and Málaga, Spain: IUCN, (2015).

[97] H. T. S., *Physical processes in the mediterranean basins.*, in Estuarine transport processes, 1978.

[98] C. Sammari, C. Millot, I. Taupier-Letage, A. Stefani, and M. Brahim, *Hydrological characteristics in the tunisia–sardinia–sicily area during spring 1995*, Deep Sea Research Part I: Oceanographic Research Papers, 46 (1999), pp. 1671–1703.

[99] B. G. Sanderson, *Structure of an eddy measured with drifters*, Journal of Geophysical Research: Oceans, 100 (1995), pp. 6761–6776.

[100] K. Schroeder, A. Ribotti, M. Borghini, R. Sorgente, A. Perilli, and G. Gasparini, *An extensive western mediterranean deep water renewal between 2004 and 2006*, Geophysical Research Letters, 35 (2008).

[101] S. C. Shadden, F. Lekien, J. D. Paduan, F. P. Chavez, and J. E. Marsden, *The correlation between surface drifters and coherent structures based on high-frequency radar data in monterey bay*, Deep Sea Research Part II: Topical Studies in Oceanography, 56 (2009), pp. 161–172.

[102] L. Solabarrieta, M. Cook, J. Paduan, A. Rubio, A. Fontán, S. Castanedo, M. Gonzalez, R. Medina, V. Fernández, and G. Charria, *Comparison between real drifter's trajectories and simulated trajectories using hf radar data, in the bay of biscay*, in EGU General Assembly Conference Abstracts, vol. 15, 2013.

[103] L. Solabarrieta, S. Frolov, M. Cook, J. Paduan, A. Rubio, M. González, J. Mader, and G. Charria, *Skill assessment of hf radar–derived products for lagrangian simulations in the bay of biscay*, Journal of Atmospheric and Oceanic Technology, 33 (2016), pp. 2585–2597.

[104] R. Sorgente, A. Drago, and A. Ribotti, *Seasonal variability in the central mediterranean sea circulation*, in Annales Geophysicae, vol. 21, 2003, pp. 299–322.

[105] R. Sorgente, A. Olita, P. Oddo, L. Fazioli, and A. Ribotti, *Numerical simulation and decomposition of kinetic energy in the central mediterranean: insight on mesoscale circulation and energy conversion*, Ocean Science, 7 (2011), p. 503.

[106] R. H. Stewart, *Introduction To Physical Oceanography*, Department of Oceanography, Texas A & M University, 2015.

[107] L. Talley, *Descriptive Physical Oceanography: An Introduction*, Elsevier Science, 2011.

[108] R. E. Thomson and W. J. Emery, *Data analysis methods in physical oceanography*, Newnes, 2014.

[109] S. Thorpe, *The Turbulent Ocean*, Cambridge University Press, 2005.

[110] J. A. Trinanes, M. J. Olascoaga, G. J. Goni, N. A. Maximenko, D. A. Griffin, and J. Hafner, *Analysis of flight mh370 potential debris trajectories using ocean observations and numerical model results*, Journal of Operational Oceanography, 9 (2016), pp. 126–138.

[111] I. Vigo, D. Garcia, and B. Chao, *Change of sea level trend in the mediterranean and black seas*, Journal of Marine Research, 63 (2005), pp. 1085–1100.

[112] P. Welch, *The use of fast fourier transform for the estimation of power spectra: a method based on time averaging over short, modified periodograms*, IEEE Transactions on audio and electroacoustics, 15 (1967), pp. 70–73.